5-26-2016

Design of Energy Efficient Embedded Systems Exploiting Domain-specific Information

Junlin Chen
University of Connecticut, junlin.chen@uconn.edu

Design of Energy Efficient Embedded Systems Exploiting Domain-specific Information

Junlin Chen, Ph.D.

University of Connecticut, 2016

Improving the energy efficiency has been the critical design goal for embedded systems. Recently, there have been some practical techniques employed to the power supply of embedded systems to extend the system's lifetime. One is renewable energy technologies such as energy harvesting from the environment to offer a sustainable, inexpensive, and maintenance-free alternative power source. Another is voltage overscaling (VOS) technique, which scales down the supply voltage to reduce the power consumption quadratically. However, most renewable energy sources are unstable and intermittent due to dynamically changing environmental conditions, and VOS inevitably incurs hardware errors, thereby posing new challenges to the improvements of energy efficiency in the embedded systems.

In this dissertation, we identify four specific power-hungry signal processing units and develop a suite of techniques to improve the energy efficiency of embedded systems, by jointly exploiting the properties of the power source and

the domain-specific information in the signal processing of embedded systems. First, we propose to dynamically adjust the modulation scheme to deal with time-varying wireless channel conditions and non-deterministic renewable energy levels in a coherent manner to maximize the data rate of RF circuits of the embedded systems. Then, we develop a progressive performance tuning approach to dynamically determine an acceptable signal processing performance in accordance with the changing energy level at runtime, by considering both of the non-deterministic characteristics of renewable energy and the unique relationship between signal processing performance and the required energy consumption. We also develop a link and energy adaptive UWB-based sensing technique to improve the detection time coverage and range coverage for self-sustained embedded applications. The proposed technique jointly exploits the link information between the transmitter and receiver of the UWB pulse radar, and the non-deterministic characteristics of the renewable energy, and dynamically adjusts the pulse repetition frequency of the UWB radar to enhance the sustainable operation under the unreliable energy supply. Finally, we present a low-power LDPC decoder design by exploiting inherent memory error statistics due to voltage scaling. After analyzing the error sensitivity to the decoding performance at different memory bits and memory locations in the LDPC decoder, we apply the scaled supply voltage to memory bits with high algorithmic error-tolerance capability to reduce the memory power consumption with minimal decoding performance loss.

Design of Energy Efficient Embedded Systems

Exploiting Domain-specific Information

Junlin Chen

B.S., University of Electronic Science and Technology of China, 2008

M.S., University of Electronic Science and Technology of China, 2011

A Dissertation

Submitted in Partial Fulfillment of the

Requirements for the Degree of

Doctor of Philosophy

at the

University of Connecticut

2016

APPROVAL PAGE

Doctor of Philosophy Dissertation

Design of Energy Efficient Embedded Systems Exploiting Domain-specific Information

Presented by

Junlin Chen, B.S., M.S.

Major Advisor

Lei Wang

Associate Advisor

John Chandy

Associate Advisor

Liang Zhang

University of Connecticut

2016

To my family.

ACKNOWLEDGEMENTS

First and foremost, I would like to thank my advisor, Prof. Lei Wang, for his constant support, excellent guidance and encouragement throughout my Ph.D. study at the University of Connecticut. He taught me how to research and opened my mind with his passion for new technology and sense of novelty. His broad knowledge, sharp insight and extraordinary vision have always been guiding me towards the right direction. Without Prof. Wang, all the accomplishments I made would be impossible.

Next, I would like to thank the members on my dissertation committee: Prof. John Chandy, Prof. Liang Zhang, Prof. Faquir Jain, and Prof. Shalabh Gupta, for their valuable feedback and comments to my research work.

I also want to thank my lab mates and friends: Guoxian Huang, Wenjie Huang, Menglong Guan, Shuai Chen, Dong Zhao, Ridvan Umaz, Fengyu Qian, Yanping Gong, Yi Huang, Lei Wan, and Hao Zhou. I sincerely appreciate the enjoyable time with them.

Last but not least, I want to express my deep gratitude to my parents and sister for their unconditional love and constant support throughout my life.

TABLE OF CONTENTS

LIST OF FIGURES

LIST OF TABLES

Chapter 1

Introduction

1.1 Overview

Improving energy efficiency has become one of the most critical design goals for the electrical embedded systems, especially when the power supply is limited. A lot of research work have been conducted to reduce the energy consumption by optimizing the signal processing and/or circuits operations without the consideration of the power source. Mostly, this type of method can lead to energy-efficient design because the power supply, such as rechargeable battery, is stable and continuous all the time, and the voltage generated from the battery can always enable the embedded systems to function correctly.

Recently, some emerging autonomous and distributed embedded systems, such as wireless sensor networks (WSN), self-organizing micro-robots, and medical implantable devices, have gained significant research interest. While many of these systems can be powered by batteries, frequent recharge and maintenance is costly if not impossible. Fortunately, renewable energy technologies such as

energy harvesting from the environment offer a sustainable, inexpensive, and maintenance-free alternative. However, most renewable energy sources are unstable and intermittent due to dynamically changing environmental conditions. Therefore, it poses a challenge for the traditional design methodology, i.e., optimizing the energy efficiency regardless of the power source.

Another challenge on the power supply of the embedded system design is the widely-used voltage overscaling (VOS) technique. VOS has been developed as an effective solution to quadratically reduce the power consumption of the integrated circuits under limited power supply. However, the low power design of VOS is realized at the cost of performance tradeoff of the embedded systems due to the hardware error incurred by the scaled supply voltage. The adaptation of VOS technique brings in more opportunities and freedom to the energy-efficient design, on the other hand, it makes the traditional design unsuitable any more.

1.2 Thesis Contributions

In this dissertation, we focus on optimizing power consumption of the embedded systems when the power supply can not be regarded as a fixed source. In particular, we identify four commonly-used signal processing units, which dominate the power consumption of most embedded systems, and analyze the interplay between the signal processing in the embedded systems and the properties of the power supply, and then propose four power supply aware techniques to improve

the energy efficiency of the embedded systems.

In this dissertation, we have made the following contributions:

- In Chapter 2, we proposed the energy-adaptive modulation scheme [1,2] to dynamically adjust the modulation scheme to deal with time-varying wireless channel conditions and non-deterministic renewable energy levels in a coherent manner to maximize the data rate of RF circuits of the embedded systems.

- In Chapter 3, we developed a progressive performance tuning approach [3,4] to dynamically determine an acceptable signal processing performance in accordance with the changing energy level at runtime. Distinct from the traditional approach, the proposed technique jointly considered the non-deterministic characteristics of renewable energy and the unique relationship between signal processing performance and the required energy consumption.

- In Chapter 4, we developed a link and energy adaptive UWB-based sensing technique [5,6] to improve the detection time coverage and detection range coverage for self-sustained embedded applications. By jointly exploiting the link information between the transmitter and receiver of the UWB pulse radar, and the non-deterministic characteristics of the renewable energy, the proposed technique dynamically adjusts the pulse repetition frequency

of the UWB radar to enhance the sustainable operation under the unreliable energy supply.

- In Chater 5, we proposed a low-power LDPC decoder design [7] by exploiting inherent memory error statistics due to voltage scaling. By analyzing the error sensitivity to the decoding performance at different memory bits and memory locations in the LDPC decoder, the scaled supply voltage is applied to memory bits with high algorithmic error-tolerance capability to reduce the memory power consumption while mitigating the impact on decoding performance.

Chapter 2

RF Power Management via Energy-adaptive Modulation for Self-powered Systems

This chapter presents a system design technique for improving the energy efficiency of RF circuits powered by renewable energy sources. Different from conventional systems, the operation of self-powered RF circuits is largely constrained by two factors: time-varying channel conditions and non-deterministic renewable energy levels. The proposed technique dynamically adjusts the modulation scheme to deal with these two factors in a coherent manner. This is an effective way to maximize the data rate of RF circuits while maintaining the required performance under unstable energy supplies. Some practical issues, such as the battery aging effect, have been investigated. The proposed technique is shown to be robust and insensitive to these issues. A detailed VLSI implementation is developed with negligible energy overhead. Simulation results demonstrate that the proposed technique outperforms conventional RF circuits based on the fixed modulation scheme under various channel and energy conditions.

2.1 Introduction

Exploiting renewable natural resources to power autonomous and distributed embedded systems, such as wireless sensor networks (WSN) [8], self-organizing microrobots [9], and medical implantable devices [10], has gained significant interest recently [11–13]. While many of these systems can be powered by batteries, frequent recharge and maintenance is costly if not impossible. Fortunately, renewable energy technologies such as energy harvesting from the environment offer a sustainable, inexpensive, and maintenance-free alternative. However, most renewable energy sources are non-deterministic due to dynamically changing environmental conditions. Therefore, it is critical to improve the energy efficiency of self-powered systems for reliable and durable operations.

Many techniques have been proposed to deal with this challenging problem at different levels of design hierarchy. At the circuit level, a self-timed circuit with AC power supply was developed in [14] to eliminate power electronics in energy harvesting circuits. A low-power maximum power point tracking (MPPT) circuit was proposed in [15] to maximize the efficiency of transferring solar energy to rechargeable batteries. At the algorithm level, a harvesting-aware scheduling algorithm was introduced in [16] to handle the uncertainties in solar energy. In [17], an energy prediction algorithm was developed to predict the solar energy profile and then adjust the duty cycle accordingly to maximize the sensor performance. A game-theoretic approach was derived in [18] to obtain the optimal sleep and

wake-up strategies for improving energy efficiency. At the system level, various self-powered embedded systems have been developed [19–22] for prototype exploration.

While a lot of effort has been directed towards the power reduction and performance improvement, few results exist in jointly exploiting the properties of renewable energy sources and domain-specific information that is typically available in the design of embedded systems. As the performance of self-powered systems relies upon the interaction between application requirements and resource capabilities, these two components need to be bridged so that effective solutions can be derived. One specific example is a solar-powered sensor node that collects information or monitors important infrastructures continually and sends out data by RF circuits through wireless channels. Data rate is an important performance metric because it determines the precision of the sampled data and the amount of information being transmitted. By increasing the data rate, more information can be collected from the field; but on the other hand, the power consumption of RF circuits will become significant and may evolve into the limiting factor.

In this chapter, we develop a system-level design technique that utilizes energy-adaptive modulation to improve the data rate of RF circuits powered by renewable energy sources. In contrast to most conventional wireless systems that employ a pre-determined modulation scheme, our approach exploits an interesting interplay among channel conditions, available renewable energy, and RF data rates

subject to a given application requirement such as signal-to-noise ratio (SNR) or bit error rate (BER). Specifically, the proposed technique dynamically adjusts the modulation scheme based on a composite effect of wireless channel conditions and renewable energy characteristics. This allows RF circuits to effectively cope with the non-deterministic energy supply while achieving significant improvement in performance. The energy overhead of the proposed technique is negligible, making it suitable for a wide range of self-powered wireless systems. We also study several practical issues such as the battery aging effect. It is shown that the proposed technique is robust and insensitive to battery aging. Simulation results demonstrate that the proposed technique outperforms the conventional systems by a large margin.

It is worth mentioning that adaptive transceiver designs, such as adaptive modulation and coding (AMC) [23–25], low-power adaptive RF systems [26], and use-aware adaptive MIMO RF receiver systems [27], had been studied in the past. Most of these systems exploit the channel conditions with the underlying assumption that the energy supply is always stable though limited. In contrast, our work targets RF systems powered by renewable energy that is inherently non-deterministic. All energy components are essentially variables with large uncertainties and changing dynamically with the time. The modulation schemes have to be determined based on the statistical effects of renewable energy and channel conditions in a coherent manner.

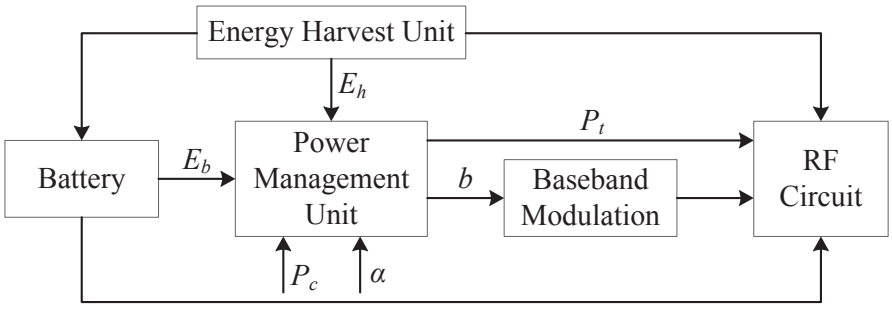

Fig. 2.1: Model of a self-powered system.

The rest of the chapter is organized as follows. In Section 2.2, we describe the system model of RF circuits powered by renewable energy. In Section 2.3, we propose the energy-adaptive modulation technique to maximize the data rate of self-powered RF circuits. Section 2.4 presents the VLSI implementation of the proposed technique and discusses the related energy overhead. Section 2.5 evaluates the proposed technique under different renewable energy models. Finally, the conclusions are summarized in Section 2.6.

2.2 System Model

In this section, we present the model of self-powered RF circuits. This model will be utilized to develop the energy-adaptive modulation technique.

2.2.1 RF Circuits with Renewable Energy

We consider a generic system (e.g., a wireless sensor node) powered by renewable energy sources. As shown in Fig. 2.1, the energy harvest unit (EHU) collects the energy E_h from environmental sources such as solar radiation. The harvested energy is consumed by the RF circuit to transmit information symbols. If the energy cannot be fully consumed, a portion of E_h will be stored into a rechargeable battery for future use. On the other hand, if the energy generated from the EHU is not sufficient to support the required operation, the gap is filled by the battery. This process is controlled by the power management unit (PMU), which collects the necessary information at runtime such as the renewable energy level E_h, the battery remaining charge E_b, and the channel gain α of the current time slot, all of which can be estimated using existing methods with sufficient accuracy. Based on these information, a decision is made to allocate a suitable amount of transmit power P_t to the transmitter.

Figure 2.2 illustrates the block diagram of a standard transmitter. Modulated symbols are first converted by the digital-to-analog converter (DAC) into the analog signal and then pass through the filter and up-convertor (mixer and local oscillator (LO)) to the radio frequency. The signal is then amplified by the variable gain power amplifier (VGPA), whose power consumption is the dominant component in the transmitter. The variable gain controller (VGC) in the VGPA is controlled by PMU. At the beginning of each time slot, VGC determines the

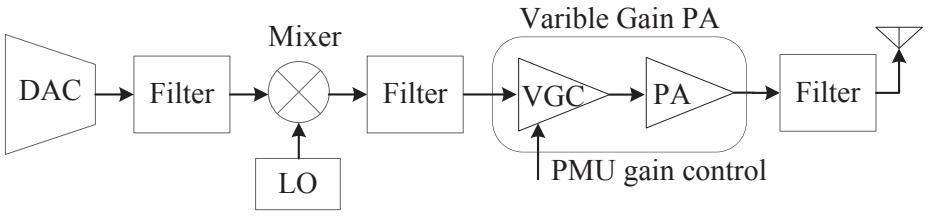

Fig. 2.2: Block diagram of transmitters.

power gain of the power amplifier (PA) according to the level of transmit power P_t assigned by PMU.

2.2.2 Power Model

The power consumption of the transmitter is a direct function of system performance requirements. Through wireless channels, the channel gain α affects the signal quality at the receiver. The signal-to-noise ratio (SNR) at the receiver is defined as

$$\gamma = \frac{\alpha P_s}{P_n}, \tag{2.1}$$

where P_s and P_n denote the transmitted signal power and channel noise power, respectively. It is clear that when the channel gain α is large, the transmitted signal power P_s can be reduced under the same SNR requirement, thereby allowing low-power operations in the transmitter.

In Fig. 2.2, the power consumption P_t of the transmitter consists of three

components

$$P_t = P_s + P_{amp} + P_c = \frac{\xi}{\eta} P_s + P_c, \tag{2.2}$$

where P_{amp} is the circuit power consumption of the PA, ξ and η are the peak-to-average power ratio (PAPR) and the drain efficiency of the PA [28], respectively. Note that the combination of P_s and P_{amp} in (2.2) is the power consumption of the PA, P_{VGPA}, which can be expressed as $P_{VGPA} = \frac{\xi}{\eta} P_s$ because it is related to the transmitted signal power P_s. The other parts of the transmitter, such as mixer, filter, DAC and LO, consume a relatively small amount of power $P_c = P_{mixer} + P_{filter} + P_{DAC} + P_{LO}$. Note that the power consumption of DAC actually varies with different PAPR, e.g., more power will be consumed by DAC under high level modulation schemes. However, this variation is very small (less than 5% as indicated in [29]), and thus it is reasonable to model P_c as a constant [30] within the scope of this work.

The total power consumption of the PA, P_{VGPA}, is the dominant component in the transmitter. In this work a linear power amplifier model [31] is considered. This is because for wireless sensor nodes the power consumption of the PA is usually in the range of mW due to the short transmission distance between the nodes. Thus, the PA typically works in the linear region to preserve RF signal linearity after amplification. Note that the proposed technique does not depend on the perfectly linear relationship between the PA power consumption and the transmission power. As long as the PA power consumption increases with trans-

mission power, the proposed technique can achieve better performance than the existing techniques.

Utilizing P_s from (2.1), P_{VGPA} can be recast as

$$P_{VGPA} = \frac{\xi \gamma P_n}{\eta \alpha}, \tag{2.3}$$

where both ξ and γ are related to the modulation scheme, as discussed next, and the channel gain α can be estimated in realtime because wireless sensor nodes typically have a large coherence time for transferring the channel state information between the transmitter and the receiver.

2.2.3 Implications of Modulation on RF Power Consumption

Choosing an appropriate modulation scheme for self-powered RF circuits involves careful tradeoffs between energy availability and system performance requirements. From (2.3), the PAPR ξ can be expressed as [32]

$$\xi = \frac{\max |S_t|^2}{\mathbf{E}\left[|S_t|^2\right]}, \tag{2.4}$$

where S_t and $\mathbf{E}\left[|S_t|^2\right]$ denote the modulated symbols and the average signal power of the symbols, respectively. In general, a higher level modulation scheme (e.g, larger signal constellation) introduces a larger PAPR [32].

On the other hand, the SNR γ at the receiver is a function of wireless channel characteristics. While the proposed technique does not depend on any specific channel model, the Rayleigh fading channel is assumed in this work for the

purpose of illustration. Note that other channel impairments, such as interferers, are usually handled by different techniques such as filtering, error-control coding, and/or higher layer solutions (e.g., code division multiple access (CDMA)), and thus are not considered here.

For the Rayleigh fading channel, the channel gain α in (2.3) follows the chi-square distribution [33], expressed as

$$f(\alpha) = \frac{1}{\Omega} e^{-\alpha/\Omega}. \tag{2.5}$$

The SNR γ can be determined when the quadrature amplitude modulation (QAM) is applied [34], as

$$\gamma = \frac{2(2^b - 1)}{3\left[\frac{1}{(1-2P_e)^2} - 1\right]} = C(2^b - 1), \tag{2.6}$$

where b and P_e are the number of bits per symbol (determined by the modulation scheme) and the bit error rate (BER), respectively. If P_e is fixed by the pre-specified performance requirement, we can combine it with other constants in (2.6) into a constant term C. Clearly, from the relationship between γ and b, a higher modulation level is preferred when the channel condition is good. This fact has been exploited in many conventional wireless systems when the energy supply is unlimited or stable.

Note that other design techniques at the different layers of wireless communication systems, such as error control coding at the baseband, also affect the tradeoff between power consumption, data rate and BER. Since our work focuses

primarily on the selection of modulation schemes for RF front-ends, the tradeoff on power, data rate and BER is the net effect of modulation schemes exclusive of ECC. Modeling and investigating the relationship between transceiver power and ECC under the renewable energy supply is an important topic for our future study.

2.3 Energy-Adaptive Modulation for RF Power Management

In this section, we will develop an energy-adaptive modulation technique to improve the efficiency of self-powered RF circuits. Considering the fact that renewable energy sources are non-deterministic, the proposed technique dynamically adjusts the modulation scheme in accordance with the changing energy levels and channel conditions to maximize the data rate of RF circuits. Several important practical issues, such as the battery aging effect, will be investigated to assess the effectiveness of the proposed technique.

2.3.1 Motivation

From (2.3), the power consumption P_{VGPA}, the dominant component in the transmitter, is inversely proportional to the channel gain α. Intuitively, when the channel gain α is large (e.g., under good channel conditions), it is preferable to use a high-level modulation scheme to improve the data rate. While this is generally true for conventional systems powered by stable power sources, it may

not be feasible in a system powered by renewable energy. As indicated in (2.4) and (2.6), a higher level modulation scheme has larger PAPR ξ and b, both resulting in a larger power consumption P_{VGPA} that may not be feasible due to the non-deterministic energy harvesting process. Thus, there exists an interesting interplay among channel conditions, available renewable energy, and RF data rates subject to a given performance requirement such as SNR or BER. For this consideration, it is important to develop a scheme that can improve the energy efficiency of RF circuits by adaptively adjusting the modulation scheme based on a composite effect of channel conditions and renewable energy levels. Existing energy-constrained adaptive modulation techniques [30], however, only handle the situation with limited battery capacity without considering the unique features of renewable energy.

To maximize the data rate, the RF circuit should try to fully utilize the available harvested energy and the energy stored in the battery when the channel condition is good enough (e.g., larger than a threshold α_{th} [35]), such as

$$\begin{aligned} E_b + E_h &= T_{on}(P_c + \tfrac{\xi\gamma P_n}{\eta\alpha}), \\ T_{on} &\leq T_s, \end{aligned} \tag{2.7}$$

where E_b and E_h represent the available energy in the battery and the energy collected by the EHU, respectively, that will be used in one time slot, T_s denotes the duration of one time slot in wireless transmission, and T_{on} is the on time of the transmitter in the current time slot. In this work, both E_b and E_h are

replenishable and are treated as random variables due to the non-deterministic energy harvesting process. Also in practical systems, T_{on} is bounded by T_s even if the available energy is sufficiently large.

When the modulation scheme is adjusted dynamically, the data rate at each time slot will be different as it is determined by the selected modulation scheme and the on time of the transmitter. Given the number of bits per symbol b and the duty cycle $\lambda = T_{on}/T_s$, the effective data rate (assuming a fixed symbol rate) of a time slot can be expressed as

$$\begin{aligned} b\lambda &= b\frac{T_{on}}{T_s} \\ &= \frac{E_b + E_h}{T_s(\frac{P_c}{b} + \frac{\xi C P_n(2^b-1)}{\eta \alpha b})}, \end{aligned} \tag{2.8}$$

where (2.8) is obtained by substituting T_{on} and γ from (2.7) and (2.6), respectively. Note that the effective data rate $b\lambda$ could be smaller than 1bit/use if T_{on} is smaller than T_s. The actual data rate can be obtained by multiplying with the symbol rate.

While the proposed technique can be applied to different modulation schemes, in this work we will consider M-QAM modulation so that the key idea of our approach can be explained clearly. Here M represents the modulation level that is adjusted dynamically based on the channel conditions and renewable energy levels. Since $M = 2^b$ for M-QAM, the value of M should be selected to maximize the data rate, as expressed in (2.8).

Note that since the channel gain α and available energy E_b and E_h change

continually, the value of M will be different in each time slot and thus needs to be determined dynamically at runtime.

2.3.2 Energy-adaptive Modulation

To derive the energy-adaptive modulation technique, we need to know the channel gain α and available energy E_b and E_h. The channel gain α can be estimated using channel estimation algorithms [36] at the beginning of each time slot. This is a commonly employed procedure in many wireless communication systems [37,38]. Techniques for monitoring the battery condition are also well-developed [39] and applied in most mobile systems. Similarly, many algorithms have been developed for estimating the renewable energy at runtime with sufficient accuracy [40]. These topics are beyond the scope of this work.

We start with a simple case of choosing between $b = 1$ and $b = 2$, i.e., 2-QAM and 4-QAM. Note that ξ_2 and ξ_4 are the PAPR parameters for 2-QAM and 4-QAM, respectively, both equal to 1 according to (2.4). From (2.8), 4-QAM is selected for a time slot under the following condition

$$\frac{E_b + E_h}{T_s(\frac{P_c}{2} + \frac{3CP_n}{2\eta\alpha})} > \frac{E_b + E_h}{T_s(P_c + \frac{CP_n}{\eta\alpha})}, \tag{2.9}$$

which reflects the scenario that, when the channel gain α is relatively large, a higher level modulation scheme will be chosen to maximize the data rate. In this case, the main factor to determine the modulation scheme is the channel condition. According to (2.9), while the transmitter using 4-QAM consumes more power and

may lead to a shorter on time T_{on}, the data rate is still larger than that using 2-QAM under the same energy level if α is larger than a threshold (determined in (2.13)).

On the other hand, when the channel gain α is small, a low level modulation scheme is preferable for performance consideration. Interestingly, the modulation scheme also needs to be determined by the available energy level. If energy is low, then 2-QAM should be selected when

$$1 > \frac{E_b + E_h}{T_s(P_c + \frac{CP_n}{\eta\alpha})} > \frac{E_b + E_h}{T_s(\frac{P_c}{2} + \frac{3CP_n}{2\eta\alpha})}, \tag{2.10}$$

where in this case the on time T_{on} is smaller than the duration of the time slot T_s; or when

$$\frac{E_b + E_h}{T_s(P_c + \frac{CP_n}{\eta\alpha})} \geq 1 > \frac{E_b + E_h}{T_s(\frac{P_c}{2} + \frac{3CP_n}{2\eta\alpha})}, \tag{2.11}$$

where in this case the on time T_{on} of the transmitter using 2-QAM is actually bounded by T_s (i.e., $b\lambda = 1$), but the data rate of the transmitter using 4-QAM is smaller than 1bit/use.

However, if energy is sufficient, then the transmitter using 2-QAM may not be able to consume all the available energy even when the duty cycle reaches its maximum (i.e., $T_{on} = T_s$). To avoid the waste of energy and possible battery overflow, the higher level modulation scheme is selected when

$$\frac{E_b + E_h}{T_s(P_c + \frac{CP_n}{\eta\alpha})} > \frac{E_b + E_h}{T_s(\frac{P_c}{2} + \frac{3CP_n}{2\eta\alpha})} > 1. \tag{2.12}$$

As in practice $b\lambda$ cannot be larger than 1 when $b = 1$ (i.e., 2-QAM), the

first term in (2.12) (i.e., the data rate of the transmitter using 2-QAM) is actually bounded by 1 while the second term (i.e., the data rate of the transmitter using 4-QAM) is larger than 1. Thus, 4-QAM should be selected.

Rearranging (2.9) and (2.12) as a function of the channel gain α, we obtain

$$\alpha > \frac{CP_n}{\eta P_c}, \tag{2.13}$$

and

$$\frac{CP_n}{\eta P_c} > \alpha > \frac{3CP_n}{2\eta(\frac{E_b+E_h}{T_s} - \frac{P_c}{2})}, \tag{2.14}$$

from (2.9) and (2.12), respectively. Combining these two conditions, the 4-QAM scheme should be selected for the transmitter if the channel gain α is larger than $\alpha_{2,4}$, expressed as

$$\alpha_{2,4} = \frac{3CP_n}{2\eta(\frac{E_b+E_h}{T_s} - \frac{P_c}{2})}, \tag{2.15}$$

where $\alpha_{2,4}$ is a function of renewable energy and the energy stored in the battery. On the other hand, when $\alpha < \alpha_{2,4}$, 2-QAM will be selected. Clearly, the proposed technique selects the appropriate modulation scheme based on both channel and energy conditions.

Extending the above procedure, we can also derive the channel gain threshold $\alpha_{4,16}$ between 4-QAM and 16-QAM, and $\alpha_{16,64}$ between 16-QAM and 64-QAM. Note that higher modulation schemes (such as 256-QAM and higher) are seldom used in self-powered systems due to the exponentially increased complexity. This is further shown in Section 2.5, where simulation results indicate that the pro-

posed technique usually chooses a modulation scheme lower than 64-QAM. Also, non-square QAM schemes (e.g., 8-QAM) are not considered either mainly because they lead to an incompatible hardware implementation (see Section 2.4).

From (2.8), 16-QAM will be selected if the resulted data rate of the transmitter is larger than that using 2-QAM, 4-QAM and 64-QAM, i.e.,

$$\frac{E_b + E_h}{T_s(\frac{P_c}{4} + \frac{15\xi_{16}CP_n}{4\eta\alpha})} > \frac{E_b + E_h}{T_s(P_c + \frac{\xi_2 CP_n}{\eta\alpha})}, \tag{2.16}$$

$$\frac{E_b + E_h}{T_s(\frac{P_c}{4} + \frac{15\xi_{16}CP_n}{4\eta\alpha})} > \frac{E_b + E_h}{T_s(\frac{P_c}{2} + \frac{3\xi_4 CP_n}{2\eta\alpha})}, \tag{2.17}$$

$$4 > \frac{E_b + E_h}{T_s(\frac{P_c}{4} + \frac{15\xi_{16}CP_n}{4\eta\alpha})} > \frac{E_b + E_h}{T_s(\frac{P_c}{6} + \frac{21\xi_{64}CP_n}{2\eta\alpha})}, \tag{2.18}$$

where $\xi_{16} = 1.8$ and $\xi_{64} = 2.33$ are the PAPR parameters of 16-QAM and 64-QAM, respectively. Similar to (2.9), the above conditions represent the relatively large channel gain α in the current time slot, while the available energy is not sufficient to support 64-QAM.

In addition, 16-QAM should also be selected when the energy supply and channel gain satisfy the following conditions,

$$\frac{E_b + E_h}{T_s(P_c + \frac{\xi_2 CP_n}{\eta\alpha})} \geq \frac{E_b + E_h}{T_s(\frac{P_c}{4} + \frac{15\xi_{16}CP_n}{4\eta\alpha})} > 1, \tag{2.19}$$

$$\frac{E_b + E_h}{T_s(\frac{P_c}{2} + \frac{3\xi_4 CP_n}{2\eta\alpha})} \geq \frac{E_b + E_h}{T_s(\frac{P_c}{4} + \frac{15\xi_{16}CP_n}{4\eta\alpha})} > 2, \tag{2.20}$$

$$\frac{E_b + E_h}{T_s(\frac{P_c}{4} + \frac{15\xi_{16}CP_n}{4\eta\alpha})} \geq 4 > \frac{E_b + E_h}{T_s(\frac{P_c}{6} + \frac{21\xi_{64}CP_n}{2\eta\alpha})}. \tag{2.21}$$

Note that (2.19) and (2.20) reflect a similar scenario as (2.12), where the transmitter using 2-QAM or 4-QAM cannot fully utilize the available energy. Since the on time T_{on} is bounded by T_s, $b\lambda$ is bounded by 1 and 2 for 2-QAM and 4-QAM, respectively. On the other hand, the condition in (2.21) indicates that, while the available energy is sufficient, the channel gain is not high enough to support 64-QAM.

Rearrange (2.16)–(2.21), we obtain the range of channel gains, within which 16-QAM should be selected for the transmitter to transmit information, as

$$\frac{48.93CP_n}{\eta(\frac{E_b+E_h}{2T_s}-\frac{P_c}{3})} > \alpha \geq \frac{27CP_n}{\eta(\frac{2(E_b+E_h)}{T_s}-P_c)}. \tag{2.22}$$

From (2.22), the thresholds $\alpha_{4,16}$ and $\alpha_{16,64}$ can be determined as,

$$\alpha_{4,16} = \frac{27CP_n}{\eta(\frac{2(E_b+E_h)}{T_s}-P_c)}, \tag{2.23}$$

$$\alpha_{16,64} = \frac{48.93CP_n}{\eta(\frac{E_b+E_h}{2T_s}-\frac{P_c}{3})}. \tag{2.24}$$

2.3.3 Performance Measurement

Note that the above discussion is based on one time slot in wireless transmission. Considering the fact that channel conditions and renewable energy levels are non-deterministic and mutually independent, we can derive the average data rate, which is a statistical measure of the performance for the proposed technique. For the purpose of illustration, we assume that α follows the chi-square distribution as expressed in (2.5), and the battery energy has a uniform distribution ranging

from zero to the maximum capacity E^b_{max}. The average data rate is obtained as

$$\mathbf{E}(b\lambda_M) = \frac{E^b_{max}/2 + E(E_h)}{T_s}\left[\int_{\alpha_{th}}^{\mu_{2,4}} \frac{f(\alpha)}{P_c + \frac{\xi_2 CP_n}{\eta\alpha}}d\alpha + \int_{\mu_{2,4}}^{\mu_{4,16}} \frac{f(\alpha)}{\frac{P_c}{2} + \frac{3\xi_4 CP_n}{2\eta\alpha}}d\alpha + \int_{\mu_{4,16}}^{\mu_{16,64}} \frac{f(\alpha)}{\frac{P_c}{4} + \frac{15\xi_{16} CP_n}{4\eta\alpha}}d\alpha + \int_{\mu_{16,64}}^{\infty} \frac{f(\alpha)}{\frac{P_c}{6} + \frac{21\xi_{64} CP_n}{2\eta\alpha}}f(\alpha)d\alpha\right], \tag{2.25}$$

where

$$\begin{aligned}
\mu_{2,4} &= \mathbf{E}(\alpha_{2,4}) = \frac{3CP_n}{2\eta(\frac{E^b_{max}/2+\mathbf{E}(E_h)}{T_s} - \frac{P_c}{2})}, \\
\mu_{4,16} &= \mathbf{E}(\alpha_{4,16}) = \frac{27CP_n}{2\eta(\frac{E^b_{max}/2+\mathbf{E}(E_h)}{T_s} - \frac{P_c}{2})}, \\
\mu_{16,64} &= \mathbf{E}(\alpha_{16,64}) = \frac{48.93CP_n}{\eta(\frac{E^b_{max}/2+\mathbf{E}(E_h)}{2T_s} - \frac{P_c}{3})}.
\end{aligned} \tag{2.26}$$

Note that (2.25) is derived by considering all the possible modulation schemes (2- to 64-QAM in this study). However, it is known that higher level modulations (e.g., 16-QAM and 64-QAM) will consume more energy. Also, higher level modulations are usually selected under very good channel conditions, which may occur rarely in a fading channel. Thus, it is expected that the main contributions to the average data rate will come from lower level modulation schemes (e.g., 2-QAM and 4-QAM). This can be seen from (2.25), where the integral terms corresponding to 16-QAM and 64-QAM decrease quickly as compared with those of 2-QAM and 4-QAM. To simplify the performance analysis, the average data rate can be approximated by using the first two integrals in (2.25), i.e., the contributions from higher modulation schemes are ignored with minor impact on accuracy.

Note that while the above analysis assumes a specific channel model and battery energy distribution for the purpose of illustration, the proposed technique provides a general solution that does not depend on any of these models.

2.3.4 Battery Issues

The rechargeable battery plays a key role in self-powered systems. With the repeated charging and discharging, the battery capacity will decrease gradually. This is referred to as the battery aging effect. Conventional systems with a fixed modulation scheme may have to stop working frequently because of the degradation in battery capacity. In contrast, the proposed technique will try to avoid using high-level modulation schemes under such circumstance. This can be seen from (2.25) and (2.26), where $\mu_{i,j}$ increases as E^b_{max} reduces, i.e., it becomes less likely to choose high-level modulation schemes due to their high energy cost. Instead of shutting down the RF circuit when the battery energy is insufficient, the proposed technique will automatically switch to a low-level (and low-power) modulation scheme (e.g., 2-QAM) to compensate for the battery aging effect. Also note that the probability density function $f(\alpha)$ of the channel gain decreases with α (see (2.5)). As E^b_{max} reduces ($\mu_{i,j}$ increases), we expect the average data rate to be dominated by low-level modulation schemes, such as 2-QAM.

Although the data rate of 2-QAM is relatively small, the chance of operating with 2-QAM (instead of shutting down the RF circuit) will increase. As a result,

our technique is relatively insensitive to battery aging. Specifically, by using lower level modulation schemes, a relatively stable data rate can be maintained. This is verified by the simulation results in Section 2.5.

As in practice the battery capacity is limited, battery overflow may occur. This is particularly the case when the RF circuit is turned off under bad channel conditions, while the renewable energy is sufficient. If the battery capacity is reached, the extra energy cannot be stored, which should be avoided in self-powered systems. As battery overflow usually occurs under bad channel conditions but high renewable energy levels, one effective way to address this problem is to exploit error control coding (ECC) [41] on the baseband signal, so that the SNR requirement can be relaxed and the RF circuit can work under bad channel conditions. This approach, however, involves some tradeoffs between the effective data rate (as ECC will add redundancy on transmitted data), performance, and overhead (e.g., the power consumption of ECC circuits). Exploiting channel/source coding for self-powered systems is an important topic for our future study.

2.3.5 Power Management Scheme

The proposed power management scheme exploiting adaptive modulation for self-powered RF circuits is summarized in Procedure 1. Here, channel gain α, harvested energy E_i^h, and stored battery energy E_i^b are time-varying and thus are treated as random variables, while the noise power P_n and battery capacity E_{max}^b

are relatively stable and thus are considered as constants. Note that in Section 2.5 we will study the battery aging effect related to E^b_{max}. The SNR requirement γ and PAPR ξ are determined by the specific application and the selected modulation scheme.

At the beginning of each time slot, the renewable energy is estimated and the thresholds $\alpha_{i,j}$'s are derived for different modulation schemes. The channel gain is estimated to determine the modulation scheme, which also decides the duty cycle T_{on} of the current time slot. These information are utilized to adjust the modulation circuit and the VGPA in the transmitter. If α is too small (e.g., less than α_{th} [35]), the RF circuit are turned off and the harvested energy is stored in the battery for future use.

2.4 Implementation

In this section, we present the VLSI design of the proposed energy-adaptive modulation technique to demonstrate that our technique can be easily implemented without introducing large overheads. We focus on the implementation of new functions such as the power management unit (PMU) and baseband modulation unit (BMU), as shown in Fig. 2.1. A key requirement is to ensure hardware compatibility for different modulation levels so that the transmitter can be made adaptive at runtime. Due to this consideration, non-square QAM schemes (e.g., 8-QAM) are excluded due to their unbalanced I and Q channels, which will need

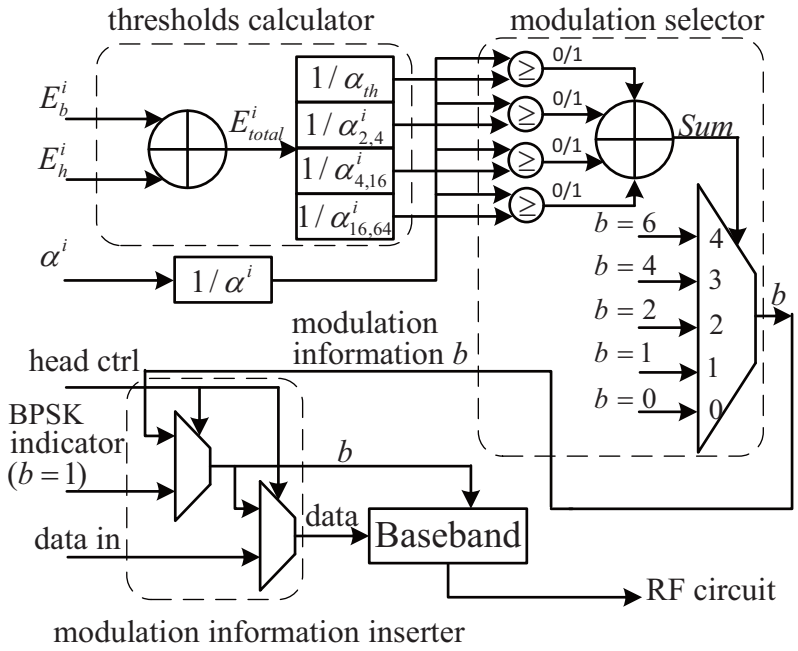

Fig. 2.3: Implementation of power management unit.

a different hardware architecture from square QAM schemes. We will also discuss the receiver design for the proposed technique. Finally, the overhead of the proposed technique will be assessed.

2.4.1 Power Management Unit

Figure 2.3 shows the implementation of the power management unit (PMU). The PMU consists of three modules: threshold calculation, modulation selection, and modulation information insertion. The threshold calculation module determines the thresholds $\alpha_{2,4}^i$, $\alpha_{4,16}^i$, and $\alpha_{16,64}^i$ using (2.15), (2.23), and (2.24) based on the total energy E_{total}^i from the harvested energy and the battery in the i^{th} time slot.

As in most self-powered systems, the renewable energy can be estimated by the existing energy prediction schemes, which usually operate at a much lower frequency (e.g., once per time slot) and thus the energy overhead can be ignored. Also, battery management unit, which is the standard component in mobile devices, can provide the battery status and handle battery overflow. Since the design of energy predictors and battery meters is beyond the scope of this work, they are not shown in Fig. 2.3.

Direct implementation of (2.15), (2.23), and (2.24) involves large energy overhead as they require the inversion operation on the energy measures. To reduce the overhead, we propose to use the reciprocals of the thresholds to determine the modulation scheme. For example, $\alpha^i_{4,16}$ can be calculated as,

$$\frac{1}{\alpha_{4,16}} = \frac{2\eta}{27CP_nT_s}(E_b + E_h) - \frac{\eta P_c}{27CP_n}, \tag{2.27}$$

where all the variables other than the energy measures are non-changing/static and can be calculated in advance. The hardware implementation of (2.27) only involves linear computations (one multiplication and one substraction) and thus avoid division operation, which is more complicated than multiplication [42]. Therefore, our approach greatly simplifies the hardware implementation and reduces the energy overhead.

All the subsequent comparisons in the modulation selection module are based on the reciprocals of the thresholds, which are the input to the modulation selection module. The channel gain is also represented by its reciprocal $1/\alpha^i$,

which can be obtained from the wireless channel gain estimator [36], a standard component in wireless communication systems. The thresholds will be compared with the channel gain. If the reciprocal of channel gain is smaller than the reciprocal of one threshold, the corresponding comparator will generate a logic "1". The outputs of all the comparators are added up to generate the modulation selection signal. For example, if all the comparators output "1", then 2-QAM ($b = 1$) will be selected as the modulation scheme for the transmitter during the i^{th} time slot.

Once the modulation scheme is determined, this information is inserted into the head of data package so that the selected modulation scheme can be known by the receiver. This information is sent using a default low-power modulation scheme such as 2-QAM. At the beginning of each time slot, the signal *head_ctrl* (control signal to transmit the modulation information) will be valid for a short time and the modulation information is fed into the BMU using the default 2-QAM scheme. The modulation information insertion module is implemented by a two-multiplexer structure, as illustrated in Fig. 2.3. The timing diagram of the power management unit is depicted in Fig. 2.4, where the channel gain thresholds are calculated at the beginning of each time slot.

2.4.2 Baseband Modulation Unit

The value of bits per symbol b is sent to the BMU for transmitting symbols, as shown in Fig. 2.5. The bitstream first passes through a serial-to-parallel (S/P) con-

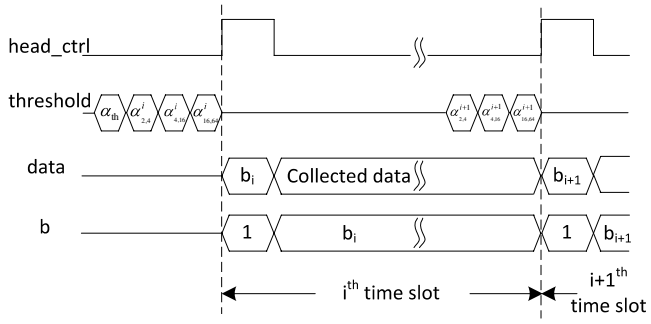

Fig. 2.4: Timing diagram of power management unit.

verter to split into two paralleled bitstreams, in-phase data (*i data*) and quadrature data (*q data*). The main parts of the S/P converter include a counter and a multiplexer [43]. Based on the value of b, the *i data* and *q data* are fed into two identical modules to perform the I/Q channel symbol mapping operations.

To maintain the same average signaling power for the modulated symbols, the symbol values are different when different modulation schemes are utilized. For example, when 2-QAM is chosen, +1 and -1 (normalized values) are used to represent the bit values of 0 and 1, respectively; while with 4-QAM, bit values of 0 and 1 in both *i data* and *q data* are mapped to the symbols with the normalized values of $-\frac{1}{\sqrt{2}}$ and $\frac{1}{\sqrt{2}}$, respectively, in order to maintain the same average signaling power of the QAM symbols. Note that all these mapped symbol values are pre-determined constants that can be implemented as 2's complements in hardware. After symbol mapping, the symbols go through two parallel analog signal processing circuits consisting of digital-to-analog conversion (DAC), filtering, and

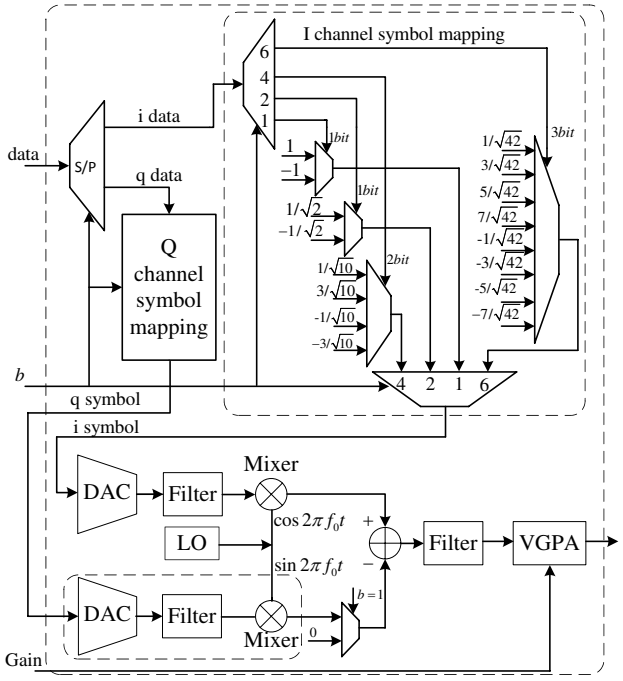

Fig. 2.5: Implementation of baseband modulation unit.

quadrature modulation (mixer and local oscilloscope (LO)). The analog signals are then amplified by the variable gain power amplifier (VGPA), whose gain is determined from (2.3).

2.4.3 Receiver Design

The proposed energy-adaptive modulation technique targets the RF circuit in the transmitter; however, the receiver should also be modified accordingly so that symbols with different modulation schemes can be recovered. We consider a common scenario in distributed sensor nodes where the receiver and the transmitter

are close to each other and thus the optimal modulation scheme is the same as both are under similar energy and channel conditions. Note that for other situations the receiver design may require different approaches that are beyond the scope of this work.

As shown in Fig. 2.6, the only difference between the modified receiver and the conventional one [44] is the modulation information extractor. Other parts, such as the I/Q channel demodulator, are the same. At the beginning of each time slot, the receiver will receive a short head frame containing the modulation information from the transmitter designed in the previous subsections. After synchronization, the receiver will correlate the input with the recovered carrier frequency to obtain the symbols in the head frame, and then demodulate these symbols using 2-QAM demodulation (the default modulation scheme for the head frame, as explained in Section 2.4.1). The value of bits per symbol b is obtained for the following data packages. This value will then be used to demodulate the incoming symbols into the serial data bits in the I/Q demodulators as shown in Fig. 2.6.

2.4.4 Overhead

As this work focuses primarily on the system-level power management, the detailed physical implementation of the transceiver is not presented. However, the hardware overhead related to the physical implementation can be analyzed. The

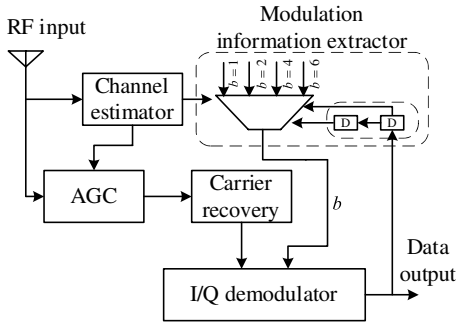

Fig. 2.6: Receiver architecture of the proposed scheme.

new circuit components in the PMU and BMU process baseband signals only. The power consumption of these baseband operations is much smaller than that of the RF circuit (see Section 2.5). In addition, the PMU only operates at the beginning of each time slot to select the modulation scheme. Simulation results in Section 2.5 show that by utilizing the reciprocals of channel gain thresholds (see (2.27)), the energy consumption of the PMU can be further reduced by half. The energy overhead at the receiver is also negligible as compared with the energy consumption of the entire receiver. Thus, the proposed technique introduces very small energy overhead. It is also possible to further reduce the energy overhead by powering off the unused hardware units. For example, when input $b = 1$ (i.e., 2-QAM), we can power off the q bitstream signal processing unit such as the Q channel symbol mapping and DAC in the Q channel in Fig. 2.5.

In addition to the energy overhead, the proposed transceiver design also introduces some extra time delay due to the additional circuits needed to determine

the modulation scheme. This issue, however, is minor for sensor node applications, which are usually operated with low data rates. Note that conventional schemes with fixed modulation may be forced to stop functioning frequently under non-deterministic renewable energy (when the harvested energy is insufficient), as shown in Section 2.5.

2.5 Evaluations

In this section, we evaluate the performance of the proposed energy-adaptive modulation technique. All the results are simulation-based obtained from the transceiver design as discussed in Section 2.4, implemented in a 130nm CMOS process and powered by solar energy as modeled in the next subsection.

2.5.1 Simulation Setup

We adopt two commonly used solar energy models to represent the repetitive yet non-deterministic solar energy patterns. This first one is an analytical model [45,46] that describes the daily solar radiation as

$$P_h(t) = |10 \cdot N(t) \cdot \cos(\frac{t}{70\pi}) \cdot \cos(\frac{t}{100\pi})|, \tag{2.28}$$

where $N(t)$ denotes a normally distributed random variable with zero mean and unit variance. Figure 2.7 shows the results obtained from this model, where the time slot is set to be 0.5 hour. Note that (2.28) describes the short-term (daily) variations in solar energy; it does not consider the long-term seasonal patterns.

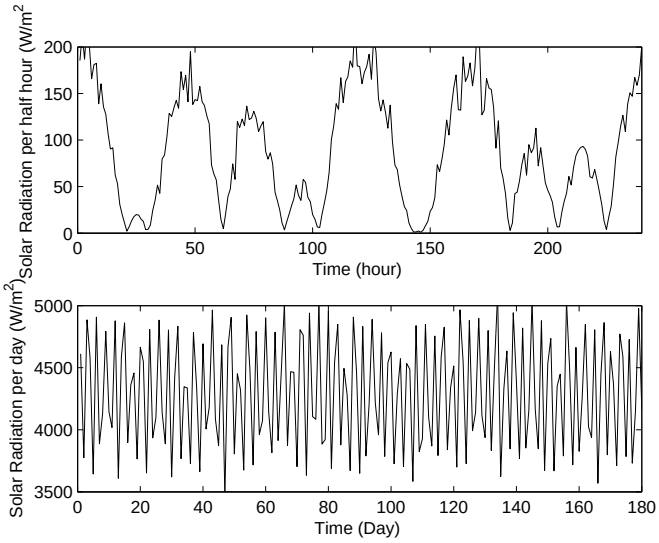

Fig. 2.7: Solar power variations from the analytical model.

The second model is an empirical model from the National Climatic Data Center (NCDC), which provides the environmental measurements collected from various monitoring stations across the United States. The energy profile used in this work is obtained from its Renewable Energy Data Source database [47]. The solar radiation energy for a half year is depicted in Fig. 2.8. In contrast to the analytical model (2.28), this model reflects the long-term seasonal variations in solar radiation. Both models will be applied to investigate the performance of the proposed energy-adaptive modulation technique.

For the purpose of demonstration, we consider the Rayleigh channel model for wireless communications and the channel noise follows the Gaussian distribution with zero mean and unit variance. The channel gain α follows the chi-square

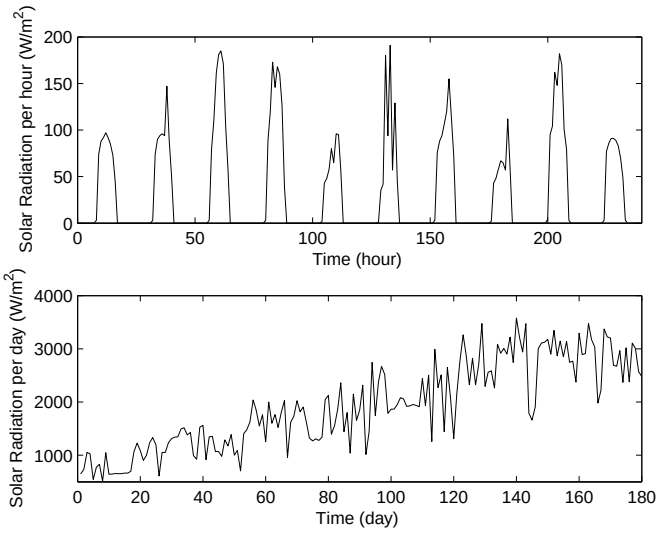

Fig. 2.8: Solar power variations from real measurements by the National Climatic Data Center.

distribution as expressed in (2.5). The battery capacity E^b_{max} is normalized with respect to the average harvested energy of one day. The PAPR ξ of different modulation schemes are 1, 1, 1.8, and 2.33 for 2-, 4-, 16-, and 64-QAM, respectively.

To estimate the power consumption, we simulate our transceiver design in a 130nm CMOS process. Table 2.1 shows the power consumption of BMU. We observed that a higher level modulation scheme introduces a larger power in BMU. This is mainly due to the fact that the higher level modulation scheme needs to use a larger multiplexer (see Fig. 2.5). Table 2.1 also shows that in most time slots 2-QAM and 4-QAM were selected by the proposed technique. This is consistent with our analysis based on (2.25) and (2.26) in Section 2.3.3. The power consumption of

PMU is $5.22\mu W$ when the reciprocals of the thresholds are implemented to determine the modulation scheme (direct implementation of (2.15), (2.23), and (2.24) would cost about $10.63\mu W$). Since PMU involves more complicated arithmetic operations, it introduces larger power overhead. However, different from BMU that works all the time, PMU only works at the beginning of each time slot, thus the energy overhead of PMU is negligible compared with that of BMU. Overall, the proposed technique introduces about 1% of energy overhead as compared to the RF circuit operated under the fixed 2-QAM modulation scheme. Nevertheless, by dynamically adjusting the modulation scheme in accordance with renewable energy levels and channel conditions, the improvement in energy efficiency can easily offset the energy overhead.

2.5.2 Performance Comparisons

Figure 2.9 shows the average data rate achieved in our transceiver design under the first solar energy model (2.28) for several fixed QAM schemes and the proposed technique (denoted as MQAM). The normalized battery capacity is assumed to be 4% of the average harvested energy of one day. These results were obtained under different channel gain threshold α_{th} (see (2.25)) to simulate all possible situations in practice. If the channel gain threshold is small, the RF circuit may be turned on more frequently, but the average data rate is low as only low-level modulation schemes will be used. On the other hand, when the channel gain threshold is large,

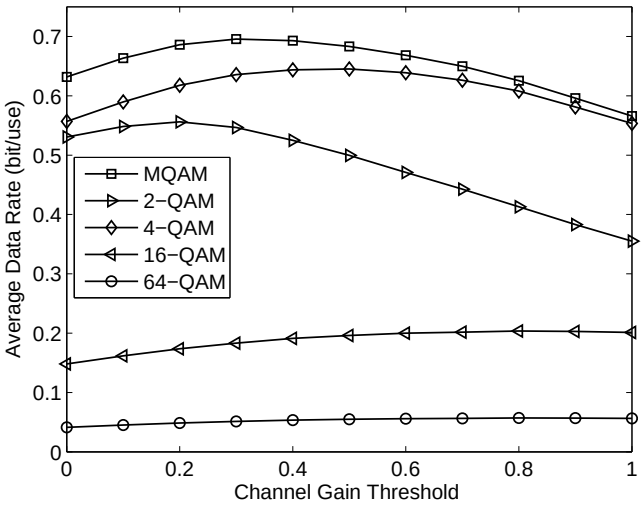

Fig. 2.9: Performance of RF circuits using the fixed QAM and MQAM under the analytical energy model.

the RF circuit will be turned on less frequently (i.e., only under the good channel condition), and thus the average data rate is also low. Since MQAM dynamically selects the best modulation scheme from 2- to 64-QAM at runtime, it outperforms any of the fixed QAM schemes. The maximal data rate (statistical average) of 0.70bit/use is achieved in Fig. 2.9. Note that the average data rate is utilized to quantify the energy efficiency of self-powered RF systems. This is because for these systems we are mainly concerned with how many data to be transmitted using the non-deterministic energy supply, but not simply reducing the power consumption of the system. This is fundamentally different from conventional low-power transceiver designs.

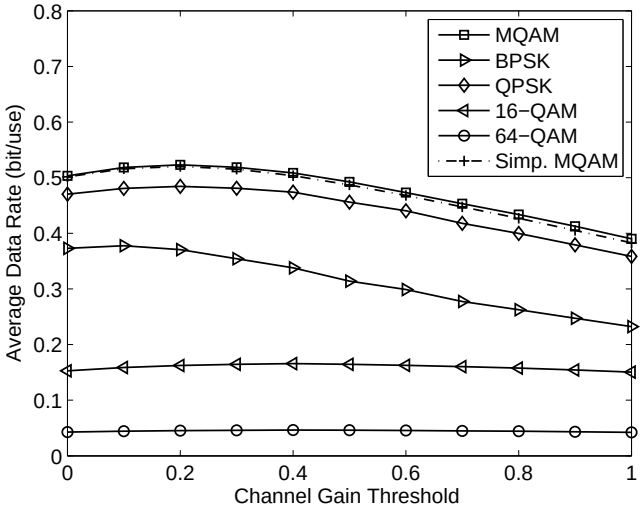

Fig. 2.10: Performance of RF circuits using the fixed QAM and MQAM under the real measurements collected from the National Climatic Data Center.

Figure 2.10 shows the similar performance trends in the fixed QAM schemes and proposed MQAM using the second empirical energy model (see Fig. 2.8). The maximal data rate achieved in the proposed MQAM is 0.52bit/use, less than that in Fig. 2.9. The reason is that the empirical energy model considers both seasonal and daily variations in solar energy, which introduces more uncertainties in the available energy and thus affects the achievable date rate in the RF circuit.

Note that from Figs. 2.9 and 2.10, 4-QAM and 2-QAM show the best performance in most time slots. Thus, we expect that the MQAM will be operated mostly under these two schemes. Considering this observation, we can simplify the

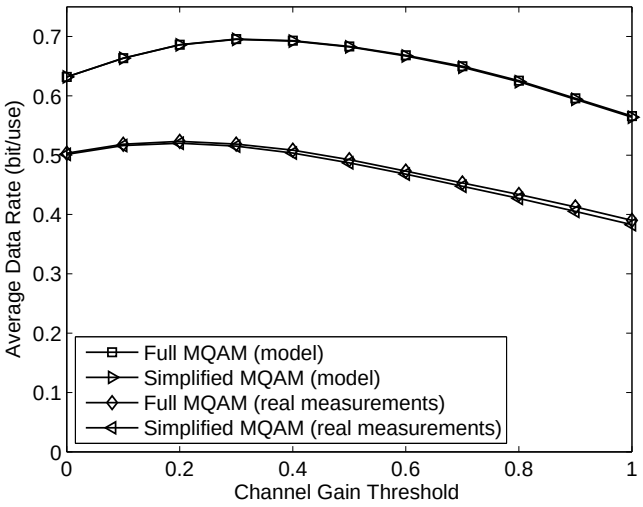

Fig. 2.11: Performance comparison between the simplified MQAM and MQAM.

proposed technique by using the lower-level modulation schemes (e.g., 2-QAM and 4-QAM) only. The performance of this simplified approach is compared with the original MQAM (i.e., using all modulation schemes) in Fig. 2.11. As shown, only minor performance degradation is incurred in terms of data rate loss. Thus, this approach is favorable when further reduction in the hardware/energy overhead is needed.

2.5.3 Implications of Battery Aging

One unique feature of the proposed energy-adaptive modulation technique is to make self-powered RF circuits insensitive to the battery aging effect. As shown in Fig. 2.12, with the reduction of battery capacity, the average data rate of the RF circuit employing MQAM decreases at a slower rate than the fixed modulation

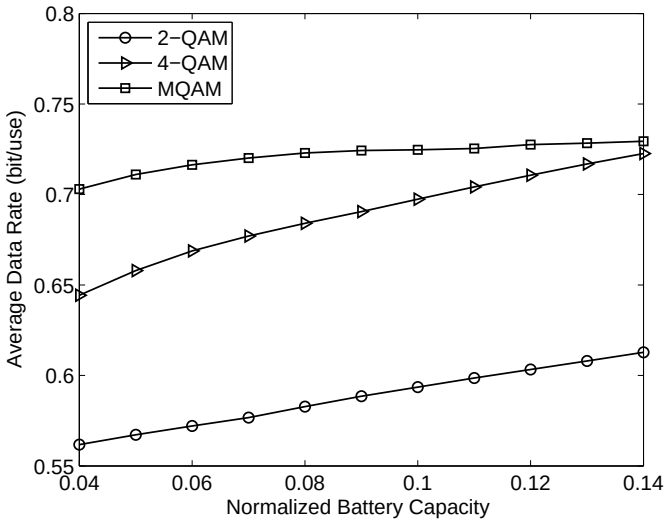

Fig. 2.12: Performance under the battery aging effect.

schemes. Specifically, the reductions of the average data rate are 8.3%, 10.8%, and 3.6% for 2-QAM, 4-QAM, and MQAM, respectively. It is obvious that battery aging has a less impact on MQAM as compared with other modulation schemes. This is consistent with the discussion in Section 2.3.4. The proposed technique can be adjusted to a lower level modulation scheme if necessary to compensate for the battery aging effect. This is because the average data rate is proportional to both the turn-on time of the transmitter and the amount of data being transferred during the turn-on time. Although the fixed 2-QAM consumes the least amount of energy and thus can operate for a longer time in the presence of battery aging, it also transfers the least amount of data. The fixed 4-QAM consumes more energy than 2-QAM and thus may have to be shut down more often if energy is insufficient

(i.e., reduced turn-on time). But when it is on, it can transfer more data than 2-QAM. Thus, overall the average data rate of 4-QAM is larger than that of 2-QAM under the same battery capacity. The proposed technique dynamically adapts the modulation scheme based on the energy availability, enabling both a longer turn-on time and more data being transferred.

2.6 Conclusions

In this chapter, we have developed an energy-adaptive modulation technique to improve the energy efficiency of RF circuits powered by renewable energy sources. By jointly considering the non-deterministic characteristics of renewable energy and statistical channel conditions, the proposed approach exploits adaptive modulation to maximize the data rate of RF circuits. We also investigate the battery issue and assess its impact on the proposed technique. A VLSI implementation of the proposed technique is presented which introduces negligible energy overhead, making the proposed technique suitable for various resource-constrained wireless systems. Future work is directed towards considering the latency constraint of the modulated data, and integrating adaptive modulation with source/channel coding to further improve the performance of self-powered systems.

Algorithm 1: Procedure of Energy-Adaptive Modulation Scheme.

Input:
P_n (Noise power at the receiver)
P_c (RF circuit power consumption)
γ (SNR requirement for the receiver)
ξ (PAPR for different modulation scheme)
α (Channel gain)
E_i^h (Harvested energy at the i^{th} time slot)
E_i^b (Initial battery energy at the i^{th} time slot)
E_{max}^b (Battery capacity)
Output:
b (Number of bits per symbol in modulation)
P_{VGPA} (Power consumption of VGPA)
T_{on} (On-time of the RF circuit)
begin
    1. Determine b by comparing α with channel gain boundary between different QAM schemes;
    % compare channel gain α with the gain bound $\alpha_{2,4}$ between 2-QAM and 4-QAM
    if $\alpha_{2,4} > \alpha > \alpha_{th}$ **then**
        $b = 1$;
    else
        % compare channel gain α with the gain bound $\alpha_{4,16}$ between 4-QAM and 16-QAM
        if $\alpha_{4,16} > \alpha > \alpha_{2,4}$ **then**
            $b = 2$;
        else
            % compare channel gain α with the gain bound $\alpha_{16,64}$ between 16-QAM and 64-QAM
            if $\alpha_{16,64} > \alpha > \alpha_{4,16}$ **then**
                $b = 4$;
            else
                $b = 6$;
            end
        end
    end
    2. P_{VGPA} is determined by (2.3);
    3. T_{on} is determined by (2.7).
end

Table 2.1: Power and Area Overhead of the BMU

	2-QAM	4-QAM	16-QAM	64-QAM
Power Consumption	$2.10\mu W$	$2.16\mu W$	$2.32\mu W$	$2.38\mu W$
Area Overhead	$3469\mu m^2$			
Selection Occurrence	987	320	3	1
Average Power	$2.12\mu W$			

Chapter 3

Energy-adaptive Signal Processing Under Renewable Energy

This chapter presents an energy-adaptive performance management technique for the design of embedded signal processing systems powered by renewable energy sources. By jointly considering the non-deterministic characteristics of renewable energy and the unique relationship between signal processing performance and the required energy consumption, a progressive performance tuning approach is developed to dynamically determine an acceptable signal processing performance in accordance with the changing energy level at runtime. Several practical issues such as energy prediction errors and battery capacity are investigated, and their impacts on the proposed technique are evaluated. The proposed technique is applied to a DCT-based image sensing system. Simulation results demonstrate that by adaptively tuning signal processing kernels with renewable energy, significant improvements in time coverage and energy efficiency can be achieved in the presence of unstable harvested energy.

3.1 Introduction

Many embedded signal processing systems need to support long-term autonomous applications, such as surveillance, real-time control, wireless sensor networks, and monitoring. Exploiting renewable energy from the environment to power these systems [11,48,5,49–52] has emerged as an effective solution. Although renewable energy sources, such as solar, wind, and vibration, are sustainable and maintenance-free, they also feature substantial energy non-determinism. Thus, there exists a challenging problem to ensure acceptable system performance under the unstable renewable energy.

Design methods for improving the energy efficiency of self-sustained systems are fundamentally different from those for conventional battery-powered systems [53,54,7,55,56]. The approaches are needed to transform from minimizing energy utilization to coherent energy/performance adaptation subject to large energy non-determinism. Many techniques have been reported to optimize the energy utilization by considering the renewable energy profile. In [57], a technique was proposed to adjust the duty cycle according to the energy availability in the environment. An energy-aware dynamic voltage and frequency scaling technique was developed in [58] to adjust the execution speed of the processor based on the available renewable energy by exploring the slack time. In [59], a maximum power point tracking scheme was presented to adaptively operate different parts of the circuit to accommodate the amount of harvested energy. In [60], a checkpoint

insertion technique was developed to improve the stability of the system powered by renewable energy.

While many existing work focus on the adjustment of the operation and/or the configuration of self-powered embedded systems based on the renewable energy status, few work exist in jointly exploiting the non-deterministic energy harvesting process and domain-specific information that is typically available in the design of embedded signal processing systems. Most embedded signal processing systems demonstrate a unique relationship between the signal processing performance and the corresponding energy consumption. Specifically, while hardware operations may be the same with similar energy consumption, the resulted outputs usually contribute differently to the algorithmic performance. Consider the implementation of an FIR filter [61] as an example. The multiply-accumulate (MAC) operations contributing to the most significant outputs should be processed with a high priority to minimize the impact of uncertainties in renewable energy sources. Similarly, most information of an image concentrates in the low-frequency coefficients of the discrete cosine transform (DCT), making it necessary to process these coefficients first under the unstable renewable energy. Some emerging applications, such as large-scale neuromorphic computing system [62], and feature selection in wearable sensor networks [63], also represent this kind of feature. More importantly, the relationship between system performance and energy consumption is typically non-linear [64], and thus the renewable energy can be more

efficiently utilized to improve the system performance when the signal quality is low. These unique features inherent in the embedded signal processing systems can lead to new solutions that ensure acceptable system performance under the non-deterministic renewable energy. Note that the domain-specific information varies from system to system, and usually it is related with the system optimization goal, such as low power design [1,2] and enhanced security design [65,66].

In this chapter, we propose an energy-adaptive performance management technique to address the new challenges in the design of renewable energy powered signal processing systems. The basic idea of this technique is to dynamically adjust the system performance in adaptation with the changing renewable energy level. In particular, by considering the non-linear relationship between the performance and energy consumption inherent in the signal processing systems, we resort to a progressive performance tuning approach at runtime to cope with the constraints of unstable energy supply. We also consider practical issues such as harvested energy prediction error and battery capacity and develop corresponding methods to mitigate their impacts on the proposed techniques. Simulation results of a DCT-based image sensing system demonstrate that, by dynamically adjusting the signal processing quality, the overall system performance in terms of the time coverage and energy efficiency can be significantly improved under non-deterministic renewable energy sources. It is worth mentioning that the concept of adaptive design has been extensively studied in many different systems [26,67,68].

Most of these systems adjust the system operation only based on the channel conditions, while our work tunes the system according to the composite effects of the channel and the renewable energy.

The rest of the chapter is organized as follows. In section 3.2, we develop a generic model of renewable energy powered signal processing systems. In section 3.3, we present the proposed energy-adaptive performance management technique. We also discuss several practical issues such as energy prediction errors and battery capacity. Simulation results are evaluated in section 3.4, and the conclusion is given in section 3.5.

3.2 System Model

We consider a generic system powered by renewable energy sources. As shown in Fig. 3.1, this system includes four major components: energy harvesting unit (EHU), energy storage unit (ESU), energy consuming unit (ECU), which performs sensing, computing and signal processing functions, and energy management unit (EMU). The EHU collects the renewable energy from the environment such as solar radiation, wind, and vibration. Usually, the available time and the amount of renewable energy are dynamically changing, while the energy consumed by the ECU can be pre-determined. To buffer the energy till the time it is utilized, the harvested energy can be stored into the ESU. Once the ECU starts to operate, it draws energy from either the ESU or the EHU.

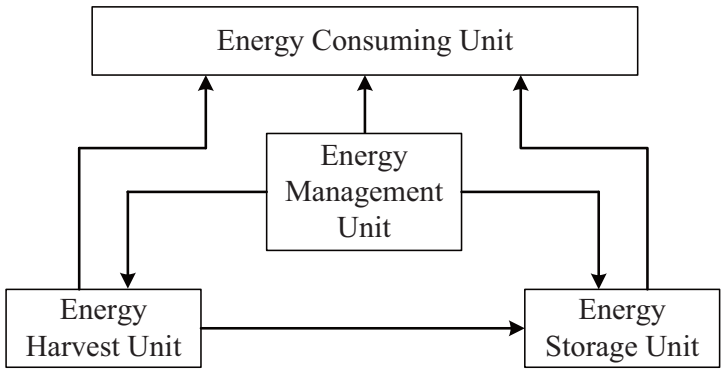

Fig. 3.1: A generic model of self-sustained embedded systems.

3.2.1 Energy harvesting unit

The EHU is characterized as a variable energy supply. For solar powered systems, the solar radiation usually varies at a relatively slow rate. Thus, it is reasonable to assume that the usable solar power P_h remains relatively stable within a short period of time; i.e., it can be approximated by a constant power level during one operation time slot (e.g., 0.5hr), even though the value may change among different time slots. As a result, the total harvested energy in the i^{th} time slot can be expressed as

$$E_h^i = P_h \times T_s, \tag{3.1}$$

where T_s is the duration of one time slot, and E_h^i represents the amount of the available energy after the energy harvester, which excludes the loss including those caused by regulating the supply voltage.

In order to adaptively allocate energy to different time slots, the profile

of the energy harvesting process is expected to be known in advance. Existing work [69] has shown that it is possible to predict the solar energy given the fact that solar radiation follows the non-deterministic yet repetitive patterns.

3.2.2 Energy storage unit

Both rechargeable batteries and super capacitors can be used as the ESU. As an energy buffer, the ESU temporarily stores the unused energy for future use when necessary. In this work, we will consider rechargeable batteries, which have a certain capacity and charging/discharging efficiency η [70]. The value of η is less than 1 due to the energy loss during charging and discharging processes. Note that η can also be used to account for the loss during energy storing and voltage regulating. In practical systems, the value of η usually changes with different workloads [70]. Since the goal of our technique is to optimize the overall performance measured by the statistical average (not instant performance boost), we use the average value of the charging/discharging efficiency, which is sufficient for the purpose of this work.

If the harvested energy E_h^i is more than what is needed, the extra energy can be saved into the rechargeable battery. The battery energy E_b^{i+1} at the beginning of $i+1^{th}$ time slot is

$$E_b^{i+1} = E_b^i + \eta(E_h^i - E_c^i), \tag{3.2}$$

where E_c^i is the amount of energy consumed in the i^{th} time slot.

On the other hand, if the harvested energy E_h^i is not enough to support the ECU in the current time slot, the rechargeable battery can supply the stored energy to the ECU. In this case, the battery energy will be reduced to

$$E_b^{i+1} = E_b^i - (E_c^i - E_h^i)/\eta. \tag{3.3}$$

3.2.3 Energy consuming unit

The ECU performs the required computation of the system and consumes most of the harvested energy. The tradeoffs between energy consumption and signal processing performance (in terms of the peak signal-to-noise ratio (PSNR), bit error rate (BER), etc.) can be exploited for design optimization. The reason is that various signal processing kernels, such as discrete cosine transform (DCT) for image processing [71] and FIR filters [61], do not contribute equally to the algorithmic performance. Consider image processing as an example. Most information of the image is concentrated in the low-frequency coefficients in the discrete cosine transform (DCT). Depending on the order of these coefficients being processed, the same rate of performance improvement actually requires different amount of energy; e.g., signal quality improvement from 70% to 80% requires 50% more energy than that from 60% to 70% [71]. Our past work [72] also demonstrated the similar trend in compressive sensing, where the last rounds of signal recovery iterations consume much more energy but can only recover less significant signal components. It is worth mentioning that in this work we use the signal quality

metric Q to quantify how much performance is reduced under different energy budgets. Because different signal processing systems may have different performance metrics, we use the normalized value in percentage for unified comparison. For example, in the DCT system, the value of Q is the ratio between the reduced PSNR (due to energy uncertainties) and the desired PSNR (under the unlimited energy).

This unique relationship between the energy consumption and algorithmic performance in signal processing systems can be generally described by a concave curve as depicted in Fig. 3.2. As shown, the system has a scalable performance from the minimal signal quality Q_0 to the maximal quality Q_{N-1}, and the associated energy consumption is E_0 and E_{N-1}, respectively. As the algorithmic performance improves from Q_0 to Q_{N-1}, the energy consumption will increase in a non-linear pattern. In other words, the same amount of the energy can enable a larger performance improvement if the system starts at a relatively low performance level. Intuitively, it takes more efforts (e.g., more energy consumption) to further improve the system performance if the performance is already high. This feature can be expressed mathematically as,

$$\frac{Q_0}{E_0} > \frac{Q_1}{E_1} > ... > \frac{Q_{N-1}}{E_{N-1}}. \tag{3.4}$$

This unique relationship will offer new opportunities to the design of signal processing systems powered by renewable energy, as discussed in Section 3.3.

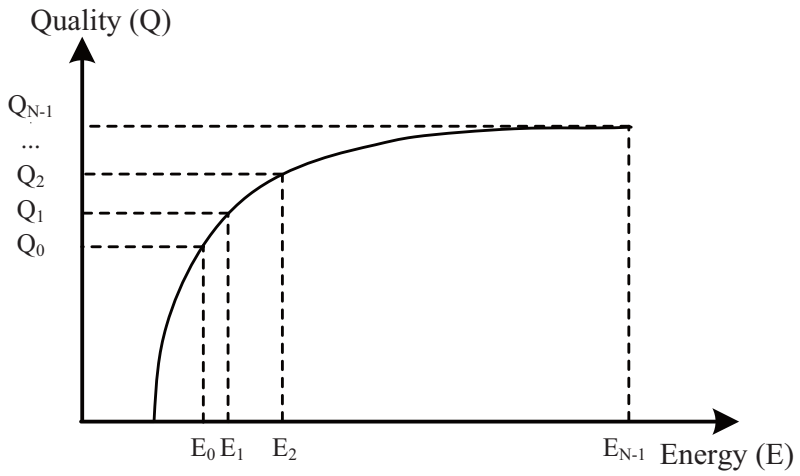

Fig. 3.2: Energy consumption vs signal quality in a typical signal processing system.

3.2.4 Energy management unit

The EMU collects the runtime information of the system, such as the renewable energy level, the battery status, and the workload requirement. Based on these information, a decision is made to allocate a suitable amount of the energy to the ECU. In the next section, we will present an energy-adaptive performance management technique to optimize the tradeoffs of performance and energy efficiency under non-deterministic renewable energy. Note that the proposed technique is different from conventional low-power/energy-efficient techniques that typically target the stable (though maybe limited) energy supply.

Table 3.1: Energy and image quality (measured by the peak SNR, i.e., PSNR) in DCT, both normalized by the maximum values.

Energy	1.00	0.65	0.43	0.28	0.18
Quality	100%	90%	80%	70%	60%

3.3 Energy-adaptive Performance Management

In this section, we discuss the proposed energy-adaptive performance management technique for signal processing systems powered by renewable energy. Considering the fact that renewable energy sources are typically non-deterministic, the proposed technique dynamically adjusts the achievable signal quality to match with the changing energy level.

3.3.1 Motivation

We consider a DCT-based image sensing and transmission system powered by renewable energy (e.g., solar) for outdoor unattended monitoring. Existing work [71] studied the relationship between signal quality and energy consumption of the DCT. As shown in Table 1, reducing the number of coefficients in DCT will incur a performance loss but at the same time enables energy savings.

Assume that in two consecutive time slots t_i and t_{i+1}, the normalized harvested energy is 0.5 and 0.3, respectively, and the normalized battery energy at the beginning of the t_i slot is 0.3. A conventional design targeting the full signal

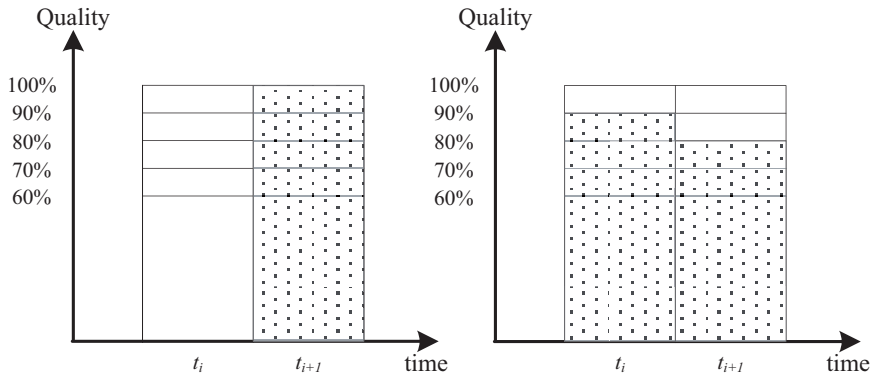

(a) (b)

Fig. 3.3: Performance comparison between (a) the conventional system and (b) the proposed system without the battery effect.

quality cannot process the DCT signal in the t_i slot, as the available energy is less than what is needed, i.e., $0.5 + 0.3 < 1.0$ (see Table 1). The harvested energy is thus stored in the battery for the next slot. Consequently, the system can only process the DCT signal in the t_{i+1} slot, as $0.5 + 0.3 + 0.3 > 1.0$. This scenario is illustrated in Fig. 3.3(a). In contrast, if the system can dynamically adjust the signal quality in accordance with the changing energy level, a better performance can be achieved. As depicted in Fig. 3.3(b), the DCT signal can be processed at 90% quality (as the available energy $0.5 + 0.3 > 0.65$, see Table 1) and 80% quality ($0.5+0.3+0.3-0.65 > 0.43$) in these two slots. This results in an average of 85% signal quality, much higher than the average 50% signal quality in the conventional system.

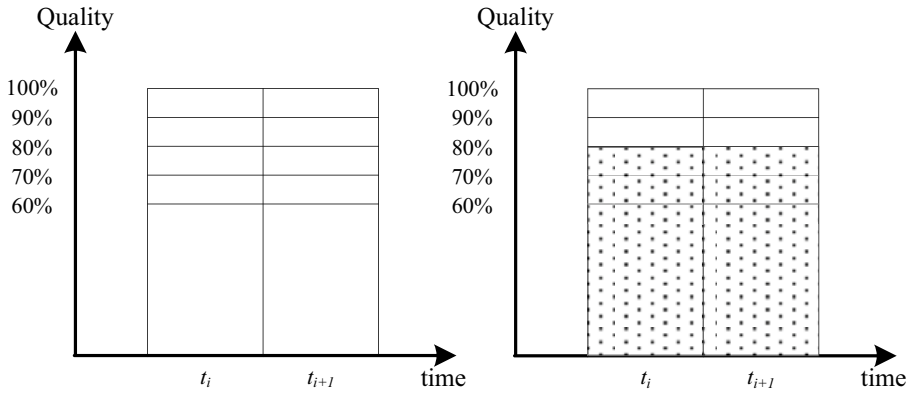

(a) (b)

Fig. 3.4: Performance comparison between (a) the conventional system and (b) the proposed system with the battery effect.

Note that the above example does not consider the battery charging/discharging efficiency. When this practical issue is taken into account, the proposed energy-adaptive performance management technique can achieve even better performance than the conventional system. Assume that the average battery charging/discharging efficiency η is 0.9. The conventional system cannot process the DCT signal in either the t_i slot or the t_{i+1} slot. This is because the battery can only store $0.5 \times 0.9 = 0.45$ harvested energy after the t_i slot. Thus, the available energy at the beginning of the t_{i+1} slot is just $(0.3+0.45)\times 0.9+0.3 = 0.975 < 1.0$, of which $(0.3 + 0.45) \times 0.9 = 0.675$ comes from the battery. On the other hand, the system employing the energy-adaptive performance management can achieve an average of 80% signal quality in the presence of energy loss due to battery

charging/discharging. These results are presented in Fig. 3.4 for comparison.

3.3.2 The proposed technique

Considering the fact that renewable energy is typically non-deterministic, the limited (and unstable) energy must be allocated dynamically among multiple operation time slots to enable the optimal performance over time. The proposed energy-adaptive performance management technique exploits the unique relationship between the performance and energy consumption in signal processing systems as depicted in Fig. 3.2 to achieve this goal. The basic idea is to resort to a progressive energy allocation approach while considering the performance impact among multiple time slots.

For the sake of simplicity, we will initially discuss the proposed technique for two consecutive operation time slots, denoted as the current slot i and the next slot $i + 1$. The harvested energy can be measured for the current slot and predicted for the next slot with a high accuracy [69]. The proposed technique can also be generalized to more time slots if the harvested energy in these slots can be predicted, which is usually possible. Note that most energy prediction algorithms strive to reduce the prediction errors statistically. This error effect will be studied in the performance analysis in Section 3.4.

Energy allocation among adjacent time slots

From Fig. 3.2, it is obvious that the limited amount of energy can be more effectively utilized to improve the system performance when the signal quality is low. Thus, our technique starts with the lowest acceptable signal quality. This procedure is shown as the step P_0 in Fig. 3.5. The required energy to achieve the baseline performance (e.g., signal quality Q_0^i) at the t_i slot is denoted as E_0^i. At the beginning of the t_i slot, if the harvested energy E_h^i is larger than E_0^i, then no matter how much the harvested energy E_h^{i+1} at the t_{i+1} slot is, the signal quality Q_0^i can always be achieved. Under this condition, the extra energy in the t_i slot will be stored in the battery for the t_{i+1} slot. Thus, the battery energy E_b^{i+1} at the beginning of the t_{i+1} slot can be expressed as

$$E_b^{i+1} = E_b^i + \eta(E_h^i - E_0^i), \tag{3.5}$$

where $\eta \leq 1$ is the battery charging/discharging efficiency. Note that the underlying assumption of (3.5) is that the battery capacity is sufficiently large, therefore no battery overflow occurs. This assumption will be relaxed in Section 3.3.4

On the other hand, if E_h^i is less than E_0^i while $E_h^i + \eta E_b^i$ is larger than E_0^i, the ECU can draw some energy from the battery to obtain the signal quality Q_0^i. In this case, the battery energy E_b^{i+1} at the beginning of the t_{i+1} slot becomes

$$E_b^{i+1} = E_b^i - (E_0^i - E_h^i)/\eta. \tag{3.6}$$

Under the extreme case when the total available energy at the beginning of

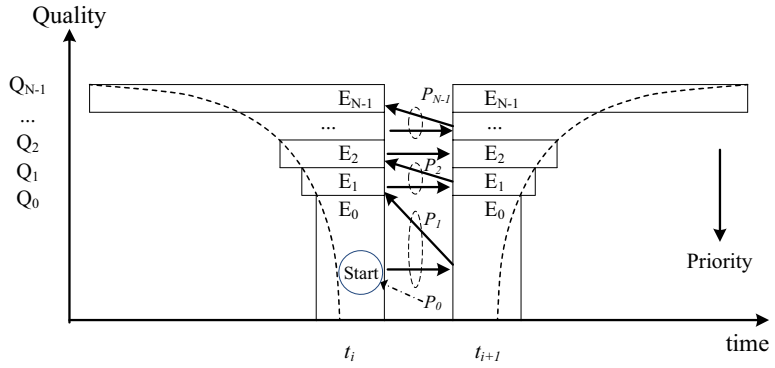

Fig. 3.5: Progressive performance tuning (the length of energy bars in horizontal indicates the amount of energy needed to achieve the image quality Q_i).

the t_i slot cannot support even the baseline performance (e.g., smaller than E_0^i), the system can either be shut down or operate below the minimal performance requirement to accommodate the available energy. The latter is usually preferable because otherwise the harvested energy will be lost. Note that the minimal performance denoted by Q_0 is pre-specified by the user based on the requirement of the application.

The second phase of the proposed technique is shown as the step P_1 in Fig. 3.5, where we will evaluate whether a higher performance level can be achieved at the t_i slot under a certain energy condition. Consider the unique relationship between the performance and energy consumption as depicted in Fig. 3.2, we should concurrently check if Q_0^{i+1} can be achievable at the next t_{i+1} slot as it requires the smallest amount of energy; in other words, it enables the best overall

energy-performance tradeoffs across the two time slots. There are four possible scenarios as described blow.

Scenario 1: When the harvested energy E_h^{i+1} is already more than the baseline performance required energy E_0^{i+1}, there is no need to transfer the harvested energy from the t_i slot to the t_{i+1} slot. It only needs to check the following condition to see if the available energy in the t_i slot is sufficient for the next performance level Q_1^i,

$$E_h^i + \eta E_b^i > E_1^i. \tag{3.7}$$

If the inequality holds, Q_1^i will be selected; otherwise, Q_0^i is selected due to the lack of energy to support Q_1^i in the t_i slot.

Scenario 2: When the harvested energy E_h^{i+1} is less than the baseline performance required energy E_0^{i+1}, we can supplement $E_0^{i+1} - E_h^{i+1}$ from the battery if the battery energy is sufficient. There is still a chance to select Q_1^i in the t_i slot and Q_0^{i+1} in the t_{i+1} slot, if the following condition is satisfied,

$$E_h^i + \eta[E_b^i - (E_0^{i+1} - E_h^{i+1})/\eta] > E_1^i, \tag{3.8}$$

where $(E_0^{i+1} - E_h^{i+1})/\eta$ is the amount of battery energy that will be allocated to the t_{i+1} slot for the baseline performance. Clearly, when the total harvested energy E_h^i and the residual battery energy $E_b^i - (E_0^{i+1} - E_h^{i+1})/\eta$ is more than the required energy E_1^i, the higher signal quality Q_1^i can be achieved.

Scenario 3: The harvested energy E_h^{i+1} is less than the baseline performance required energy E_0^{i+1}, and the deficient $E_0^{i+1} - E_h^{i+1}$ cannot be provided by the

battery. To achieve Q_0^{i+1}, a portion of the harvested energy E_h^i in the t_i slot will be stored in the battery to fill the energy gap in the t_{i+1} slot. Thus, the following condition will make Q_1^i achievable,

$$E_h^i - [(E_0^{i+1} - E_h^{i+1})/\eta - E_b^i]/\eta > E_1^i, \tag{3.9}$$

where $[(E_0^{i+1} - E_h^{i+1})/\eta - E_b^i]/\eta$ is the amount of energy that needs be stored in the battery for use in the t_{i+1} slot to achieve Q_0^{i+1}. If the remaining energy is still more than the required energy E_1^i, the higher signal quality Q_1^i can be achieved.

Scenario 4: In the worst case when the total available energy at the beginning of the t_{i+1} slot cannot support the baseline performance Q_0^{i+1}, i.e.,

$$E_h^{i+1} + \eta E_b^{i+1} < E_0^{i+1}, \tag{3.10}$$

then there is no need to check the higher quality Q_1^i at the t_i slot. This is because if E_b^{i+1} obtained from (3.5) or (3.6) based on the t_i slot cannot support Q_0^{i+1}, it cannot support Q_1^i either due to the higher energy requirement of Q_1^i. This is also reflected in Fig 3.5, in which the system will try to improve Q_0^i to Q_1^i only when both baselines Q_0^i and Q_0^{i+1} are achievable under the unstable energy.

Proceeding in the same way, the progressive performance tuning will evaluate whether higher performance levels can be achieved in adjacent time slots under the given energy condition. This is represented by steps P_2 to P_{N-1} in Fig. 3.5. Then, the same procedure will be performed dynamically over other time slots. This is summarized in Algorithm 2.

Extension to multiple time slots

We now extend the proposed technique to multiple time slots, which may occupy an entire day as solar radiation varies on a daily basis. The harvested energy in these slots can be predicted, as shown in many previous work [73].

As mentioned before, the baseline signal quality requires the smallest amount of energy to achieve. For this consideration, it is necessary to initially check whether the system can work at E_0^i for all the time slots t_0 to t_{N-1} before going for higher signal qualities, i.e.,

$$E_b^i + E_h^i > E_0^i, \tag{3.11}$$

where i ranges from 0 to $N-1$, and E_b^i is determined by (3.5) or (3.6) depending on the harvested energy level at the t_{i-1} time slot.

It is expected that the system should be able to operate at the minimal required signal quality level Q_0 for most cases. Under the extreme condition such as very bad weather for quite a long time, the system may not be able to receive sufficient energy to work at Q_0. As illustrated in Fig. 3.6, if the system can only support Q_0 from t_0 to t_{L-1} but not the t_L time slot, then there is no need to further check the signal quality Q_1 between t_0 and t_L due to the energy shortage, and Q_0^i, $i = 0...L-1$, is the final performance level in these slots. This is the same as that in (3.10) for two adjacent time slots.

As the energy harvested after t_L could become abundant, we still need to

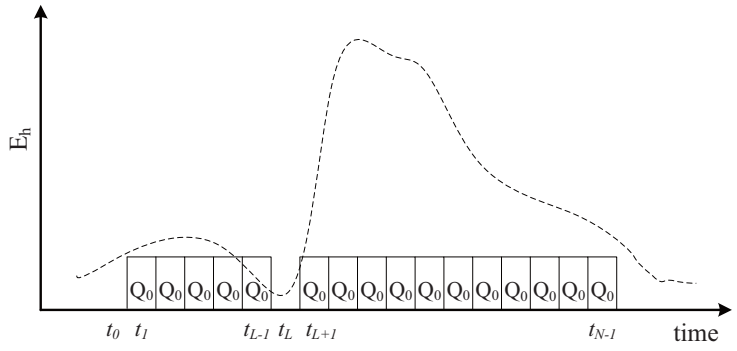

Fig. 3.6: Illustration of quality Q_0 allocation (the height of energy bars indicates the amount of energy needed to achieve the corresponding image quality).

adjust the system performance from t_L to t_{N-1}. Without loss of generality, we assume t_L, i.e., the earliest time slot when the system can possibly have the performance higher than Q_0, is the initial time slot t_0. Three possible scenarios may occur when determining whether the higher performance Q_1 is achievable.

Scenario 1: When the harvested energy is sufficient for most of the time slots and the time slots with inadequate energy can use the stored energy from the previous time slots, all the time slots can achieve Q_1 if

$$E_h^i + \eta E_b^i > E_1^i, \tag{3.12}$$

where E_b^i is determined by

$$E_b^i = E_b^{i-1} + \eta(E_h^{i-1} - E_1^{i-1})^+ - (E_1^{i-1} - E_h^{i-1})^+/\eta, \tag{3.13}$$

where the function $(x)^+$ equals x if $x > 0$ and otherwise equals 0. This scenario

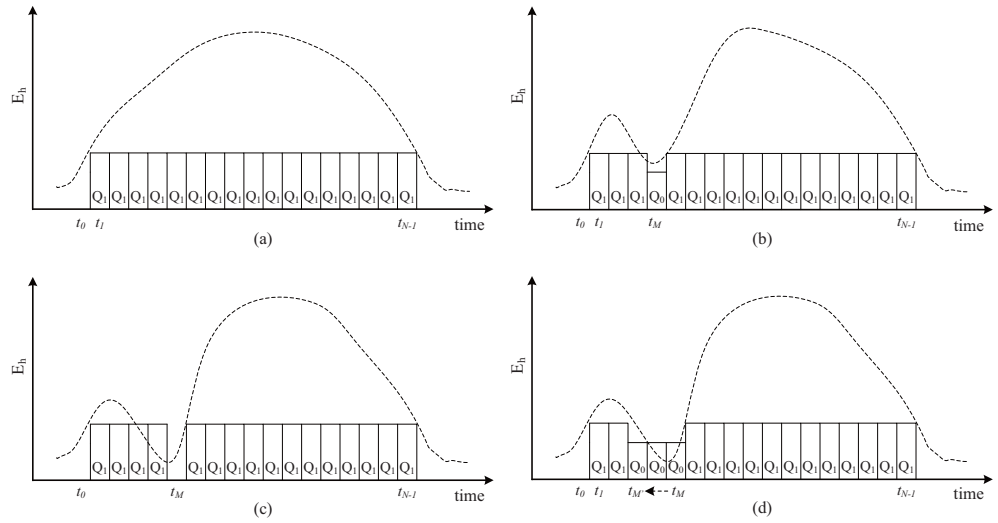

Fig. 3.7: Illustration of three possible scenarios in multiple time slots energy allocation (the height of energy bars indicates the amount of energy needed to achieve the corresponding image quality).

is illustrated in Fig. 3.7(a).

Scenario 2: When the harvested energy is enough to support Q_0 but not Q_1 at a certain time slot t_M, i.e.,

$$E_h^M + \eta E_b^M < E_1^M, \tag{3.14}$$

then the energy allocation from t_0 to t_M is finished because all the available energy will be consumed in these time slots. The final performance level from t_0 to t_{M-1} is Q_1, and the performance level at t_M is Q_0, as shown in Fig. 3.7(b). Now the system will need to determine the energy allocation policy for the time slots after t_M, starting with Q_1.

Scenario 3: This scenario is similar to scenario 2 except that the harvested energy is not even enough to support Q_0 at a certain time slot t_M, i.e.,

$$E_h^M + \eta E_b^M < E_0^M. \tag{3.15}$$

This indicates that achieving Q_1 in the previous time slots causes energy deficiency and Q_0 is unattainable at t_M (see Fig. 3.7(c)). Under this situation, the previous performance levels starting from t_{M-1} need to be lowered for more energy savings, until at a time slot $t_{M'}$ $(0 \leq M' \leq M-1)$ where the saved energy can support Q_0 at t_M. This process is illustrated in Fig. 3.7(d). Once M' is determined, the final performance levels from t_0 to t_M can be determined as well, which are Q_1 for t_0 to $t_{M'-1}$ and Q_0 for $t_{M'}$ to t_M. The performance for time slots after t_M will then need to be determined thereafter, starting with Q_1.

This process will continue for higher signal qualities until all the harvested energy is allocated and the overall system performance is maximized. The complete algorithm is summarized in Algorithm 3.

3.3.3 Reducing the impact of energy prediction errors

The energy-adaptive performance management assumes accurate energy prediction in each time slot. In reality, energy prediction will always introduce errors [73], which will affect the effectiveness of the proposed technique. Thus, it is important to compensate for the energy prediction errors, defined as

$$\Delta(i) = E_h^{real}(i) - E_h^{pre}(i) + \eta \times E_h^{res}(i-1), \tag{3.16}$$

where $E_h^{real}(i)$ is the measured harvested energy, $E_h^{pre}(i)$ is the predicted energy, and $E_h^{res}(i-1)$ is the residual battery energy from the previous time slot. Note that initially $E_h^{res}(i-1) = 0$, and in the subsequent time slots $E_h^{res}(i-1)$ represents the portion of the harvested energy that is not consumed.

Starting with a set of performance levels determined by the predicated energy as shown in the previous sections, the system will need to adjust the performance at runtime to mitigate the effect of energy prediction errors. When $\Delta(i) < 0$, the system can reduce the signal quality at the t_i time slot to fill the energy gap. If the signal quality is already at the baseline, the system may need to reduce the signal quality further to below the minimal performance requirement, if the time coverage requirement is more important. Reducing the signal quality at future time slots will not help as the energy cannot be transferred from future time slots to the current time slot. On the other hand, when $\Delta(i) > 0$, i.e., the system receives more energy than predicted, the extra energy should be assigned to time slots with the lowest signal quality, as this is the most effective way to improve energy efficiency for signal processing systems according to Fig. 3.2.

3.3.4 Limitations of battery capacity

Rechargeable batteries play a key role in renewable energy powered systems, as they act as energy buffers to store the harvested energy for future use. However, battery capacity must be considered in the practical system design. Obviously,

a battery cannot store the energy beyond its capacity. When battery overflow occurs, the extra energy is wasted. In the proposed technique, this extra energy can be utilized to further increase the performance level.

When the expected battery energy E_b^{i+1} in (3.5) is larger than the battery capacity E_{max}^b, the battery can only be charged to E_{max}^b, i.e.,

$$E_b^{i+1} = E_{max}^b. \tag{3.17}$$

Thus, the system should try to consume $E_h^i - (E_{max}^b - E_b^i)/\eta$ in the t_i slot to reduce the energy waste, where $(E_{max}^b - E_b^i)/\eta$ is the maximum energy that can be stored in the battery.

Another issue is that, when the battery capacity is small, the available energy (e.g., harvested and stored energy in the battery) may not be able to support even the minimal signal quality at certain time slots. In this case, the system can either be shut down or operate below the minimal performance requirement at the current time slot to accommodate the available energy. As expected, the average performance over multiple time slots will be reduced if the battery capacity is smaller. Nevertheless, the proposed algorithm is less sensitive to the battery capacity limitation as compared with the conventional method (see results in Section 3.4). This is because our technique can adaptively adjust the energy consumption to make these battery issues less likely to occur.

3.4 Simulation Results

In this section, we apply the proposed energy-adaptive performance management technique in a DCT-based image sensing system powered by solar energy. We will compare with a conventional system and demonstrate the performance improvement.

3.4.1 Simulation setup

We adopt the solar radiation profile collected by the National Renewable Energy Lab [74], and conduct simulations based on the solar profile of 30 consecutive days. Figure 3.8 shows four days with different solar profiles, where the energy harvesting time is from 7am to 6pm. The DCT-based image sensing system is assumed to operate during this period. The length of each time slot is set as 0.5 hour. The solar energy is converted by the solar panel of 10cm×10cm with the efficiency of 20%. The energy prediction algorithms employed are Exponentially Weighted Moving Average (EWMA) [75,17] for two time slots and Weather-Conditioned Moving Average (WCMA) [69] for multiple time slots. The reason is that WCMA, while has a better accuracy (4% prediction errors) than EWMA (33% prediction errors), cannot be used for multi-slot prediction. All the simulation results have included these prediction errors. The rechargeable battery has an average efficiency of 0.9, and the battery capacity E_b^{max} is equal to the average harvested energy of one day. The battery energy is monitored at the beginning

of each time slot [39]. Note that the proposed technique does not depend on the specific value of the battery capacity. This is because the battery is mainly used as a buffer to temporarily store the harvested energy. In reality, the harvested energy varies due to many uncontrollable factors. Thus, most likely the battery will not be fully charged and cannot support the required signal processing tasks. The proposed technique dynamically adjusts the algorithm configuration at runtime to deal with the non-deterministic renewable energy.

The DCT-based image sensing system is shown in Fig. 3.9. A standard transmitter design [30] is employed and the associated configuration parameters are adopted, which include the modulation, analog conversion, and RF transmission. Note that RF transmission energy is usually dominant. This problem has been studied in our past work [1,2], where an energy-adaptive RF modulation technique was developed to better utilize the renewable energy. As this work focuses primarily on the baseband signal processing, the results of RF energy are not included in the comparison. The quality-adjustable DCT accelerator [71] can process image data with different levels of quality for energy-performance tradeoffs. The hardware support to the quality adjustments involves computing a subset of the DCT coefficients. For example, by computing just 12 coefficients rather the whole 64 coefficients, the signal quality can be adjusted to 60% of the best quality. Note that we do not change the supply voltage to adjust the signal processing quality. It was done by changing the algorithm complexity/configuration.

The image (640 × 480 pixels) is first partitioned into 8 × 8 blocks, each encoded with the DCT accelerator. The first 12, 18, 28, 42, and 64 coefficients with 12 bits per coefficient of the DCT results carry about 60%, 70%, 80%, 90%, and 100% information of the image, respectively. By calculating and transmitting only the first N_{DCT} coefficients, the receiver can decode and reconstruct the image at the corresponding quality. The upper limit of the acceptable image quality is assumed to be 100% (measured by the normalized PSNR), and the lower limit varies between 60% and 100% (normalized PSNR). Since the proposed technique can adjust the energy consumption of the DCT accelerator and the transmitter (but not the image sensor) by reducing the number of DCT coefficients being processed and transmitted, we simulated these two components in a 90nm CMOS process and found that the total average energy consumption is about 10μJ/bit under the QPSK modulation. A standard image sensor [11] consumes a much smaller energy of about 1μJ/frame. The workload in one time slot of 0.5 hour is defined by the number of frames N_f being processed and transmitted. In our simulation setup, $N_f = 40$ frames per time slot is selected to demonstrate the effectiveness of the proposed method. Note that the proposed technique is not limited by the frame rate of the DCTs. The proposed technique requires only simple operations (additions, subtractions, comparisons, and look-up table searching) for progressive performance tuning. Due to the small number of image quality levels (5 levels in our simulation) in the search space, the complexity of the proposed

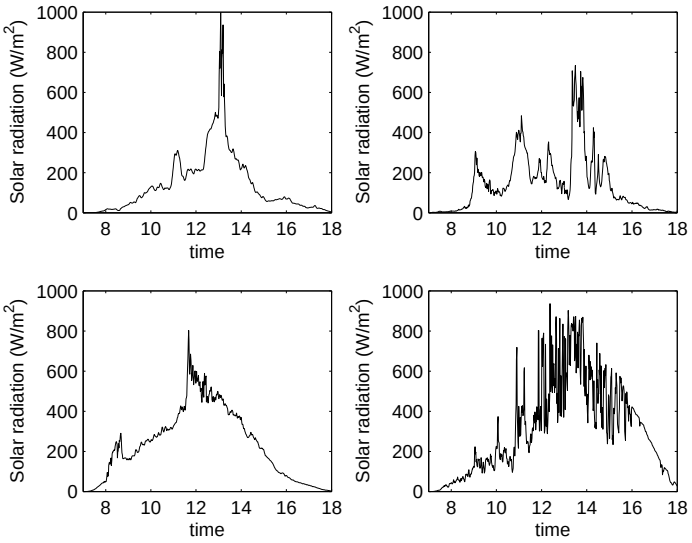

Fig. 3.8: Solar profiles of four days.

technique is very small. Nevertheless, the induced energy overhead was estimated and included in the simulation results.

3.4.2 Performance analysis and discussion

We will show the results of two different schemes, one considering two adjacent time slots and the other considering multiple time slots. We will demonstrate that the multi-slot energy allocation scheme outperforms the two-slot energy allocation scheme under various workload conditions. These two schemes will also be compared with the conventional system for performance and energy efficiency.

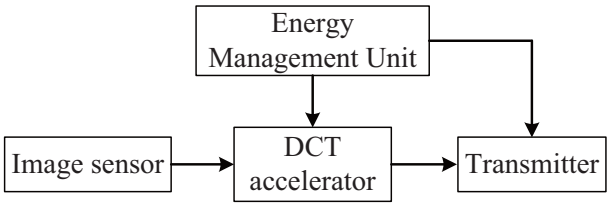

Fig. 3.9: Block diagram of the DCT-based image sensing system.

Performance comparisons

We compare the two schemes with the conventional design targeting full-quality DCT encoding and transmission under the same solar energy profile. All systems are designed to achieve a pre-defined PSNR of 36dB under the full image quality. To deal with energy supply fluctuations, the conventional system can adjust the number of frames N_f to accommodate energy shortage. At the beginning of each time slot, the conventional system will determine if the harvested energy is sufficient for the required workload. If not, the system will reduce the number of frames; otherwise, the extra energy, if any, will be saved for future use. This is different from the proposed technique that aims to accomplish the required N_f for tradeoffs with the image quality. In image sensing systems, the average time coverage T_{cov} is related to the number of frames processed in each time slot, which is defined as

$$T_{cov} = \frac{T_f}{N_f N_T}, \tag{3.18}$$

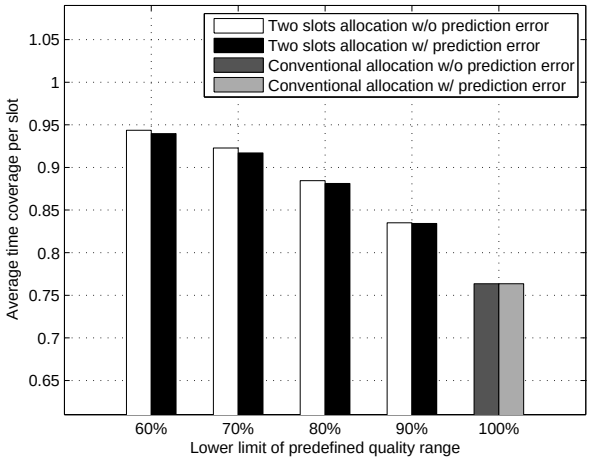

Fig. 3.10: Average time coverage of the two-slot energy allocation scheme under the renewable energy.

where T_f is the total number of frames that the system can process under the renewable energy and N_T is the total number of time slots. Note that image sensing systems typically require a high time coverage while the image quality is compromisable for applications such as monitoring and surveillance. This is the reason that the proposed technique trades off image quality for time coverage under the variable harvested energy.

Figure 3.10 compares the average time coverage achieved by the two-slot energy allocation scheme and the conventional system. For the conventional system targeting 100% signal quality, the average time coverage is only about 76% (i.e., about 30 out of 40 frames can be processed on average due to the unstable renewable energy). In comparison, the proposed scheme achieves a much higher time

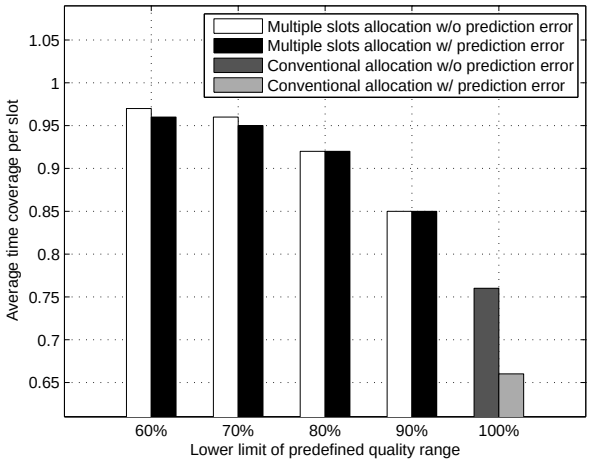

Fig. 3.11: Average time coverage of the multi-slot energy allocation scheme under the renewable energy.

coverage when the image quality is dynamically adjusted to compensate for the unstable renewable energy. This is because by dynamically adjusting the image quality, the proposed technique can maintain a relatively stable image processing capability in realtime even when the energy is insufficient and varying. Trading off image quality for time coverage is typically preferable in renewable energy powered image sensing systems targeting monitoring and surveillance applications. In Figure 3.10, due to the high accuracy of WCMA, the time coverage loss caused by energy prediction errors is negligible (less than 1%). The similar comparison between the multi-slot energy allocation scheme and the conventional system is shown in Fig. 3.11. Multi-slot energy allocation scheme can achieve even better time coverage than the two-slot scheme in Fig. 3.10. However, the time cover-

age loss due to energy prediction errors is relatively large. Fortunately, by using the method discussed in Section 3.3.3, the impact of energy prediction errors can be minimized. In comparison, the conventional system experiences much larger time coverage degradation as it only adjusts the number of frames per slot, which directly affects the time coverage.

Energy efficiency

To quantify the energy efficiency, we compare the average image quality normalized by the available renewable energy as,

$$E_Q = \frac{\sum_{i=1}^{T_f} Q_j^i}{\sum_{i=1}^{N_T} E_h^i}, \tag{3.19}$$

where $\sum_{i=1}^{T_f} Q_j^i$ is the sum of the image qualities in PSNR of the processed frames T_f, and $\sum_{i=1}^{N_T} E_h^i$ is the harvested energy in these time slots.

As shown in Fig. 3.12, with image quality being tuned down from 90% to 60%, the difference in E_Q between the two-slot energy allocation scheme and the conventional system increases, indicating $7\% - 14\%$ (or equivalently 1.5dB/J–3dB/J) improvement in energy efficiency. In other words, more information can be processed by the proposed technique under the same amount of renewable energy. Similar trend was also observed in the multi-slot energy allocation system, as shown in Fig. 3.13, which indicates about $9\% - 17\%$ (or equivalently 1.9dB/J–3.5dB/J) energy efficiency improvement. This can be explained by the fact that our technique exploits the non-linear relationship between the image quality and

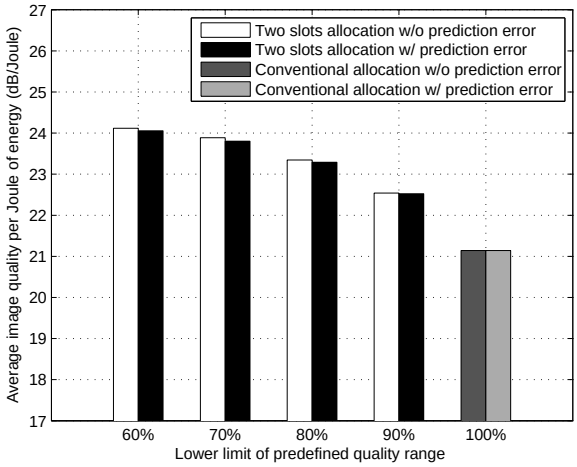

Fig. 3.12: Average image quality per Joule of the two-slot energy allocation scheme under the renewable energy.

energy consumption (see Fig. 3.2), and consumes energy more efficiently to process significant signal components when necessary; whereas the conventional system treats signal components equally and thus wastes the energy. Clearly, the proposed technique is beneficial to image sensing systems powered by renewable energy sources. Note that the multi-slot energy allocation scheme again achieves the better performance overall than the two-slot energy allocation scheme. Also, these results consider the effect of energy prediction errors.

3.5 Conclusions

In this chapter, we have developed an energy-adaptive performance management technique for self-sustained signal processing systems. Considering the fact that

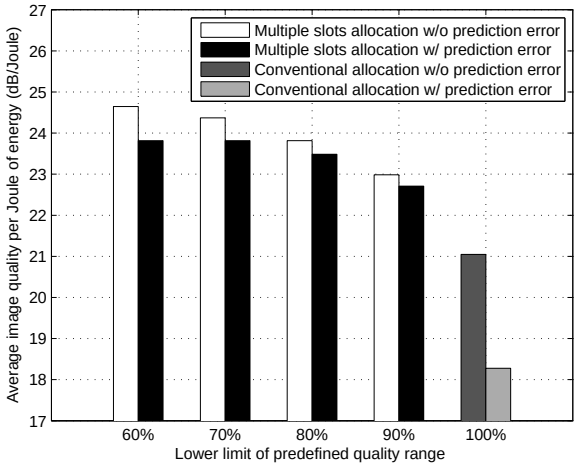

Fig. 3.13: Average image quality per Joule of the multi-slot energy allocation scheme under the renewable energy.

renewable energy sources are typically non-deterministic, the proposed technique dynamically matches the achievable signal quality with the changing energy level to optimize the energy and performance tradeoffs. The unique relationship between signal processing performance and the required energy consumption inherent in most signal processing systems is exploited to achieve this goal. Future work is directed towards hardware demonstration of the proposed technique, applying the proposed technique in real signal processing systems, and comparing the tradeoff in performance and energy efficiency with other low-power design techniques such as DVFS.

Algorithm 2: Summary of the two-slot energy allocation scheme.

Input:
i (Index of time slot, range between 0 and $N_T - 1$)
E_h^i (Harvested energy at the i^{th} time slot)
E_b^i (Battery energy at the i^{th} time slot)
η (Battery charging/discharging efficiency)
j (Index of signal quality, range between 0 and $N - 1$)
Q_j^i (The j^{th} quality at the i^{th} time slot)
E_j^i (Energy associated with the Q_j^i at the i^{th} time slot)
N_f (The number of frames to be processed per time slot)
Output: Energy allocation at i^{th} time slot

```
1  begin
2      for i ← 0 to N_T − 1 do
3          Check if Q_0^i is achievable. E_b^{i+1} is determined by eqns(5,6)
4          for j ← 1 to N − 1 do
5              if E_h^{i+1} + ηE_b^{i+1} < E_{j−1}^{i+1} then
6                  return E_{j−1}^i. See scenario 4
7              else if E_h^{i+1} > E_{j−1}^{i+1} then
8                  if E_h^i + ηE_b^i > E_j^i then
9                      Q_j^i is achievable. See scenario 1
10                 else return E_{j−1}^i. See scenario 1
11
12             else if E_h^{i+1} + ηE_b^{i+1} > E_{j−1}^{i+1} then
13                 if E_h^i + η[E_b^i − (E_{j−1}^{i+1} − E_h^{i+1})/η] > E_j^i then
14                     Q_j^i is achievable. See scenario 2
15                 else return E_{j−1}^i. See scenario 2
16
17             else if η²E_h^i + ηE_b^{i+1} + E_h^{i+1} > E_{j−1}^{i+1} then
18                 if E_h^i − [(E_{j−1}^{i+1} − E_h^{i+1})/η − E_b^i]/η > E_j^i then
19                     Q_j^i is achievable. See scenario 3
20                 else return E_{j−1}^i. See scenario 3
21
22         end
23     end
24 end
```

Algorithm 3: Summary of the multi-slot energy allocation scheme.

Input:
i (Index of time slot, range between 0 and $N_T - 1$ in one day)
E_h^i (Harvested energy at the i^{th} time slot)
E_b^i (Battery energy at the i^{th} time slot)
η (Battery charging/discharging efficiency)
j (Index of signal quality, range between 0 and $N - 1$)
Q_j^i (The j^{th} quality at the i^{th} time slot)
SP_j (Starting point for the Q_j checking process)
E_j^i (Energy associated with the Q_j^i at the i^{th} time slot)
Output: Energy allocation of N_T time slots

```
1  begin
2      for i ← 0 to N_T − 1 do
3          Check if Q_0^i is achievable for all N_T.
4          if All slots can achieve Q_0^i then
5              Set SP_1 = 0; j = 1.
6          else if Q_0^L is not achievable then
7              Set SP_1 = L + 1; j = 1. See Fig. 3.6
8      end
9      for i ← SP_j to N_T − 1 do
10         for j ← 1 to N − 1 do
11             if Q_j^i is achievable between SP_j and N_T − 1 then
12                 Set SP_{j+1} = SP_j. See Fig. 3.7(a).
13             else if Q_j^M is not achievable then
14                 if Q_{j−1}^M is also achievable then
15                     Set SP_{j+1} = M + 1. See Fig. 3.7(b).
16                 else Set SP_{j+1} = M + 1;  Trigger the restoring back
                   process. See Fig. 3.7(c-d).
17
18         end
19     end
20 end
```

Chapter 4

Self-sustained UWB Sensing: A Link and Energy Adaptive Approach

In this chapter, we present a link and energy adaptive UWB-based sensing technique to improve the detection time coverage and detection range coverage for self-sustained embedded applications. The basic idea is derived from the fact that domain-specific information in such applications is often available. Thus, by jointly exploiting the link information between the transmitter and receiver of the UWB pulse radar, and the non-deterministic characteristics of the renewable energy, the proposed technique dynamically adjusts the pulse repetition frequency of the UWB radar to enhance the sustainable operation under the unreliable energy supply. The overhead of the proposed technique is negligible as compared with the overall energy consumption of the UWB pulse radar. It was demonstrated that the proposed technique can achieve much better detection time coverage and detection range coverage than the conventional UWB radar. The proposed technique is also insensitive to many practical issues such as the limited battery

capacity.

4.1 Introduction

Ultra-wideband (UWB) radar has become a promising technology for short-range sensing [76], detection [77], and wireless communications [78,48]. The unique properties of narrow UWB pulses allow accurate measuring and offer robust signaling against the multi-path fading in wireless channels. The pulsed UWB signal inherently has a low duty cycle, which naturally enables low-power operations. Furthermore, UWB features low-complexity transceiver structure and unlicensed communications by FCC regulations [79], all of which make it a good candidate for embedded applications.

Due to these advantages, UWB technique have been widely adopted in many emerging applications, including positioning [80], object recognition [81], and wireless body area network (WBAN) [82]. In [83], a low-complexity and low-power UWB transceiver is proposed for health monitoring in WBAN. In [84], a UWB pulse radar IC is developed to track and range the target for respiratory rate monitoring. In outdoor environments, UWB-based radar can be used for short-range and high time resolution applications, such as tracking and ranging in agriculture environments [85], or used as the vehicle radar [86]. It should be noted that most of the existing work assume the operation of UWB radar under stable and sufficient power supply.

Among the above mentioned applications, low-power embedded sensing is a new area where the benefits of UWB pulse radar can be effectively reaped. However, a critical issue in embedded sensing is the lack of sustainable power supply. While most of embedded systems can be powered by batteries, frequent recharge and maintenance is costly if not impossible. For this reason, exploiting renewable natural resources (e.g., solar radiation, wind, ocean wave, etc.) to power autonomous and distributed sensor devices has become a promising alternative [4,35,1,49,3]. It was reported in recent literature [87] that solar cells can harvest solar energy up to the power density of 15mW/cm^2, and the latest energy harvesting circuit can convert the power output of photovoltaic (PV) panels with an efficiency around 93%. The improved efficiency and cost reduction in energy harvesting techniques have spurred significant interests in deploying self-sustained embedded systems [11,12,2]. However, different from the battery-powered systems [54,88,89,7], most renewable energy sources are non-deterministic with large variations that characterize the energy harvesting process. This requires a new approach to the design of self-sustained embedded sensing systems, where stable and robust performance needs to be maintained through the synergy of energy characteristics and sensing operations.

In this chapter, we develop a link and energy adaptive UWB-based embedded sensing technique powered by renewable energy sources such as solar radiation. Distinct from the existing UWB sensing techniques, the proposed technique

deliberately exploits the varying link gains and non-deterministic energy characteristics in a coherent manner to improve the sensing performance and coverage. Specifically, the proposed technique dynamically adjusts the UWB pulse repetition frequency in accordance with the available renewable energy level as well as the wireless link condition. It is shown that by making the UWB transceiver link and energy adaptive, better detection time coverage and performance trade-offs can be achieved. The fact that the energy overhead imposed by the proposed technique is minor makes our technique well-suited to resource/energy constrained sensing applications. We also consider some practical issues such as the capacity of rechargeable batteries. Simulation results demonstrate the advantages of the proposed technique over conventional UWB sensing techniques. Note that the link information has been extensively utilized for different system design goals, such as low power design [90] and enhanced security design [91,92]. While most of these systems are adjusted according to the channel conditions only, our work tunes the system based on the composite effects of the channel and the harvested energy.

The rest of this chapter is organized as follows. In Section 4.2, we describe the model of self-sustained UWB pulse radar for sensing applications. We also discuss the limitations of conventional UWB sensing techniques when powered by renewable energy sources. In Section 4.3, we develop the link and energy adaptive UWB sensing technique, derive an analytical approach to explore the

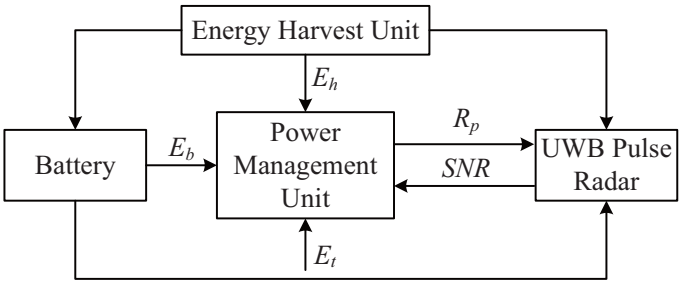

Fig. 4.1: Model of a self-sustained UWB-based sensing transceiver.

interplay between energy characteristics and sensing performance, and investigate the related practical issues such as battery capacity. In Section 4.4, we present the system architecture of the proposed technique with detailed discussion on the induced overhead. The evaluation of the proposed technique is provided in Section 4.5, and the conclusion is given in Section 4.6.

4.2 Model of UWB Pulse Radar for Sensing Applications

In this section, we present the model of UWB-based sensing systems. The proposed technique exploits this model to develop adaptive mechanisms based on the link and energy conditions.

4.2.1 Self-sustained UWB Pulse Radar

Figure 4.1 shows the model of a UWB-based sensing system. Under the scope of this work, we consider that the transceiver is powered by renewable energy that is drawn from the ambient sources by the energy harvesting unit (EHU). Since

UWB pulses have a very low duty cycle, most of the time the transceiver will stay in silence thereby consuming a very low level of power. Thus, a rechargeable battery is needed to store the harvested energy for future use. The power management unit (PMU) collects the key parameters from the transceiver at runtime. These parameters, including the available energy in the battery E_b, average harvested energy E_h, and the signal-to-noise ratio (SNR) at the receiver, will be utilized to determine a suitable set of operation configurations to deal with the non-deterministic energy source and the varying target range (see Section 4.3).

Figure 4.2 shows the detailed block diagram of the UWB transceiver for sensing applications. UWB pulses with a repetition frequency R_p are generated by the pulse generator in the transmitter. These pulses are then transmitted directly to the target through the wireless link, which introduces non-ideal effects such as path loss and multi-path fading. After being reflected by the target, the pulses will be collected by the receiver. The received signals are first amplified by a low-noise amplifier (LNA) and then enter the two parallel processing units. The first unit, shown within the dashed frame in Fig. 4.2, correlates the received signals with the delayed local UWB pulses to estimate the delay time between the radar and the target, so that the distance to the target can be determined. Note that the target is assumed to be slow-moving and the detection range is relatively small. Under these conditions, the moving target is detectable using the coherent method. To improve the sensing performance such as the signal-to-noise ratio

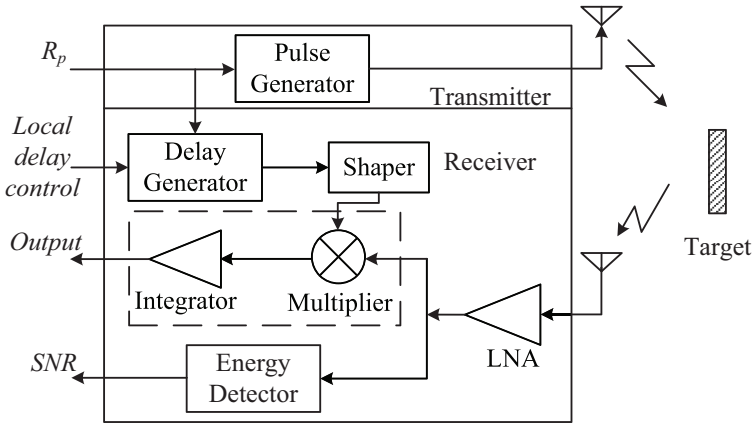

Fig. 4.2: UWB pulse radar transceiver for sensing applications.

(SNR), an integrator is employed after the correlator to accumulate the signal power of multiple received UWB pulses for coherent signal detection. The SNR at the receiver is estimated by the energy detector [93] in the second processing unit.

4.2.2 System Specifications

The sensing performance of the UWB pulse radar is quantified by the SNR γ at the receiver, which is expressed in decibels as

$$\gamma = \alpha + P_t - P_n, \tag{4.1}$$

where α, P_t, and P_n are the total link gain between the transmitter and the receiver, the transmitted UWB pulse power, and wireless channel noise power, respectively. In this work, the UWB pulse power P_t is pre-determined (e.g., regulated by FCC to be below -41.3dBm/MHz), and the channel noise power P_n is

assumed to be slow-changing because the UWB pulse radar is typically used for short range sensing. In order to meet a specific SNR requirement, it is necessary to tune the link gain α, which consists of path gain G_d, multi-path fading gain G_f, and the processing gain G_p of the integrator in the receiver, i.e.,

$$\alpha = G_d + G_f + G_p, \tag{4.2}$$

where the multi-path fading gain G_f is related to the reflection of UWB pulses in the outdoor environment. Due to the natural property of fine time resolution in UWB pulses, G_f is relatively small as compared with the path gain G_d [94], and thus can be considered as a constant that is independent of the distance to the target. On the other hand, the path gain G_d is distance-dependent, which is determined by

$$G_d(d) = G_0 - 10n \log_{10}(\frac{d}{d_0}), \tag{4.3}$$

where d is the signal propagation distance between the transmitter and receiver, d_0 is the reference distance, and G_0 is the path gain at d_0. The propagation exponent n equals 2 in the air medium.

To improve the time resolution, the integrator in the UWB transceiver (see Fig. 4.2) will update the detection result I times every second (e.g., update rate $I = 100$Hz). Within each update period, the UWB transceiver transmits and integrates N pulses (e.g., $N = 10^5$) to improve the SNR. As a result, the UWB

pulse repetition frequency R_p can be expressed as

$$R_p = I \cdot N, \tag{4.4}$$

where R_p represents the number of UWB pulses transmitted per second.

The processing gain G_p in (4.2) at the receiver is related to the integral of N received UWB pulses during one update period, defined as

$$G_p = 10\log_{10}(N). \tag{4.5}$$

Substituting (4.2)–(4.5) into (4.1), we can recast the SNR expression as

$$\gamma = G_0 - 10n\log_{10}(\frac{d}{d_0}) + G_f + 10\log_{10}(\frac{R_p}{I}) + P_t - P_n, \tag{4.6}$$

where G_0, G_f, P_t, and P_n can be considered as distance-independent. Thus, the SNR in (4.6) can be further simplified as

$$\gamma = 10\log_{10}(\frac{R_p}{I}) - 10n\log_{10}(\frac{d}{d_0}) + C, \tag{4.7}$$

where $C = G_0 + G_f + P_t - P_n$. Clearly, for a given R_p, the receiver SNR γ will increase as d reduces, i.e, when the target moves closer to the UWB transceiver. Rearranging (4.7), we obtain

$$R_p = I \cdot (\frac{d}{d_0})^n 10^{(\gamma - C)/10}. \tag{4.8}$$

In the conventional UWB pulse radar, pulse repetition frequency R_p is determined by the maximum detection range under a pre-specified SNR requirement.

Assuming a pre-specified SNR γ_s, the pulse repetition frequency $R_{p,c}$ of the conventional UWB radar can be calculated from (4.8) as

$$R_{p,c} = I \cdot (\frac{d_{max}}{d_0})^n 10^{(\gamma_s - C)/10}, \tag{4.9}$$

where d_{max} represents the maximum detection range.

Note that the conventional UWB technique employs a fixed pulse repetition frequency $R_{p,c}$ based on the maximum detection range d_{max} without considering the varying link condition and energy availability. When the link gain increases due to the movement of the target within d_{max}, the UWB transceiver operating at the $R_{p,c}$ will consume more energy than necessary. Thus, the conventional UWB transceiver works best when the energy supply is sufficient and stable.

4.3 Link and Energy Adaptive UWB Sensing

In this section, we develop a link and energy adaptive UWB-based sensing technique to exploit renewable energy sources. Since renewable energy sources are non-deterministic, the proposed technique dynamically adjusts the pulse repetition frequency at the transmitter by jointly considering the link gain and available energy to maximize the detection range and time coverage. We will first discuss the motivation and then present the details of the proposed technique.

4.3.1 Motivation

In natural environments, the target under the detection is unlikely to stay still, while the pulse repetition frequency of the conventional UWB radar is determined by the worst case scenario (i.e., the maximum detection range, see (4.9)) under a pre-specified SNR γ_s requirement. As the distance d between the UWB transceiver and the target is smaller than d_{max}, the receiver SNR γ in (4.7) will go above the pre-specified γ_s if R_p is fixed, i.e., the UWB radar is overperforming. On the other hand, the energy consumed by the UWB transceiver within each update period can be expressed as

$$E_t = \frac{R_p(E_p + E_{circ})}{I}, \tag{4.10}$$

where I is the update rate and E_p denotes the energy consumption of one UWB pulse, which includes the transmitter energy consumption in generating the pulse and the receiver energy consumption in processing the pulse. The standby energy, denoted by E_{circ}, which generally includes the energy for waiting the pulse to come, only accounts for a very small portion of the total energy consumption in the UWB system (around 2% on average [84], [95]). Thus it is ignored without affecting the results of the proposed technique. From (4.10), E_t in each update period is proportional to R_p. As a result, the UWB transceiver operating at the fixed $R_{p,c}$ for $d < d_{max}$ unnecessarily consumes more energy, as the receiver SNR is larger than the pre-specified requirement.

While not being a problem for conventional UWB sensing systems powered

by stable energy sources, this can significantly affect the sustainable operation in the device powered by renewable energy. As renewable energy sources are scarce, the transceiver is expected to often operate under the limited and even insufficient power supply. Using a fixed R_p regardless of the link gain may adversely affect the detection range and time coverage of the UWB radar. Note that both the detection range and time coverage are important performance metrics that are directly associated with the energy supply. For a given SNR γ_s, if the pulse repetition frequency R_p can be adaptively tuned with respect to the link gain (primarily determined by the distance between the transceiver and the target), large energy savings are possible. This can significantly improve the robustness of self-sustained UWB sensing. For example, the saved energy in the above case can be utilized later when the renewable energy level is low, or when the target is moving away from the UWB transceiver thereby requiring a higher R_p and thus a larger power budget. As a result, making R_p link adaptive is necessary for self-sustained UWB sensing.

In addition to the link gain, the non-determinism inherent in most renewable energy sources is another constraint for self-sustained UWB sensing. Consider solar radiation as an example. The harvested energy changes with time as well as other factors such as rain, cloud, and shadow, which introduce uncertainties to the available energy that can be utilized by the UWB radar. If the renewable energy (including the energy saved in the rechargeable battery) is not sufficient

due to the variations in environmental conditions, the pulse repetition frequency R_p may not be sustained at the desired level. Hence, it is important to develop a scheme that can improve the detection range and time coverage of UWB-based sensing systems by adaptively adjusting the pulse repetition frequency based on a composite effect of link gain and renewable energy level.

4.3.2 The Proposed Technique

Based on the above observations, we propose a link and energy adaptive technique for self-sustained UWB sensing applications. The proposed technique works as follows.

At the beginning of the i^{th} transceiver update period, the pulse repetition frequency R_p^i is determined by the link gain and renewable energy level. From (4.9), if the actual distance d_i between the UWB sensing transceiver and the target is smaller than d_{max} while the transceiver still sends pulses at the frequency of $R_{p,c}$, then the receiver output SNR γ_i (which can be estimated by the energy detector in Fig. 4.2) will be larger than the pre-specified γ_s. This situation is reflected by the following expression,

$$\begin{aligned} R_{p,c} &= I \cdot (\frac{d_i}{d_0})^n 10^{(\gamma_i - C)/10} \\ &= I \cdot (\frac{d_{max}}{d_0})^n 10^{(\gamma_s - C)/10}, \end{aligned} \tag{4.11}$$

where $d_i < d_{max}$ and thus $\gamma_i > \gamma_s$.

In this case, we can reduce the pulse repetition frequency to R_p^i so that the

pre-specified γ_s is just met, i.e,

$$R_p^i = I \cdot (\frac{d_i}{d_0})^n 10^{(\gamma_s - C)/10}. \tag{4.12}$$

Combining (4.11) and (4.12), we derive the pulse repetition frequency R_p^i for the i^{th} update period as

$$R_p^i = R_{p,c} 10^{(\gamma_s - \gamma_i)/10}, \tag{4.13}$$

where R_p^i is related with the actual SNR γ_i, which is a function of the distance between the target and UWB transceiver. As the target moves, the proposed technique will adjust the pulse repetition frequency R_p^i accordingly at runtime to save energy.

In (4.13), to determine the pulse repetition frequency R_p^i, we need to know the maximum pulse repetition frequency $R_{p,c}$, which is a function of the maximum detection range d_{max} under the pre-specified SNR requirement (see (4.9)). Note that the detection range is not a constant but changes with the available harvested energy. Thus, it is reasonable to consider the detection range as a random variable because renewable energy sources are usually modeled in a statistical way.

To find out the d_{max}, we assume that the renewable energy level is estimated by the PMU in Fig. 4.1 at the frequency of $1/T_s$ (e.g., the time slot $T_s = 0.5$ hour for solar energy). Ideally, the UWB transceiver should fully utilize the harvested energy and the energy stored in the rechargeable battery during every time slot;

e.g., for the j^{th} time slot, we have

$$\begin{aligned} E_h^j + E_b^j &= \sum_{k=0}^{k=M-1} E_t^k \\ &= \frac{\sum_{k=0}^{k=M-1} E_t^k}{M} \cdot M \\ &= \bar{E}_t \cdot M, \end{aligned} \tag{4.14}$$

where $M = I \cdot T_s$ is the number of update periods during each time slot T_s, and $\bar{E}_t$ is the average energy consumption of the UWB transceiver in each update period, i.e., the average value of E_t in (4.10). Substituting the average value of E_t in (4.10) into (4.14), we obtain

$$E_h^j + E_b^j = \bar{R_p}(E_p + E_{circ})T_s, \tag{4.15}$$

where $\bar{R_p}$ is the average pulse repetition frequency in each time slot. Consider that the object moves randomly in the range of $d_i \in [0, d_{max}]$, then

$$\bar{R_p} = \int_0^{d_{max}} f_{di} \cdot R_p^i \cdot d(d_i), \tag{4.16}$$

where R_p^i is a function of d_i, as expressed in (4.12), and f_{di} is the probability density function (PDF) of d_i, which is the distance between the UWB transceiver and the target during each update period. Note that the object moving beyond d_{max} is undetectable; thus there is no need to determine the pulse repetition frequency for this case. This condition, however, will be relaxed in the next subsection when we deal with some practical design issues.

To illustrate with a simple example, we consider the commonly used random walk model for the object movement. This model has been widely used in

mobile ad-hoc networks [96,97] to accurately reflect the statistical characteristics of moving objects in real situations. It was shown [96] that if the position and moving direction of the object is uniform at the beginning of the detection, then the position of the object will continue to follow the uniform distribution. Thus, the PDF of d_i is $f_{di} = 1/d_{max}$. Substituting this into (4.16), the average pulse repetition frequency $\bar{R_p}$ can be obtained as

$$\begin{aligned} \bar{R_p} &= \int_0^{d_{max}} \frac{1}{d_{max}} \cdot R_p^i \cdot d(d_i) \\ &= \frac{I}{n+1} \cdot \left(\frac{d_{max}}{d_0}\right)^n \cdot 10^{(\gamma_s - C)/10}. \end{aligned} \tag{4.17}$$

Combining (4.15) and (4.17), the maximum detection range d_{max} can be obtained as

$$d_{max} = \left\{ \frac{(E_h^j + E_b^j)(n+1)}{I R_p (E_p + E_{circ}) T_s 10^{(\gamma_s - C)/10}} \right\}^{\frac{1}{n}} \cdot d_0. \tag{4.18}$$

From (4.18), a higher renewable energy level enables a larger detection range. Rearranging (4.18), (4.11), and (4.13), the pulse repetition frequency R_p^i in the i^{th} update period can be expressed as

$$R_p^i = \frac{(E_h^j + E_b^j)(n+1)}{R_p (E_p + E_{circ}) \cdot T_s} 10^{(\gamma_s - \gamma_i)/10}, \tag{4.19}$$

where we can tune the pulse repetition frequency R_p^i according to the link gain γ_i and the available energy level $E_h^j + E_b^j$ at runtime.

Note that while the above discussion is based on the random walk model, the proposed technique is a general technique that does not depend upon any specific model.

4.3.3 Consideration of Practical Issues

Note that (4.19) is derived based on the estimated renewable energy at the beginning of the time slot. Since the renewable energy is non-deterministic, it is possible that the actual available energy is different from the estimated value. Thus, the calculated R_p may be occasionally larger than that the UWB radar can be actually operated. This happens when the harvested energy is less than the energy required by the UWB transceiver for several update periods. To deal with this problem, we will take different approaches to meet the performance requirement. Note that the energy consumption E_t^i of the UWB transceiver in the i^{th} update period can be determined by substituting R_p^i into (4.10). From the PMU, the available energy E_a^i in the current update period is the sum of renewable energy E_h^i and the energy in the battery E_b^i. If the available energy does not support the UWB transceiver to transmit at R_p^i, i.e., $E_a^i < E_t^i$, then two options are available. The first option, similar to the conventional UWB technique, is to simply shut down the UWB radar for the current update period. Note that the overall performance of the proposed technique under this option is still better than the conventional technique (see results in Section 4.5.2). The second and more rational option is to reduce the pulse repetition frequency to accommodate the available E_a^i, i.e.,

$$R_p^i = \frac{E_a^i I}{E_p + E_{circ}}. \tag{4.20}$$

In this case, a degradation in the output SNR is expected but the time

coverage is maintained. This is important for many sensing applications where full time coverage is critical while SNR performance is usually compromisable.

On the other hand, when the available energy is larger than the energy demanded by the UWB transceiver, i.e., $E_a^i \geq E_t^i$, the pulse generator will be tuned to generate pulses at the frequency of R_p^i. Since the transceiver is now consuming less energy, the unused harvested energy, if any, will be stored in the rechargeable battery for future use. Note that in practice, the battery always has a limited capacity, and thus battery overflow may occur. However, the proposed technique is relatively insensitive to the battery capacity. This is because the renewable energy can be more efficiently utilized thereby achieving better sensing performance than conventional UWB techniques under the same battery capacity (see results in Section 4.5.4).

4.4 System Design

In this section, we present the detailed design of the proposed technique. Considering the fact that energy harvesting is a non-deterministic process, it is reasonable to divide the whole day into several time slots (e.g., 0.5 hour/slot for solar energy harvesting) and estimate the renewable energy level at the beginning of each time slot. To achieve link and energy adaptive UWB sensing, the R_p of the UWB radar needs to be adjusted at each update period in the time slot.

The link and energy adaptive UWB sensing operation is summarized in

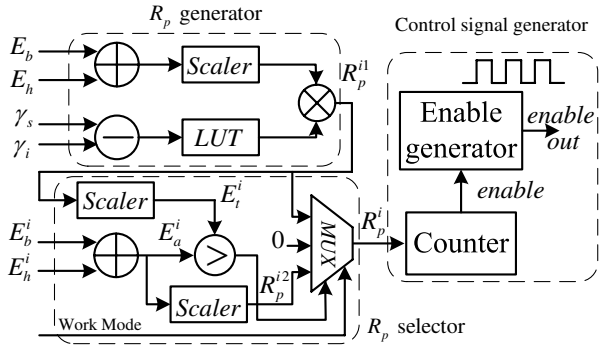

Fig. 4.3: Architecture of PMU in the proposed UWB transceiver.

Algorithm 4. The PMU (see Fig. 4.1) will be initialized with all the necessary information such as the pulse energy consumption E_p, time slot duration T_s, the pre-specified SNR requirement γ_s, available energy (E_h+E_b), and the receiver SNR γ_i from the energy detector (see Fig. 4.2). Note that many of these parameters, such as E_p, T_s, and γ_s, can be considered as constants, while the available energy (E_h+E_b) and the receiver output SNR γ_i will need to be updated at the beginning of each update period. The collected parameters are used to determine the pulse repetition frequency R_p according to (4.19) in the following update period of the same time slot.

Compared with the conventional UWB system, the proposed technique requires only a few new components such as the power management unit (PMU) (see Fig. 4.1) and the energy detector (see Fig. 4.2). The function of the PMU is to determine the proper pulse repetition frequency R_p^i at runtime based on the link and energy information, as expressed in (4.19). As shown in Fig. 4.3, the

PMU consists of three components: R_p generator, R_p selector, and control signal generator. The R_p generator determines the pulse repetition frequency at the beginning of each update period. The available energy $(E_h + E_b)$ of each time slot is first summed up and then scaled by the parameters E_p, and T_s. Note that the renewable energy E_h can be estimated accurately by employing existing low-complexity energy prediction algorithms [16,69]. Similarly, the battery status E_b can be detected by the battery monitoring unit [39]. The scaled $(E_h + E_b)$ is then multiplied with the value from the lookup table (LUT), addressed by the difference between γ_s and γ_i, to obtain the pulse repetition frequency R_p^i. The LUT is utilized here to avoid the complicated exponential computation in (4.19). The calculated R_p^i passes through the R_p selector, which adjusts the pulse repetition frequency for the current update period. Note that the *Work Mode* signal selects the different options when $E_t^i > E_a^i$ as discussed in Section 4.3.3. Finally, the control signal generator enables the pulse generator in Fig. 4.3 to generate UWB new pulses with the selected R_p^i.

The second component, the energy detector, estimates the SNR γ_i at the receiver based on the reflected pulses. The technique proposed in [93] can be employed to implement the energy detector, of which the major components include a squarer (multiplying the pulse by itself) cascaded with an integrator (accumulating the energy of multiple pulses). Note that the energy detector is activated as long as the receiver has pulse input, while the PMU works only at the beginning

of each update period. As a result, the energy overhead of the proposed technique comes mainly from the energy detector.

4.5 Evaluations

In this section, we evaluate the proposed link and energy adaptive UWB sensing technique. The performance results are based on Matlab simulations, and the energy parameters are obtained from the transceiver as discussed in Section 4.4, synthesized in a $90nm$ CMOS process, and powered by real-world measured solar energy as discussed in the next subsection. Practical issues, such as the battery capacity, are investigated to assess their impacts on the performance of the proposed technique.

4.5.1 Setup

Two commonly used solar energy models are utilized to obtain the repetitive yet non-deterministic solar energy patterns. The first model is based on the measured results from the National Climatic Data Center (NCDC), which provides the environmental measurements collected from various monitoring stations across the United States. The energy profile used in this work is obtained from its Renewable Energy Data Source database [47]. The solar energy radiation for a half year is shown in Fig. 4.4. This model captures both short-term (daily) and long-term (seasonal) variations in solar radiation.

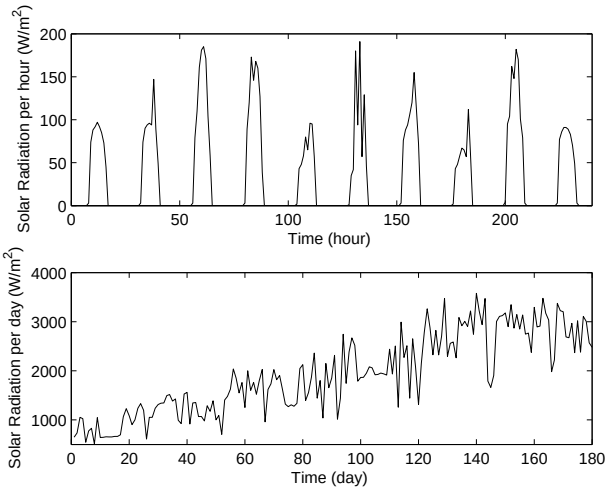

Fig. 4.4: Solar power from the field measurements by the National Climatic Data Center.

The second model is a statistical model [45,46] that describes the daily solar radiation as

$$P_h(t) = |10 \cdot N(t) \cdot \cos(\frac{t}{70\pi}) \cdot \cos(\frac{t}{100\pi})|, \tag{4.21}$$

where $N(t)$ is a normally distributed random variable with zero mean and unit variance. Figure 4.5 shows the results generated from this model, where the solar energy profile of ten days is depicted. Note that (4.21) describes the short-term (daily) variations in solar energy; it does not consider the long-term seasonal patterns. Both models will be applied to investigate the performance of the proposed link and energy adaptive UWB sensing technique based on the time period of six months. Note that the solar energy is converted by the solar panel of $10cm \times 10cm$ with an efficiency of 20%.

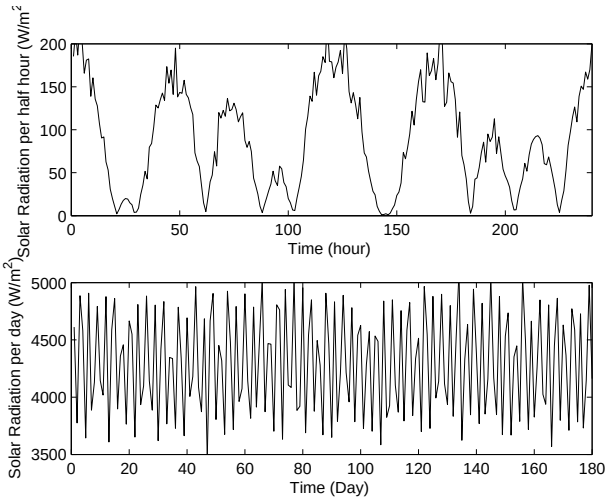

Fig. 4.5: Solar power from the statistical model.

The channel-related parameters such as the multi-path fading gain $G_f = -3dB$ and wireless channel noise power $P_n = -75dBm$ are obtained from the experimental results [98,99]. The reference distance d_0 is set at $2m$, the pre-specified SNR requirement γ_s is $5dB$, and each update period is set at $1/I = 0.01sec$. The gain G_0 at the reference distance d_0 can be tuned by adjusting the gain of LNA at the receiver, so that the UWB pulses are sent to meet the pre-specified SNR. The average energy consumption of the radar per pulse is about $42.9pJ$ when the pulse width is $350ps$. The standby energy consumption between two consecutive UWB pulses is around $1pJ$. The position of the target is described by the random walk model, which has been proved to accurately reflect the statistical characteristics of moving objects in the field [96,97]. Note that the range of object movement is not limited.

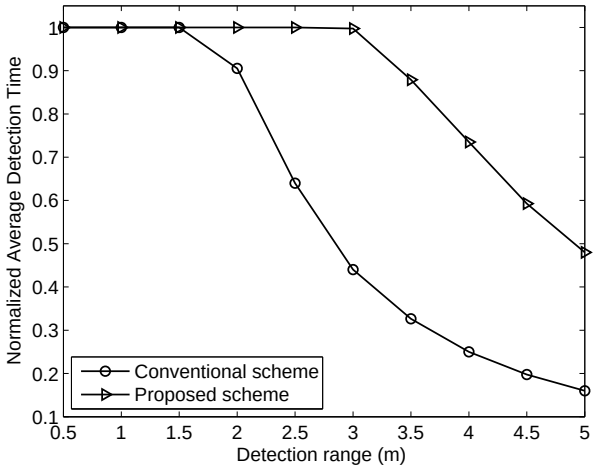

Fig. 4.6: Comparison of detection time coverage and range coverage under the statistical energy model.

4.5.2 Sensing Performance

The results in Fig. 4.6 are obtained by using the statistical solar energy model (4.21). These results compare the detection time coverage as a function of the detection range. The detection time coverage is defined as the portion of operation time within a day, during which the UWB transceiver has sufficient energy to support pulse transmission and collection. Note that the conventional UWB technique transmits UWB pulses at a fixed $R_{p,c}$ determined by (4.9). Both the conventional and the proposed UWB transceivers are powered down when the available energy is not sufficient to support the required R_p at the given γ_s (i.e., the proposed technique uses the first option in Section 4.3.3 in dealing with $E_a^i < E_t^i$). Note that this may cause battery overflow when the unused harvested

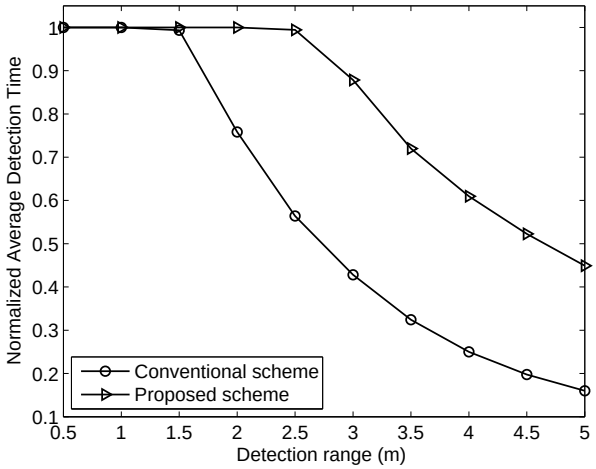

Fig. 4.7: Comparison of detection time coverage and range coverage under the measured energy results.

energy in the UWB transceiver is larger the battery capacity. Under such a circumstance, the extra energy will be lost. The battery capacity corresponding to these results is 20%, normalized by the average harvested energy of one day, and the battery has an average efficiency of 0.9 with 50% initial energy. The evaluation on different battery capacities will be presented in Section 4.5.4. As shown, the proposed technique significantly improves the detection range and time coverage by making the pulse repetition frequency link and energy adaptive; i.e., the detection range d_{max} increases from 1.5m for the conventional technique to about 3m for the proposed technique. At $d = 3$m, the conventional technique can only achieve about 45% of the time coverage (i.e., being powered down during 55% of the time due to insufficient energy). In contrast, the proposed technique can

reach 100% of the time coverage without incurring any SNR degradation.

Figure 4.7 shows the performance comparison under the measured solar energy results [47]. It can be seen that the performance is worse than that in Fig. 4.6. This is because the solar energy is obtained from field measurements, reflecting both short-term (daily) and long-term (seasonal) variations in solar radiation. Nevertheless, the proposed technique still achieves better performance than the conventional technique. Note that the detection time coverage will drop as d increases beyond d_{max}. However, achieving full time coverage may be needed in certain mission-critical sensing applications. To tradeoff SNR performance with the detection time coverage, we evaluate the second option in Section 4.3.3 in dealing with $E_a^i < E_t^i$. In this case, the pulse repetition frequency is further reduced to accommodate the available energy in order to keep the UWB transceiver operating at a lower SNR. In Fig. 4.8, 100% detection time coverage is maintained subject to the SNR degradation. Note that most embedded sensing applications can accept a moderate level of performance degradation. Thus, the proposed technique offers an effective solution that enables tradeoffs between performance and energy availability.

4.5.3 Energy Efficiency

We synthesized the PMU using Synopsys Design Compiler in a $90nm$ CMOS process, and estimated the energy consumption to be about $0.2\mu J$ using Synopsys

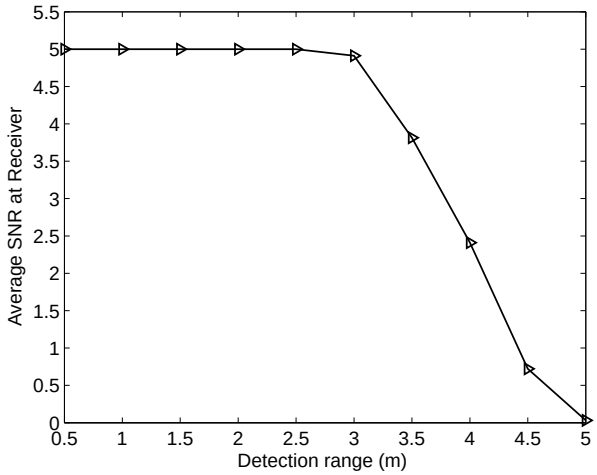

Fig. 4.8: Performance of the proposed technique to achieve 100% detection time coverage.

PrimeTime. In the proposed technique, the update period $I = 100Hz$ of the PMU is fixed, which results in an energy overhead equal to 4.7% of the total system. All the other components such as the energy detector [93] are the standard components in a UWB sensing system. Their energy consumptions have been included in the simulations.

Figure 4.9 compares the energy consumption within one update period under the different detection ranges between the conventional technique and the proposed technique. As the detection range increases, the energy consumption of the conventional technique increases at a much larger rate than the proposed technique. This is because the conventional UWB technique is based on the worst-case design, i.e., transmitting UWB pulses at a fixed $R_{p,c}$, while the proposed technique

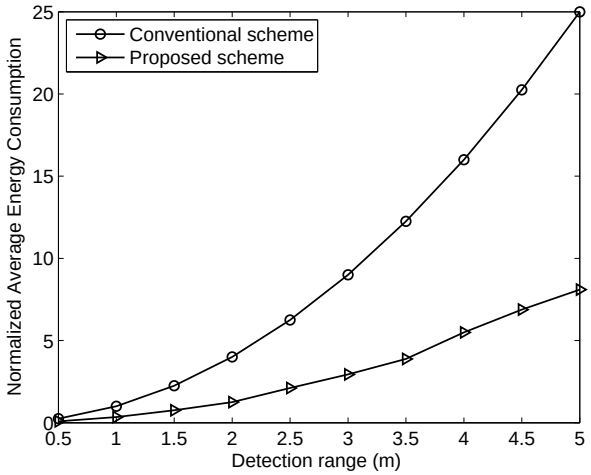

Fig. 4.9: Comparison of average energy consumption within one update period (normalized by the energy consumption of the conventional technique at $d = 1$m).

is more energy-efficient due to its adaptive nature.

4.5.4 Battery Capacity

We now evaluate some practical issues related to the limited battery capacity. Figure 4.10 shows the average detection time coverage under different values of the battery capacity (normalized by the average harvested energy of one day using measured solar energy results [47]). The detection range is selected to be [0, 2m]. As the battery capacity decreases (e.g., due to the battery aging effect), the conventional technique will suffer a large degradation in the detection time coverage. In contrast, the proposed technique is relatively less sensitive to the

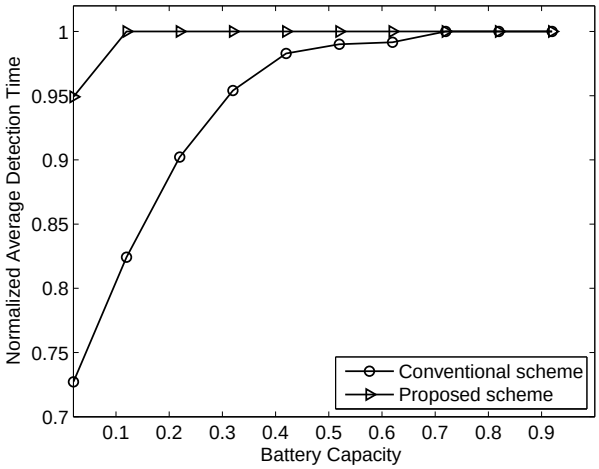

Fig. 4.10: Comparison of detection time coverage under different battery capacities.

battery capacity effect. This is because our technique adaptively adjusts the pulse repetition frequency of the UWB radar according to different energy/batter conditions. For example, if the battery capacity reduces, our technique will use a smaller pulse repetition frequency for continuous detection coverage, whereas the conventional technique using a fixed pulse repetition frequency will have to stop frequently due to the insufficient energy supply.

4.6 Conclusion

In this chapter, we propose a new link and energy adaptive UWB sensing technique to improve the sustainable operation of embedded sensing systems powered by renewable energy sources. The proposed technique allows the UWB radar to ef-

fectively deal with the limited and non-deterministic energy supply with negligible overheads. The maximum detection time coverage and detection range coverage are improved by exploiting the link information of the UWB radar and the non-deterministic renewable energy in a coherent manner. The proposed technique also enables good tradeoffs between detection time coverage and performance when a moderate performance degradation is acceptable, which is the case in most embedded sensing applications. Further work is being directed towards the hardware implementation of the proposed technique, applications of the proposed technique for multiple targets tracking, and extension to other applications, such as emergency management systems.

Algorithm 4: Link and energy adaptive operations for self-sustained UWB sensing.

Input:
E_p (One pulse energy consumption)
T_s (Energy harvest time slot duration)
γ_s (SNR requirement of UWB receiver)
γ_i (SNR output of UWB receiver at i^{th} update period)
E_b (Battery energy)
E_h (Harvested energy)
Output:
d_{max} (Maximum detection range)
$R_{p,c}$ (Maximum pulse repetition frequency)
R_p^i (Adaptive pulse repetition frequency)

```
begin
    % assuming L time slots in one day;
    for j ← 1 to L do
        % estimate E_h and E_b;
        % initialize the R_p ;
        % initialize the R_p ;
        % determine d_max ;
        Calculate d_max with (4.18);
        % obtain R_{p,c} ;
        Calculate R_{p,c} with (4.11) and transmit at the initialization;
        % find out the following R_p ;
        % assuming U update periods in one time slot;
        for i ← 1 to U − 1 do
            % estimate E_h^i and E_b^i and sum up to obtain E_a^i;
            % collect γ_i and calculate R_p^i Calculate R_p^i with (4.19);
            % calculate plan-to-use energy E_t^i
            Calculate E_t^i with (4.10);
            if E_t^i > E_a^i then
                Option 1: Power off transceiver;
                Option 2: Transmit at a lower R_p^i determined by (4.20);
            else
                Transmit at the calculated R_p^i.
            end
        end
    end
end
```

Chapter 5

Low-Power LDPC Decoder Design Exploiting Memory Error Statistics

This chapter presents a low-power LDPC decoder design by exploiting inherent memory error statistics due to voltage scaling. By analyzing the error sensitivity to the decoding performance at different memory bits and memory locations in the LDPC decoder, the scaled supply voltage is applied to memory bits with high algorithmic error-tolerance capability to reduce the memory power consumption while mitigating the impact on decoding performance. We also discuss how to improve the tolerance to memory errors by increasing the number of iterations in LDPC decoders, and investigate the energy overheads and the decoding throughput loss due to extra iterations. Simulation results of the proposed low-power LDPC decoder technique demonstrate that, by deliberately adjusting the scaled supply voltage to memory bits in different memory locations, the memory power consumption as well as the overall energy consumption of the LDPC decoder can be significantly reduced with negligible performance loss.

5.1 Introduction

Low Density Parity-Check (LDPC) codes offer excellent decoding performance and have been adopted by several digital communication standards, such as 802.11n, 802.16e and DVB-S2. However, the high power consumption of LDPC decoders due to the iterative decoding complexity has become the bottleneck in low-power applications of LDPC, such as wireless mobile devices. In the last decade, various low-power LDPC decoder techniques have been proposed at different levels of the design hierarchy. In [100], a technique was proposed to early terminate the computation when the convergence of the LDPC decoding is achieved. In [101], a memory-bypassing scheme was developed to reduce the amount of accesses to the memory that stores messages in the LDPC decoder. The layered decoding algorithm [102] speeds up the decoding convergence from the conventional flooding schedule, thereby reducing the power consumption.

Due to the iteration nature of LDPC decoders, a large amount of memory accesses are required. In WiMAX LDPC decoders, the memory accesses in one LDPC decoding iteration can reach up to $32,800$ [103]. It was also reported [104,105] that the power consumption of memory accesses accounts for more than 50% of the total power consumption in LDPC decoders. Therefore, reducing memory power consumption in LDPC decoders becomes a priority in low-power LDPC decoder design. Recently, aggressive voltage scaling techniques [88] have been applied as an effective way to reduce memory power consumption, espe-

cially for image processing [106] and wireless communications [107] applications. In [106], the low-order and high-order memory bits are powered by the scaled voltage and nominal supply voltage, respectively. This technique can reduce the memory power consumption with minor image quality degradation. In [107], the supply voltage of the memory is reduced when the wireless receiver experiences a relatively high channel gain. Note that both applications exploit the inherent error tolerance in the system, and the memory errors due to voltage scaling can be tolerated by the algorithm.

In LDPC decoders, some memory errors can be tolerated, while many will propagate through the iterative decoding process and thus deteriorate the decoding performance. Therefore, it is more challenging to employ voltage scaling on the memory in LDPC decoders. In this work, we propose to exploit memory error statistics to the design of low-power LDPC decoders. By analyzing the error sensitivity to the decoding performance at different memory bits and memory locations, the scaled supply voltage is applied to memory bits with high algorithmic error-tolerance capability to reduce the memory power consumption while mitigating the impact on decoding performance. We also discuss how to improve the tolerance to memory errors by increasing the number of iterations in LDPC decoders, and evaluate the resulted energy overheads and the decoding throughput loss due to extra iterations. Simulation results of the proposed low-power LDPC decoder technique demonstrate that, by deliberately adjusting the scaled

supply voltage to memory bits in different memory locations, the memory power consumption as well as the overall energy consumption of the LDPC decoder can be significantly reduced with negligible performance loss.

The rest of the chapter is organized as follows. Section 5.2 briefly discusses the background of LDPC decoders. Section 5.3 studies the memory error statistics and the performance impact of different memory bits and different memory locations. Then, a low-power LDPC decoder design technique is developed to exploit memory error statistics for power reduction. Simulation results are evaluated in Section 5.4, and the conclusion is given in Section 5.5.

5.2 Background of LDPC decoders

Figure 5.1 shows a generic LDPC decoder, which consists of multiple processing units and the associated memory blocks. Two groups of processing units, namely variable nodes units (VNU) and check node units (CNU), exchange messages according to the pre-defined connections in the sparse parity-check matrix of the corresponding LDPC code. These messages are defined as the belief measurement of the received bit information in the form of the log-likelihood ratio (LLR).

Among all LDPC decoders, the min-sum (MS) decoder [108] is the most commonly used due to its hardware simplicity and good performance. One full iteration of MS decoding consists of two phases: check node update and variable node update. In the check node update, the CNU reads all the neighbouring VNU

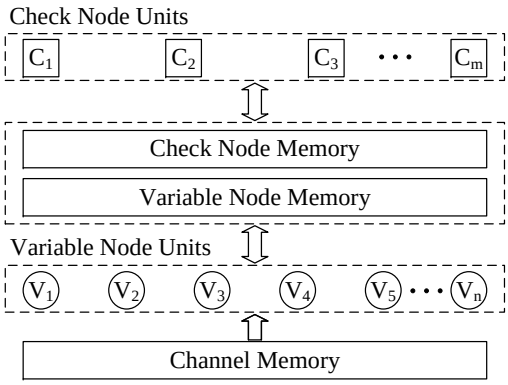

Fig. 5.1: A generic architecture of the LDPC decoder.

outputs from the VNU memory, and performs the MIN operation as,

$$R_{mn}^{i} = \left(\prod_{n' \in N(m) \backslash n} \text{sign}(Q_{n'm}^{i-1}) \right) \min_{n' \in N(m) \backslash n} |Q_{n'm}^{i-1}|, \tag{5.1}$$

where Q_{nm}^{i} and R_{mn}^{i} are the message from VNU n to CNU m and the message from CNU m to VNU n in the i-th iteration, respectively, and the sign( ) operation returns the MSB (i.e., the sign bit) of the message. Then, the outputs of CNU will be written back into the the associated CNU memory.

During the variable node update, the VNU will access the CNU output from the associated CNU memory as well as the received symbols from the channel memory, and then conduct the SUM operation as,

$$Q_{mn}^{i} = L_n + \sum_{m' \in M(n) \backslash m} R_{m'n}^{i}, \tag{5.2}$$

where L_n is the initial LLR message for VNU n from the received symbol. The outputs of VNU will then be stored into the associated VNU memory. A decoding

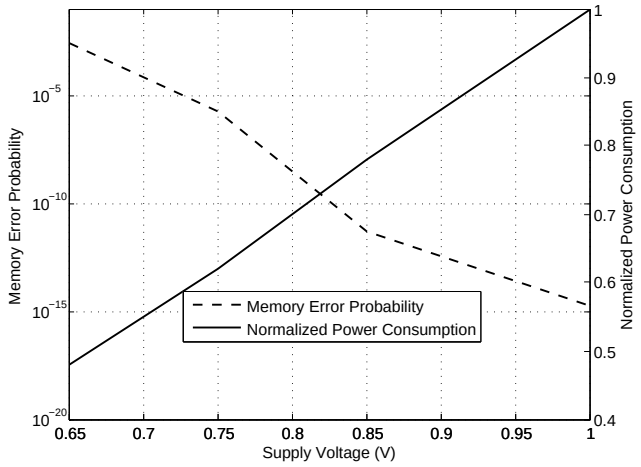

Fig. 5.2: Memory supply voltage vs error rate.

decision will be made at the end of each iteration as,

$$x^i = \text{sign}(L_n + \sum_{m \in M(n)} R^i_{mn}), \tag{5.3}$$

where only the signs of the messages will be utilized for decoding.

The decoding will continue iteratively in the same manner until the maximum iterations are reached, or the early termination mechanism [100] is evoked when all the errors are eradicated before the maximum iterations. It is worth mentioning that the memory accesses required in the computations in (5.1)–(5.3) contribute to most of the power consumption of the LDPC decoder. It was reported [104,105] that memory accesses account for more than 50% of the total power consumption in the LDPC decoder. Therefore, reducing memory power consumption is critical for low-power LDPC decoder design.

5.3 Low-power LDPC decoder exploiting memory error statistics

With technology scaling, on-chip memory circuits experience large process variations such as random dopant fluctuation (RDF) [109], which make memory bit upsets easy to occur. This is particularly a problem when voltage scaling is applied as a common practice to reduce memory power consumption [110,111]. More specifically, reducing the supply voltage in memory will lead to spatially random uniform bit flipping. This phenomenon has been observed in [107] as shown in Fig. 5.2. In this work, we will exploit the underlying memory error statistics to reduce the power consumption of LDPC decoders.

5.3.1 Memory error models for LDPC decoders

As shown in Fig. 5.3, memory errors may be introduced due to lowering the supply voltage of all memory blocks in the LDPC decoder. Memory errors in the channel memory, VNU memory, and CNU memory can all be modeled as an additive random variable with the error probability P_{err}. Note that the channel memory will keep the received symbols unchanged until the end of the decoding process. Thus, any bit errors in the channel memory will manifest at the same bit locations in the received symbols. Therefore, the LDPC decoder will treat the channel memory errors as the errors in the received symbols. On the other hand, the contents in the VNU/CNU memory will be updated at the end of each iteration in LDPC decoding. This makes the decoding process more exposed to the errors

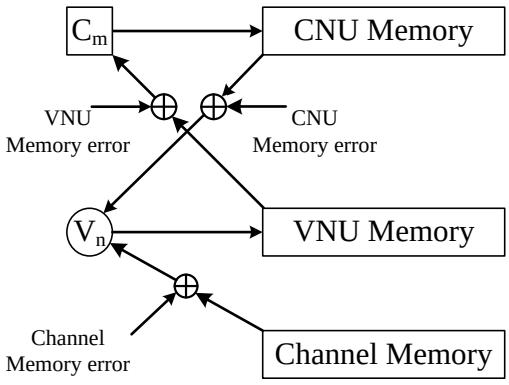

Fig. 5.3: Memory error model for LDPC decoders.

from the VNU/CNU memory. This is because VNU and CNU memory errors can propagate, accumulate, and generate more errors under some conditions. Even though the LDPC decoder can naturally tolerate some of these errors [112], many errors that cannot be tolerated will propagate to the subsequent iterations.

To illustrate the error occurrence in the Min-Sum LDPC decoder, a simplified message exchange process is shown in Fig. 5.4. Note that in Fig. 5.4 the number pairs separated by a slash represent the message value without and with memory errors, respectively. Quantized to 5 bits with a 1-bit fractional part, the maximal and minimal message values are 7.5 and -8, respectively. Figures 5.4(a)–(b) show the case that an memory error occurs at the 2nd LSB of the 5-bit message. As shown, the message value from VNU3 (V3) will be erroneously changed from 7 to 6 when CNU1 (C1) reads these memory cells due to the bit flipping at the 2nd LSB. After the CNU update (see (5.1)) in Fig. 5.4(a), the messages returned back to the neighbouring VNUs still remain the correct values. This shows the

case that the memory errors can be completely tolerated and thus have no impact on the following operations. Similarly, in Fig. 5.4(b), though an error occurring in the message from C3 to V1 will propagate to the next iteration after V1 update (see V1 $\rightarrow$ C2), the sign of the message does not change. So the errors in Figs. 5.4(a)–(b) can be tolerated by the LDPC decoding algorithm and there is not performance loss.

Figures 5.4(c)–(d) show the opposite situation. An error occurring at the 2nd MSB in the message changes the message value from 7 to 3. In Fig. 5.4(c), the error in the message from V3 to C1 will propagate and multiply into two message errors (see C1 $\rightarrow$ V1 and C1 $\rightarrow$ V2). This trend appears in the VNU update (see (5.2)) in a similar way. As a result, the LDPC decoder is not immune to these errors and significant degradation in the decoding performance is expected. In sections 5.3.2 and 5.3.3, we will explain more details related to Fig. 5.4.

The above two different situations can be characterized statistically as follows.

- *Memory error tolerance*: $P_{err} > \Delta BER$, where ΔBER denotes the increase in the LDPC decoder bit-error rate (BER) due to the additional memory errors with a probability P_{err}. If the induced ΔBER is much less than P_{err}, the LDPC decoder can mitigate the memory error impact by itself. Note that a smaller ΔBER indicates a better error tolerance.

- *Memory error propagation*: $P_{err} < \Delta BER$. In many cases, the change in

the BER is larger than P_{err}, indicating that memory errors are multiplied due to the feedback of the iterative decoding process.

In view of these features, factors affecting the decoding performance will be investigated in the following subsections, and the guideline of the proposed low-power LDPC decoder design will be derived.

For the purpose of illustration, the LDPC decoder performance is analyzed for the $N = 1008$, $K = 504$, $d_v = 3$, and $d_c = 6$ regular LDPC code, which can be accessed online [113]. This implies that the LDPC decoder has 1008 VNUs and 504 CNUs; and each VNU (CNU) is connected with 3 (6) CNUs (VNUs). Every LDPC message is quantized to 5 bits. Note that while the numerical results may vary for different LDPC codes, the trend of error statistics remains more or less the same.

5.3.2 Errors at different memory bits

As previously discussed, the outputs of the LDPC decoder are based on the sign bits of messages. As long as memory errors do not upset the sign bits, the performance of LDPC decoder will not be affected. Thus, it is important to protect the most significant bits (MSB) of messages, as they are more sensitive to memory errors. Considering that the LDPC decoder will accumulate the messages (SUM operations in VNU) and compare the messages (MIN operations in CNU), it is possible that a memory error occurring at the lower bit location (e.g., the least

significant bit (LSB)) can eventually flip the MSB due to message accumulation and comparison through multiple iterations. However, the probability of these events is much smaller than those due to memory errors directly at the MSBs. Therefore, reducing the supply voltage of lower bits in the memory is expected to have a smaller impact on decoder performance. This is also illustrated in Fig. 5.4, where the error at the higher bit location (2nd MSB) (see Figs. 5.4(c)–(d)) can propagate and generate more errors than the error at the lower bit location (2nd LSB) (see Figs. 5.4(a)–(b)). In other words, the LDPC decoder is more vulnerable to memory errors at higher bit locations.

To assess the impact of supply voltage scaling on LDPC decoder performance, we simulate the decoding process with the memory error probability $P_{err} = 0.0027$ when the supply voltage is lowered from the nominal voltage $1V$ to $0.65V$. Note that P_{err} of single bit has an order of 10^{-3}, thus the chance of multiple bit errors in one LDPC symbol is negligible. More specifically, although supply voltage scaling can be applied to the arbitrary bits in the memory, only one bit error occurs in every LDPC symbol with the error location varying in the symbol. The value of P_{err} is obtained from Fig. 5.2. The maximum iteration is set at 10. Note that supply voltage scaling is only applied to the memory cells corresponding to the last four bits of the message. The memory cells storing the MSBs are always powered by the nominal supply voltage. As shown in Fig. 5.5, lowering the supply voltage of the last 3 bits in the messages will only incur minor

performance loss due to the inherent error tolerance; but the memory power savings can be as high as 31% compared with the decoder under the nominal supply voltage. Note that all the comparisons in Fig. 5.5 and hereafter are performed across different input LDPC signal qualities in terms of the signal-to-noise ratio (Eb/N0) from 1.8dB to 3dB. To the first order of approximation, the overall memory power consumption can be expressed by

$$P_{mem} = P(V_L) \times bits(V_L) + P(V_H) \times bits(V_H), \tag{5.4}$$

where $P(V_L)$ and $P(V_H)$, obtained from Fig. 5.2, denote the power consumption under the scaled supply voltage and the nominal supply voltage, respectively; $bits(V_L)$ and $bits(V_H)$ are the number of memory bits with the scaled supply voltage and the nominal supply voltage, respectively. In the above example, the decoder with the scaled supply voltage consumes about 69% of the memory power under the nominal supply voltage. Furthermore, when the scaled supply voltage is applied to the last 4 bits, the memory power savings will increase to 42%; however, this also induces about $0.1dB$ performance loss due to memory error propagation.

5.3.3 Errors at different memory locations

During the LDPC iterative decoding process, the CNU and VNU demonstrate different characteristics in terms of error tolerance and propagation. Compared with the MIN operation (see (5.1)) in CNU, the SUM operation (see (5.2)) in VNU is more sensitive to memory errors because an error in the operands of the SUM

operation can easily propagate to the MSBs of the output messages, which are used to determine the final codeword (see (5.3)). The sign change (MSB bit-flipping) in the message will deteriorate the LDPC decoder performance. Therefore, the errors occurring at the CNU memory, which stores the operands for VNU update, can potentially cause larger performance loss than the errors in the VNU memory. This is also shown in Figs. 5.4(d), where the message error (7 is upset to 3) after the VNU update changes the sign bit of the output message (2 becomes -2).

Figure 5.6 further compares the performance impact of errors at different memory locations. The sizes of VNU memory, CNU memory, and channel memory are $1008 \times 3 \times 5$ bits, $504 \times 6 \times 5$ bits, 1008×5 bits, respectively. The simulation is based on the memory error probability $P_{err} = 0.0027$ and the maximum iterations being 10. Memory errors are assumed to occur at the last 4 bits in the 5-bit messages. As shown, errors occurring uniformly at all memory locations (CNU memory, VNU memory, and channel memory) cause the largest performance loss, among which the CNU memory errors are the biggest contributor to the performance loss. The overall memory power consumption without any performance loss, e.g., scaling the supply voltage of the last 4 bits of the messages in the VNU memory and channel memory from $1V$ to $0.65V$, reduces to 76% of the memory power under the nominal supply voltage.

The fact that different memory bits and locations have different error characteristics in the LDPC decoder motivates us to consider applying voltage scaling

in accordance with memory error sensitivity. In Fig. 5.6, the LDPC decoder with the last 2 bits at the CNU memory and last 4 bits at the VNU/channel memory subject to voltage scaling induced errors can maintain the BER performance very well. The memory power consumption are then obtained as,

$$P_{mem} = \sum_{i=1}^{3} \left(P(V_L) \times bits^i(V_L) + P(V_H) \times bits^i(V_H) \right), \tag{5.5}$$

where $bits^i(V_L)$ and $bits^i(V_H)$ denote the number of memory bits under the scaled voltage and nominal voltage, and i ranging from 1 to 3 represents CNU memory, VNU memory, and channel memory in the LDPC decoder, respectively. According to (5.5), the LDPC decoder in this case only consumes about 67.3% of the total memory power consumption under the nominal supply voltage.

5.3.4 Reducing memory error impact by increasing iterations

The performance of the LDPC decoder can benefit from increasing the number of iterations. This can be applied to mitigate the performance loss due to scaling memory supply voltage. In Fig. 5.7, the LDPC decoder with a maximum iteration number of 11 can mitigate the memory errors, particularly for the received symbols with high E_b/N_0 (e.g., 3 dB), where all the memory errors, including those from the CNU memory, can be completely corrected. Further increase of iteration number to 12 can correct the errors from the memory as well as the errors from the received symbols.

To mitigate the performance loss due to memory errors stemmed from supply

voltage scaling, one can increase the number of iterations at the cost of decoder throughput and some energy overhead. Thus, an optimal LPDC decoder design should ensure that the power savings obtained from memory voltage scaling can easily offset the energy overhead due to increased iterations. To evaluate the total energy consumption of the LDPC decoder, assume that the total energy consumption of the LDPC decoder under the nominal voltage and the scaled voltage is E_{total} and E_{total}^{new}, then

$$E_{total} = (P_{mem} + P_{logic}) \times N_{iter}, \tag{5.6}$$

and

$$E_{total}^{new} = (P_{mem}^{new} + P_{logic}) \times (N_{iter} + \Delta N_{iter}), \tag{5.7}$$

where P_{mem}, P_{logic} and N_{iter} are the memory power consumption under the nominal supply voltage, logic core power consumption, and the average number of iterations; P_{mem}^{new} and ΔN_{iter} are the memory power consumption under the scaled supply voltage and the increased iterations. Note that P_{mem}^{new} can be determined by (5.5), and N_{iter} and ΔN_{iter} are obtained from Fig. 5.8.

5.3.5 Summary of the proposed technique

To exploit the above memory error statistics, the proposed low-power LDPC decoder design involves finding the solution that enables the minimal energy consumption E_{total}^{new} as expressed in (5.7) under a given set of performance constraints (e.g., SNR, throughput). It starts with assigning the scaled supply voltage to all

bits except for the MSB in all memories. If performance constraints are not satisfied, the higher bits of the CNU memory will be powered by the nominal voltage or an increased iteration number is adopted. This is because CNU memory errors have a greater impact on the decoder performance, while a small increase in iterations is able to correct most of the memory errors. This procedure continues until the minimal E_{total}^{new} is achieved subject to the performance constraints. Note that this procedure can be run off-line until the optimal bit numbers under the scaled supply voltage in different memories are determined. Once the optimal allocation about the scaled supply voltage is obtained, it can be stored in the lookup table (LUT) for future use.

Note that in [106] a reconfigurable SRAM architecture was proposed that can dynamically assign two different supply voltages on an SRAM array. The hardware implementation of the proposed technique can leverage this SRAM architecture. In Fig. 5.9, the modified SRAM array groups the same bits of different words into sub array bits 0-4 for separate power supplies. The supply voltage is selected between the nominal voltage V_{norm} and the scaled voltage V_{low} via the pull-up networks. Note that as aforementioned, the MSB (Sub array bit 4) is directly connected with V_{norm} to reduce the performance impact. The selection signals ($sel_0 - sel_3$) will be retrieved from the LUT before the normal LDPC decoding. Consider the fact that the estimated reconfiguration time is in the order of nanosecond [106], and reconfiguration is only required when the LDPC input

SNR changes, the reconfiguration impact is minimal. Also as will be shown in the next section, the power savings of our proposed technique are noticeable, which can easily compensate for the power overhead incurred by the extra components (e.g., LUT and pull-up networks) in Fig. 5.9.

5.4 Simulation Results

In this section, we will evaluate the proposed low-power LDPC decoder design. The memory error statistics is exploited by assigning the scaled supply voltage to different memory bits as well as different memory locations of the LDPC decoder according to their impacts on decoder performance.

The sizes of VNU memory, CNU memory, and channel memory are $1008 \times 3 \times 5$ bits, $504 \times 6 \times 5$ bits, 1008×5 bits, respectively. Several configurations of the scaled voltage in different memories are listed in Table I. Note that the digits in the first 3 columns represent the bit numbers under the scaled supply voltage, and the bit numbers are counted from the LSB in the message. The scaled voltage and the nominal voltage are $0.65V$ and $1.0V$, respectively. Memory power consumption is 0.48 normalized by the total decoder power consumption under the nominal voltage, based on the 6T SRAM in 65 nm proces technology [107]. The memory bit error probability $P_{err} = 0.0027$ at $0.65V$ based on Fig. 2. The memory errors are modeled as a spatially uniform random variable. Note that the memory read/write speed remains the same as supply voltage scaling is applied

only to memory cells. Thus, cells with more delay than the maximum access time due to the lower supply voltage will generate errors.

Table 5.1: Configuration of memory bits with scaled voltage in different memories.

	CNU memory	VNU memory	Channel memory	Maximum iterations
Case 0	0	0	0	10
Case 1	4	4	4	10
Case 2	2	4	4	10
Case 3	4	4	4	11
Case 4	3	4	4	11

Table II compares the performance loss ΔSNR, the increased average iterations ΔN_{iter}, normalized memory power consumption, and total LDPC energy consumption. Note that case 0 is the baseline without memory voltage scaling, which targets 10^{-3} bit-error rate. The required SNR and average iterations for the baseline are 2.72 dB and 7.59 when the maximum number of iterations is set as 10. Note that the memory power consumption and overall energy consumption in Table II are determined by (5.5) and (5.7). In (5.7), $P_{logic} = 0.5$ normalized the overall power consumption. In most LDPC decoders, P_{logic} is comparable to P_{mem}. According to Tables I and II, Case 1 where the last 4 bits in all memories

are powered by the scaled voltage consumes the lowest memory power as well as overall energy. However, it will incur about $0.11dB$ SNR loss. Case 2 can reduce the SNR loss with only 2 bits in CNU memory powered by the scaled voltage, but it will introduce extra iterations, which will decrease the LDPC decoder throughput and incur more overall energy consumption compared with Case 1. In Cases 3 and 4, maximum iterations of 11 are conducted to reduce the SNR loss. As shown, memory power consumption can still remain unchanged, while the overall energy consumption will rise due to the increased average iterations ΔN_{iter}. From these results, the proposed low-power LDPC decoder design offers a variety of options for power-performance tradeoffs, which are essential for a wide range of applications.

Table 5.2: Comparison of performance and power consumption for different design options.

	ΔSNR	ΔN_{iter}	Memory power consumption	Overall energy consumption
Case 0	0	0	1	1
Case 1	0.11	0	0.584	0.792
Case 2	0.02	0.06	0.673	0.843
Case 3	0.05	0.35	0.584	0.829
Case 4	-0.03	0.42	0.628	0.859

5.5 Conclusions

In this chapter, we developed a low-power LDPC decoder design by applying the aggressive voltage scaling technique on the memory. We discussed the error sensitivity of different memory bits to the LDPC decoder performance, and proposed to reconfigure the scaled supply voltage to the memory bits with higher error tolerance capability to mitigate the memory error impact. We also evaluated the energy overhead and the decoding throughput loss due to increased iterations in LDPC decoder. Simulation results demonstrate that the proposed technique can significantly reduce the energy consumption of LDPC decoder with minimal performance loss. Future work is directed towards developing an optimal design framework incorporating the proposed technique and other memory error mitigation methods to further improve the error tolerance and energy efficiency.

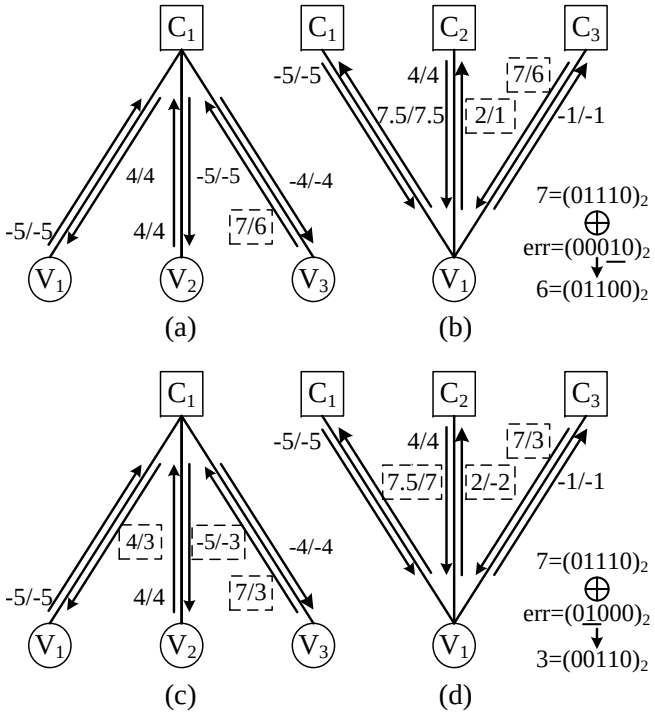

Fig. 5.4: Illustration of memory error tolerance and error propagation in LDPC decoders. (a) Check node update with an error at the 2nd LSB memory bit, (b) variable node update with an error at the 2nd LSB memory bit, (c) check node update with an error at the 2nd MSB memory bit, and (d) variable node update with an error at the 2nd MSB memory bit.

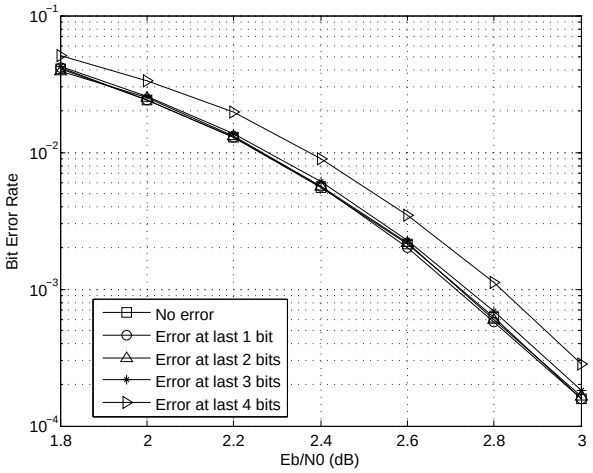

Fig. 5.5: Performance comparisons for memory errors at different bit locations.

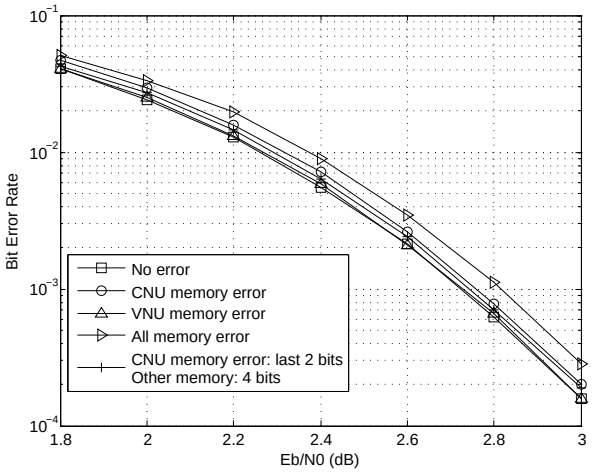

Fig. 5.6: Performance comparisons for memory errors at different memory locations.

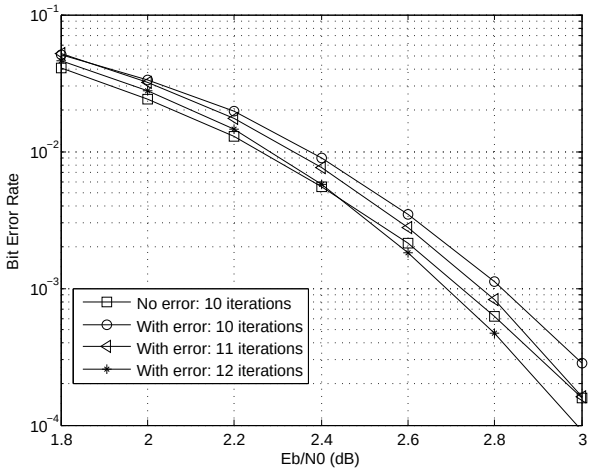

Fig. 5.7: Impact of the number of iterations.

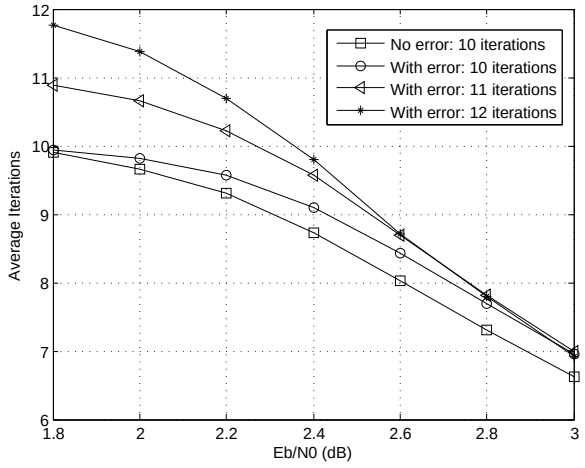

Fig. 5.8: Performance of average number of iterations.

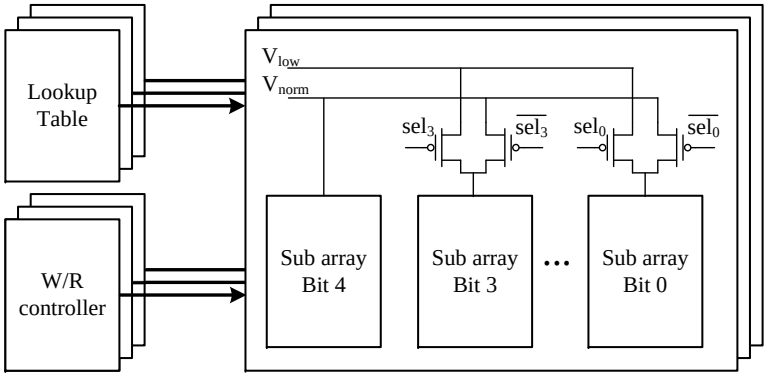

Fig. 5.9: Implementation of the proposed technique.

Chapter 6

Summary

In this dissertation, we have proposed to improve the energy efficiency of the embedded systems by jointly exploiting the properties of the power supply and the domain-specific information in the design of the embedded systems. We identify four power-hungry signal processing units, which are commonly employed in most of the embedded systems, and develop the corresponding algorithms to make full use of the energy when the power supply can not be regarded as a fixed source or provide normal voltage to the system.

In Chapter 2, we first analyze the challenges experienced by the RF circuits in the embedded systems under renewable energy, i.e., the time-varying wireless channel and the non-deterministic energy harvesting processes, and then develop an energy-adaptive modulation technique to maximize the data rate of the RF circuits by dynamically selecting the optimal modulation schemes according to the energy level and the channel conditions.

In Chapter 3, we investigate the non-linear relationship between signal processing performance and the required energy, which is usually available in most

signal processing systems, such as image and video signal processing. By considering this unique relationship between performance and energy consumption and the available renewable energy, we develop a progressive performance tuning method to allocate the energy among different harvested time slots to maximize the system performance.

In Chapter 4, we propose a novel link and energy adaptive UWB sensing technique to dynamically adjust the pulse repetition frequency in the UWB transceiver by considering the variable link gains of the UWB radar and the unstable renewable energy. The proposed adaptive technique can achieve better detection time coverage and range coverage due to the utilization of link and energy information.

In Chapter 5, we develop a low power LDPC decoder by exploiting inherent memory error statistics due to voltage overscaling. By analyzing the error sensitivity of the LDPC decoding algorithm at different memory bits and memory locations, we propose to apply the scaled supply voltage to memory bits with high algorithmic error-tolerance capability to achieve the low power design with minimal performance loss.

Bibliography

[1] J. Chen, J.-H. Cui, and L. Wang, "RF power management via energy-adaptive modulation for self-powered systems," *IEEE Transactions on Very Large Scale Integration (VLSI) Systems*, vol. 23, no. 9, pp. 1931–1935, 2015.

[2] ——, "Energy-adaptive modulation for RF power management under renewable energy," in *IEEE Workshop on Signal Processing Systems (SiPS)*, 2012, pp. 173–178.

[3] J. Chen and L. Wang, "Energy-adaptive performance management for self-sustained signal processing systems," in *IEEE Workshop on Signal Processing Systems (SiPS)*, 2014, pp. 1–6.

[4] ——, "Energy-adaptive signal processing under renewable energy," *Journal of Signal Processing Systems*, pp. 1–14, 2015.

[5] J. Chen, D. Zhao, and L. Wang, "Link and energy adaptive UWB-based embedded sensing with renewable energy," in *2013 IEEE International Symposium on Circuits and Systems (ISCAS)*, 2013, pp. 1825–1828.

[6] ——, "Self-sustained UWB sensing: A link and energy adaptive approach," *Journal of Signal Processing Systems*, pp. 1–11, 2015.

[7] J. Chen and L. Wang, "Low-power LDPC decoder design exploiting memory error statistics," in *IEEE International Symposium on Defect and Fault Tolerance in VLSI and Nanotechnology Systems (DFTS)*, 2015, pp. 171–176.

[8] W. K. Seah, Z. A. Eu, and H.-P. Tan, "Wireless sensor networks powered by ambient energy harvesting (WSN-HEAP)-survey and challenges," in *Wireless Communication, Vehicular Technology, Information Theory and Aerospace & Electronic Systems Technology, 2009. Wireless VITAE 2009. 1st International Conference on.* IEEE, 2009, pp. 1–5.

[9] S. Bergbreiter and K. S. Pister, "Design of an autonomous jumping microrobot," in *IEEE International Conference on Robotics and Automation.* IEEE, 2007, pp. 447–453.

[10] S. Kerzenmacher, J. Ducrée, R. Zengerle, and F. Von Stetten, "Energy harvesting by implantable abiotically catalyzed glucose fuel cells," *Journal of Power Sources*, vol. 182, no. 1, pp. 1–17, 2008.

[11] X. Jiang, J. Polastre, and D. Culler, "Perpetual environmentally powered sensor networks," in *Fourth International Symposium on Information Processing in Sensor Networks (IPSN)*. IEEE, 2005, pp. 463–468.

[12] L. Mateu and F. Moll, "Review of energy harvesting techniques and applications for microelectronics," in *Microtechnologies for the New Millennium 2005*. International Society for Optics and Photonics, 2005, pp. 359–373.

[13] S. Sudevalayam and P. Kulkarni, "Energy harvesting sensor nodes: Survey and implications," *IEEE Communications Surveys & Tutorials*, vol. 13, no. 3, pp. 443–461, 2011.

[14] R. Amirtharajah, J. Collier, J. Siebert, B. Zhou, and A. Chandrakasan, "Dsps for energy harvesting sensors: applications and architectures," *IEEE Pervasive Computing*, no. 3, pp. 72–79, 2005.

[15] C. Alippi and C. Galperti, "An adaptive system for optimal solar energy harvesting in wireless sensor network nodes," *IEEE Transactions on Circuits and Systems I: Regular Papers*, vol. 55, no. 6, pp. 1742–1750, 2008.

[16] S. Liu, J. Lu, Q. Wu, and Q. Qiu, "Harvesting-aware power management for real-time systems with renewable energy," *IEEE Transactions on Very Large Scale Integration (VLSI) Systems*, vol. 20, no. 8, pp. 1473–1486, 2012.

[17] A. Kansal, J. Hsu, S. Zahedi, and M. B. Srivastava, "Power management in energy harvesting sensor networks," *ACM Transactions on Embedded Computing Systems (TECS)*, vol. 6, no. 4, p. 32, 2007.

[18] D. Niyato, E. Hossain, M. M. Rashid, and V. K. Bhargava, "Wireless sensor networks with energy harvesting technologies: a game-theoretic approach to optimal energy management," *IEEE Wireless Communications*, vol. 14, no. 4, pp. 90–96, 2007.

[19] R. Min, M. Bhardwaj, S.-H. Cho, A. Sinha, E. Shih, A. Wang, and A. Chandrakasan, "An architecture for a power-aware distributed microsensor node," in *2000 IEEE Workshop on Signal Processing Systems (SiPS)*. IEEE, 2000, pp. 581–590.

[20] V. Raghunathan, A. Kansal, J. Hsu, J. Friedman, and M. Srivastava, "Design considerations for solar energy harvesting wireless embedded systems," in *Proceedings of the 4th international symposium on Information processing in sensor networks*. IEEE, 2005, p. 64.

[21] D. Li and P. H. Chou, "Application/architecture power co-optimization for embedded systems powered by renewable sources," in *Proceedings of the 42nd annual Design Automation Conference*. ACM, 2005, pp. 618–623.

[22] M. Gorlatova, P. Kinget, I. Kymissis, D. Rubenstein, X. Wang, and G. Zussman, "Challenge: ultra-low-power energy-harvesting active networked tags (EnHANTs)," in *Proceedings of the 15th annual international conference on Mobile computing and networking*. ACM, 2009, pp. 253–260.

[23] A. J. Goldsmith and S.-G. Chua, "Adaptive coded modulation for fading channels," *IEEE Transactions on Communications*, vol. 46, no. 5, pp. 595–602, 1998.

[24] L. Wan, H. Zhou, X. Xu, Y. Huang, S. Zhou, Z. Shi, and J.-H. Cui, "Adaptive modulation and coding for underwater acoustic OFDM," *IEEE Journal of Oceanic Engineering*, vol. 40, no. 2, pp. 327–336, Apr. 2015.

[25] ——, "Field tests of adaptive modulation and coding for underwater acoustic OFDM," in *Proceedings of the 8th ACM International Workshop on Underwater Networks and Systems*, Nov. 11-13, 2013.

[26] D. Banerjee, S. Sen, A. Banerjee, and A. Chatterjee, "Low-power adaptive RF system design using real-time fuzzy noise-distortion control," in *Proceedings of the 2012 ACM/IEEE international symposium on Low power electronics and design*. ACM, 2012, pp. 249–254.

[27] D. Banerjee, S. Devarakond, S. Sen, and A. Chatterjee, "Real-time use-aware adaptive MIMO RF receiver systems for energy efficiency under BER constraints," in *Proceedings of the 50th Annual Design Automation Conference*. ACM, 2013, p. 56.

[28] T. H. Lee, *The design of CMOS radio-frequency integrated circuits*. Cambridge university press, 2004.

[29] Y. Li, B. Bakkaloglu, and C. Chakrabarti, "A system level energy model and energy-quality evaluation for integrated transceiver front-ends," *IEEE Transactions on Very Large Scale Integration (VLSI) Systems*, vol. 15, no. 1, pp. 90–103, 2007.

[30] S. Cui, A. J. Goldsmith, and A. Bahai, "Energy-constrained modulation optimization," *IEEE Transactions on Wireless Communications*, vol. 4, no. 5, pp. 2349–2360, 2005.

[31] Y. Ding and R. Harjani, "A high-efficiency CMOS+ 22-dbm linear power amplifier," *IEEE Journal of Solid-State Circuits*, vol. 40, no. 9, pp. 1895–1900, 2005.

[32] B. Imran and J. Varun, "PAPR Analysis of DHT-Precoded OFDM System for M-QAM," in *Int. Conf. Intell. Adv. Syst., Kuala Lumpur, Malaysia*, 2010, pp. 1–4.

[33] J. G. Proakis, *Digital Communication*. McGraw-Hill, 2000.

[34] S. Cui, A. J. Goldsmith, and A. Bahai, "Modulation optimization under energy constraints," in *IEEE International Conference on Communications (ICC)*, vol. 4. IEEE, 2003, pp. 2805–2811.

[35] W. Tang and L. Wang, "Data rate maximization by adaptive thresholding RF power management under renewable energy," in *2010 IEEE International Conference on Computer Design (ICCD)*. IEEE, 2010, pp. 145–150.

[36] H. Meyr, M. Moeneclaey, and S. Fechtel, *Digital Communication Receivers: Synchronization, Channel Estimation, and Signal Processing*. John Wiley & Sons, Inc., 1997.

[37] Y. Huang, L. Wan, S. Zhou, Z. Wang, and J. Huang, "Comparison of sparse recovery algorithms for channel estimation in underwater acoustic OFDM with data-driven sparsity learning," *Elsevier Journal on Physical Communication*, vol. 13, pp. 156–167, Dec. 2014.

[38] Q. Lu, Y. Huang, Z. Wang, and S. Zhou, "Characterization and receiver design for underwater acoustic channels with large Doppler spread," in *OCEANS'15 MTS/IEEE Washington*. IEEE, 2015, pp. 1–6.

[39] K. Kadirvel, Y. Ramadass, U. Lyles, J. Carpenter, V. Ivanov, V. McNeil, A. Chandrakasan, and B. Lum-Shue-Chan, "A 330na energy-harvesting charger with battery management for solar and thermoelectric energy harvesting," in *2012 IEEE International Solid-State Circuits Conference Digest of Technical Papers (ISSCC)*. IEEE, 2012, pp. 106–108.

[40] J. Lu, S. Liu, Q. Wu, and Q. Qiu, "Accurate modeling and prediction of energy availability in energy harvesting real-time embedded systems," in *2010 International Green Computing Conference*. IEEE, 2010, pp. 469–476.

[41] S. Lin and D. Costello, *Error control coding*. Prentice-Hall, 2004.

[42] T. Granlund and P. L. Montgomery, "Division by invariant integers using multiplication," in *Proceedings of the SIGPLAN '94 Conference on Programming Language Design and Implementation*. ACM, 1994, pp. 61–72.

[43] P. Gigliotti. Serial-to-parallel converter. [Online]. Available: www.xilinx.com

[44] M.-S. Alouini and A. J. Goldsmith, "Adaptive modulation over nakagami fading channels," *Wireless Personal Communications*, vol. 13, no. 1-2, pp. 119–143, 2000.

[45] C. Moser, D. Brunelli, L. Thiele, and L. Benini, "Real-time scheduling for energy harvesting sensor nodes," *Real-Time Systems*, vol. 37, no. 3, pp. 233–260, 2007.

[46] S. Liu, Q. Wu, and Q. Qiu, "An adaptive scheduling and voltage/frequency selection algorithm for real-time energy harvesting systems," in *46th ACM/IEEE Design Automation Conference (DAC)*. IEEE, 2009, pp. 782–787.

[47] National centers for environmental information. [Online]. Available: http://www.ncdc.noaa.gov/cdo-web/datasets

[48] D. Zhao, J. Chen, and L. Wang, "Energy-adaptive pulse amplitude modulation for IR-UWB communications under renewable energy," *Journal of Signal Processing Systems*, vol. 76, no. 2, pp. 121–132, 2014.

[49] W. Huang and L. Wang, "Adaptive tracking channel control for gnss receivers under renewable energy," in *2015 16th International Symposium on Quality Electronic Design (ISQED)*. IEEE, 2015, pp. 212–216.

[50] U. Karra, G. Huang, R. Umaz, C. Tenaglier, L. Wang, and B. Li, "Stability characterization and modeling of robust distributed benthic microbial fuel cell (DBMFC) system," *Bioresource technology*, vol. 144, pp. 477–484, 2013.

[51] G. Huang, R. Umaz, U. Karra, B. Li, and L. Wang, "A biomass-based marine sediment energy harvesting system," in *2013 IEEE International Symposium on Low Power Electronics and Design (ISLPED)*. IEEE, 2013, pp. 359–364.

[52] ——, "A power management integrated system for biomass-based marine sediment energy harvesting," *International Journal of High Speed Electronics and Systems*, vol. 23, no. 01n02, p. 1450012, 2014.

[53] L. Wang and N. R. Shanbhag, "Low-power MIMO signal processing," *IEEE Transactions on Very Large Scale Integration (VLSI) Systems*, vol. 11, no. 3, pp. 434–445, 2003.

[54] W. Tang and L. Wang, "Cooperative OFDM for energy-efficient wireless sensor networks," in *IEEE Workshop on Signal Processing Systems (SiPS)*. IEEE, 2008, pp. 77–82.

[55] G. Huang and L. Wang, "High-speed signal reconstruction with orthogonal matching pursuit via matrix inversion bypass," in *2012 IEEE Workshop on Signal Processing Systems (SiPS)*. IEEE, 2012, pp. 191–196.

[56] ——, "High-speed signal reconstruction for compressive sensing applications," *Journal of Signal Processing Systems*, vol. 81, no. 3, pp. 333–344, 2015.

[57] J. Hsu, S. Zahedi, A. Kansal, M. Srivastava, and V. Raghunathan, "Adaptive duty cycling for energy harvesting systems," in *Proceedings of the 2006 international symposium on Low power electronics and design*. ACM, 2006, pp. 180–185.

[58] S. Liu, Q. Qiu, and Q. Wu, "Energy aware dynamic voltage and frequency selection for real-time systems with energy harvesting," in *Design, Automation and Test in Europe, 2008. DATE'08*. IEEE, 2008, pp. 236–241.

[59] J. Yi, F. Su, Y.-H. Lam, W.-H. Ki, and C.-Y. Tsui, "An energy-adaptive MPPT power management unit for micro-power vibration energy harvesting," in *2008 IEEE International Symposium on Circuits and Systems (ISCAS)*. IEEE, 2008, pp. 2570–2573.

[60] A. Mirhoseini, E. M. Songhori, and F. Koushanfar, "Automated checkpointing for enabling intensive applications on energy harvesting devices," in *Proceedings of the International Symposium on Low Power Electronics and Design*. IEEE Press, 2013, pp. 27–32.

[61] S.-J. Lee, J.-W. Choi, S. W. Kim, and J. Park, "A reconfigurable FIR filter architecture to trade off filter performance for dynamic power consumption," *IEEE Transactions on Very Large Scale Integration (VLSI) Systems*, vol. 19, no. 12, pp. 2221–2228, 2011.

[62] S. Venkataramani, A. Ranjan, K. Roy, and A. Raghunathan, "AxNN: energy-efficient neuromorphic systems using approximate computing," in *Proceedings of the 2014 international symposium on Low power electronics and design*. ACM, 2014, pp. 27–32.

[63] H. Ghasemzadeh, N. Amini, R. Saeedi, and M. Sarrafzadeh, "Power-aware computing in wearable sensor networks: An optimal feature selection," *IEEE Transactions on Mobile Computing*, vol. 14, no. 4, pp. 800–812, 2015.

[64] A. Sinha, A. Wang, and A. Chandrakasan, "Energy scalable system design," *IEEE Transactions on Very Large Scale Integration (VLSI) Systems*, vol. 10, no. 2, pp. 135–145, 2002.

[65] S. Chen, J. Chen, D. Forte, J. Di, M. Tehranipoor, and L. Wang, "Chip-level anti-reverse engineering using transformable interconnects," in *IEEE International Symposium on Defect and Fault Tolerance in VLSI and Nanotechnology Systems (DFTS)*, 2015, pp. 109–114.

[66] S. E. Quadir, J. Chen, D. Forte, N. Asadizanjani, S. Shahbazmohamadi, L. Wang, J. Chandy, and M. Tehranipoor, "A survey on chip to system reverse engineering," *ACM Journal on Emerging Technologies in Computing Systems (JETC)*, vol. 13, no. 1, pp. 1–34, 2016.

[67] Y. Zhang, Y. Huang, L. Wan, H. Zhou, S. Zhou, X. Shen, and H. Wang, "Adaptive OFDMA for downlink underwater acoustic communications," in *Oceans-St. John's, 2014*. IEEE, 2014, pp. 1–5.

[68] Y. Zhang, Y. Huang, L. Wan, S. Zhou, X. Shen, and H. Wang, "Adaptive OFDMA with partial CSI feedback for underwater acoustic communications," *Journal of Communications and Networks*, Aug. 2015, (accepted).

[69] J. R. Piorno, C. Bergonzini, D. Atienza, and T. S. Rosing, "Prediction and management in energy harvested wireless sensor nodes," in *Wireless Communication, Vehicular Technology, Information Theory and Aerospace & Electronic Systems Technology, 2009. Wireless VITAE 2009. 1st International Conference on*. IEEE, 2009, pp. 6–10.

[70] M. Pedram and Q. Wu, "Design considerations for battery-powered electronics," in *Proceedings of the 36th annual ACM/IEEE Design Automation Conference*. ACM, 1999, pp. 861–866.

[71] T. Darwish and M. Bayoumi, "Energy aware distributed arithmetic DCT architectures," in *IEEE Workshop on Signal Processing Systems (SIPS)*. IEEE, 2003, pp. 351–356.

[72] G. Huang and L. Wang, "Soft-thresholding orthogonal matching pursuit for efficient signal reconstruction," in *2013 IEEE International Conference on Acoustics, Speech and Signal Processing (ICASSP)*. IEEE, 2013, pp. 2543–2547.

[73] C. Bergonzini, D. Brunelli, and L. Benini, "Algorithms for harvested energy prediction in batteryless wireless sensor networks," in *2009. 3rd International Workshop on Advances in sensors and Interfaces (IWASI)*. IEEE, 2009, pp. 144–149.

[74] D. J. C. MacKay. (2014) Nrel: Measurement and instrumentation data center. [Online]. Available: http://www.nrel.gov/midc/

[75] D. R. Cox, "Prediction by exponentially weighted moving averages and related methods," *Journal of the Royal Statistical Society. Series B (Methodological)*, pp. 414–422, 1961.

[76] R. Zetik, J. Sachs, and R. S. Thomä, "UWB short-range radar sensing-the architecture of a baseband, pseudo-noise UWB radar sensor," *IEEE Instrumentation & Measurement Magazine*, vol. 10, no. 2, pp. 39–45, 2007.

[77] S. Chang, T.-S. Chu, J. Roderick, C. Du, T. Mercer, J. W. Burdick, and H. Hashemi, "UWB human detection radar system: A RF CMOS chip and algorithm integrated sensor," in *2011 IEEE International Conference on Ultra-Wideband (ICUWB)*. IEEE, 2011, pp. 355–359.

[78] L. Yang and G. B. Giannakis, "Ultra-wideband communications: an idea whose time has come," *IEEE Signal Processing Magazine*, vol. 21, no. 6, pp. 26–54, 2004.

[79] J. R. Fernandes and D. Wentzloff, "Recent advances in IR-UWB transceivers: An overview," in *Proceedings of 2010 IEEE International Symposium on Circuits and Systems (ISCAS)*. IEEE, 2010, pp. 3284–3287.

[80] M. R. Mahfouz, A. E. Fathy, M. J. Kuhn, and Y. Wang, "Recent trends and advances in UWB positioning," in *Wireless Sensing, Local Positioning, and RFID, 2009. IMWS 2009. IEEE MTT-S International Microwave Workshop on*. IEEE, 2009, pp. 1–4.

[81] R. Salman, T. Schultze, and I. Willms, "UWB material characterisation and object recognition with applications in fire and security," in *2008. IEEE International Conference on Ultra-Wideband (ICUWB)*, vol. 2. IEEE, 2008, pp. 203–206.

[82] E. C. Kim, S. Park, J. S. Cha, and J. Y. Kim, "Improved performance of UWB system for wireless body area networks," *IEEE Transactions on Consumer Electronics*, vol. 56, no. 3, pp. 1373–1379, 2010.

[83] D. Simic, A. Jordan, R. Tao, N. Gungl, J. Simic, M. Lang, L. Van Ngo, and V. Brankovic, "Impulse UWB radio system architecture for body area networks," in *2007 16th IST Mobile and Wireless Communications Summit*, 2007.

[84] D. Zito, D. Pepe, M. Mincica, F. Zito, A. Tognetti, A. Lanata, and D. De Rossi, "SoC CMOS UWB pulse radar sensor for contactless respiratory rate monitoring," *IEEE Transactions on Biomedical Circuits and Systems*, vol. 5, no. 6, pp. 503–510, 2011.

[85] D. Wu, R. Li, R. Li, H. Liang, and J. Luo, "Localization in UWB sensor networks for agriculture environment," in *4th International Conference on Wireless Communications, Networking and Mobile Computing (WiCOM)*. IEEE, 2008, pp. 1–4.

[86] I. Gresham, A. Jenkins, R. Egri, C. Eswarappa, N. Kinayman, N. Jain, R. Anderson, F. Kolak, R. Wohlert, S. P. Bawell *et al.*, "Ultra-wideband radar sensors for short-range vehicular applications," *IEEE Transactions on Microwave Theory and Techniques*, vol. 52, no. 9, pp. 2105–2122, 2004.

[87] K. K. Win, X. Wu, S. Dasgupta, W. J. Wen, R. Kumar, and S. Panda, "Efficient solar energy harvester for wireless sensor nodes," in *2010 IEEE International Conference on Communication Systems (ICCS)*. IEEE, 2010, pp. 289–294.

[88] L. Wang and N. R. Shanbhag, "Low-power filtering via adaptive error-cancellation," *IEEE Transactions on Signal Processing*, vol. 51, no. 2, pp. 575–583, 2003.

[89] L. Wang and N. Shanbhag, "Low-power AEC-based MIMO signal processing for gigabit ethernet 1000Base-T transceivers," in *Proceedings of the 2001 international symposium on Low power electronics and design*. ACM, 2001, pp. 334–339.

[90] W. Huang and L. Wang, "A channel-adaptive nonbinary LDPC decoder," in *Signal Processing Systems (SiPS), 2015 IEEE Workshop on*. IEEE, 2015, pp. 1–6.

[91] Y. Huang, P. Xiao, S. Zhou, and Z. Shi, "A half-duplex self-protection jamming approach for improving secrecy of block transmissions in underwater acoustic channels," *IEEE Sensors Journal*, vol. 16, no. 11, pp. 4100–4109, Jun. 2016.

[92] Y. Huang, S. Zhou, Z. Shi, and L. Lai, "Channel frequency response based secret key generation in underwater acoustic systems," *IEEE Transactions on Wireless Communications*, May 2016 (Accepted).

[93] A. Gerosa, S. Soldà, A. Bevilacqua, D. Vogrig, and A. Neviani, "An energy-detector for noncoherent impulse-radio UWB receivers," *IEEE Transactions on Circuits and Systems I: Regular Papers*, vol. 56, no. 5, pp. 1030–1040, 2009.

[94] A. F. Molisch, "Ultra-wide-band propagation channels," *Proceedings of the IEEE*, vol. 97, no. 2, pp. 353–371, 2009.

[95] M. Verhelst and W. Dehaene, "System design of an ultra-low power, low data rate, pulsed UWB receiver in the 0-960 MHz band," in *2005 IEEE International Conference on Communications (ICC)*, vol. 4. IEEE, 2005, pp. 2812–2817.

[96] P. Nain, D. Towsley, B. Liu, and Z. Liu, "Properties of random direction models," in *24th Annual Joint Conference of the IEEE Computer and Communications Societies. INFOCOM 2005.*, vol. 3. IEEE, 2005, pp. 1897–1907.

[97] S. Bandyopadhyay, E. J. Coyle, and T. Falck, "Stochastic properties of mobility models in mobile ad hoc networks," *IEEE Transactions on Mobile Computing*, vol. 6, no. 11, pp. 1218–1229, 2007.

[98] A. F. Molisch, D. Cassioli, C.-C. Chong, S. Emami, A. Fort, B. Kannan, J. Karedal, J. Kunisch, H. G. Schantz, K. Siwiak *et al.*, "A comprehensive standardized model for ultrawideband propagation channels," *IEEE Transactions on Antennas and Propagation*, vol. 54, no. 11, pp. 3151–3166, 2006.

[99] G. R. Aiello and G. D. Rogerson, "Ultra-wideband wireless systems," *IEEE Microwave Magazine*, vol. 4, no. 2, pp. 36–47, 2003.

[100] A. Darabiha, A. C. Carusone, and F. R. Kschischang, "Power reduction techniques for LDPC decoders," *IEEE Journal of Solid-State Circuits*, vol. 43, no. 8, pp. 1835–1845, 2008.

[101] J. Jin and C.-Y. Tsui, "An energy efficient layered decoding architecture for LDPC decoder," *IEEE Transactions on Very Large Scale Integration (VLSI) Systems*, vol. 18, no. 8, pp. 1185–1195, 2010.

[102] E. Sharon, S. Litsyn, and J. Goldberger, "An efficient message-passing schedule for LDPC decoding," in *IEEE Convention of Electrical and Electronics Engineers in Israel*. IEEE, 2004, pp. 223–226.

[103] C. Condo, G. Masera, and P. Montuschi, "Unequal error protection of memories in ldpc decoders," *IEEE Transactions on Computers*, vol. PP, no. 99, 2014.

[104] C. Roth, P. Meinerzhagen, C. Studer, and A. Burg, "A 15.8 pJ/bit/iter quasi-cyclic LDPC decoder for IEEE 802.11 n in 90 nm CMOS," in *2010 IEEE A-SSCC*. IEEE, 2010, pp. 1–4.

[105] J. Jin and C.-Y. Tsui, "A low power layered decoding architecture for LDPC decoder implementation for IEEE 802.11 n LDPC codes," in *ISLPED*. IEEE, 2008, pp. 253–258.

[106] M. Cho, J. Schlessman, W. Wolf, and S. Mukhopadhyay, "Reconfigurable sram architecture with spatial voltage scaling for low power mobile multimedia applications," *IEEE Transactions on Very Large Scale Integration (VLSI) Systems*, vol. 19, no. 1, pp. 161–165, 2011.

[107] M. S. Khairy, A. Khajeh, A. M. Eltawil, and F. J. Kurdahi, "Joint power management and adaptive modulation and coding for wireless communications systems with unreliable buffering memories," *IEEE Transactions on Circuits and Systems I: Regular Papers*, vol. 61, no. 8, pp. 2456–2465, 2014.

[108] N. Wiberg, *Codes and decoding on general graphs*. Citeseer, 1996.

[109] S. Borkar, T. Karnik, S. Narendra, J. Tschanz, A. Keshavarzi, and V. De, "Parameter variations and impact on circuits and microarchitecture," in *Proceedings of the 40th annual Design Automation Conference*. ACM, 2003, pp. 338–342.

[110] M. Cho, J. Schlessman, W. Wolf, and S. Mukhopadhyay, "Accuracy-aware SRAM: a reconfigurable low power SRAM architecture for mobile multimedia applications," in *Proceedings of the 2009 ASP-DAC*. IEEE, 2009, pp. 823–828.

[111] S. Mukhopadhyay, H. Mahmoodi, and K. Roy, "Modeling of failure probability and statistical design of SRAM array for yield enhancement in nanoscaled CMOS," *IEEE Transactions on Computer-Aided Design of Integrated Circuits and Systems*, vol. 24, no. 12, pp. 1859–1880, 2005.

[112] V. C. Gaudet, "Low-power LDPC decoding by exploiting the fault-tolerance of the sum-product algorithm," *Contemporary Mathematics*, vol. 523, pp. 165–172, 2010.

[113] D. J. C. MacKay. Encyclopedia of sparse graph codes. [Online]. Available: http://www.inference.phy.cam.ac.uk/mackay/codes/data.html